NOVEL METHODS OF THERMALLY MEDIATED SELECTIVE NEURAL INHIBITION

by

JUNQI ZHUO

Submitted in partial fulfillment of the requirements for the degree of Doctor of Philosophy

Department of Biomedical Engineering

CASE WESTERN RESERVE UNIVERSITY

May. 2023

CASE WESTERN RESERVE UNIVERSITY

SCHOOL OF GRADUATE STUDIES

We hereby approve the thesis/dissertation of

Junqi Zhuo

candidate for the degree of **Doctor of Philosophy***.

Committee Chair

Andrew M. Rollins

Committee Member

Michael W. Jenkins

Committee Member

Hillel J. Chiel

Committee Member

Dustin J. Tyler

Committee Member

Kenneth R. Laurita

Date of Defense

January. 12, 2023

*We also certify that written approval has been obtained for any proprietary material contained therein.

Table of Contents

List of Tables

List of Figures

Acknowledgments

Completing this dissertation has allowed me to reflect on my Ph.D. journey and express my heartfelt gratitude to all my advisors, friends, and family members who supported me along the way.

I would like to thank my PI, Dr. Michael Jenkins, who guided me through the whole process and supported me with great trust, patience, and wisdom. I would also like to thank Dr. Andrew Rollins, Dr. Hillel Chiel, Dr. E. Duco Jansen, Dr. Michael Moffitt and Dr. Charles Horn. It is my honor to learn from all of you how to work professionally, cooperate closely, and live positively. All of those intense discussions and insightful humor will become unforgettable memories for me. I would like to thank Dr. Dustin Tyler and Dr. Kenneth Laurita for serving on my committee and guiding me to the finish line.

I would also like to acknowledge the contribution to this work of my colleagues, collaborators, and friends whom I have met along the journey. Due to the limited space here, I can only name a few: Shi Gu, Emilie Lothet, Yehe Liu, Matthew McPheeters, Brecken Blackburn, Maryse Lapierre-Landry, Jeremy Ford, Jeffrey Gill, Mohit Ganguly, Yu Huan, Catherine Kehl, Andrew Buzza, Aaron Skubal, Aaron Anqi Ren, and Yi Zhong. It has been a pleasure not only to collaborate with you but also to know you as a friend and share some precious memories.

Also, I would like to thank the undergraduates that helped me conduct my research projects: Sachin Shankar, Elizabeth Jackson, Zihui Ou, Yuhan Zhang, Chloe Weidrick, and Marcelo Beramendi Caballero. Your participation not only accelerated the research but also provided a chance for me to learn how to communicate and lead a team.

Last but now least, I would like to thank my family members for their understanding and support. I would like to thank my parents for understanding and supporting all my decisions, including studying abroad and not being able to visit them for years. I would like to thank my mom and dad for taking care of themselves and fighting cancer fearlessly. I would like to thank my other family members for taking care of my dad during his surgery. I would like to thank my mother-in-law for the courage to travel across continents alone to visit and support me and my wife. My dear wife, Xiaowei, your presence in my life has been the greatest blessing. Together we have grown, learned, and experienced so much. Your motivation and love have pushed me to be the best version of myself. Having you and our daughter in my life has given everything a new level of meaning.

List of Abbreviations

Abbreviations	Definition
AP	Action Potential
CAP	Compound action potential
CW	Continuous wave
DC	Direct current
FUS	Focused ultrasound
GDP	Gross domestic product
HFAC	High-frequency alternating current
IACUC	Institutional animal care and use committee
INI	Infrared neural inhibition
INS	Infrared neural stimulation
IR	Infrared
NIS	Normalized inhibition strength
OTC	Over the counter
PBM	Photobiomodulation
RAUC	Rectified area under the curve
SM	Single Mode
RH	Resistive heating
TEA	Tetraethylammonium
TTX	Tetrodotoxin

Novel Methods of Thermally Mediated Selective Neural Inhibition

Abstract

by

JUNQI ZHUO

Small-diameter axons (e.g., unmyelinated C fibers) are commonly afferent axons that carry critical sensory signals. Selective inhibition of dysfunctional small-diameter axons can be useful for basic neuroscience research and lead to treatments for neurological diseases (e.g., neuropathic pain and persistent hypertension), but remains an unmet need. Conventional pharmaceutical targets are distributed throughout the body, which causes systematic side effects. Electrode-based neuromodulation modalities tend to block large-diameter axons first. Other efforts, such as multi-electrode designs, have achieved spatial selectivity, which is challenged by the degradation of electrode performance due to immune responses. There is a need for a modality that can intrinsically and reliably induce size-selective inhibition of small-diameter axons.

Our lab and collaborators have demonstrated in previous studies that infrared (IR) neural inhibition (INI) can selectively inhibit small-diameter axons via the heat induced by the absorption of IR light (e.g., 1470 nm, 1860 nm) which thermally accelerates ion-

channel dynamics. In this work, we first explored the possibility of lowering the IR power threshold for INI with isotonic ion replacement using glucose and/or choline in the extracellular fluid. We applied IR and isotonic ion replacement simultaneously to the same nerve segment, both at a sub-threshold level, and the results confirmed that the IR power threshold of size-selective INI can be lowered by isotonic ion replacement. Second, we tested the hypothesis that resistive heating can reproduce the size selectivity of INI. We fabricated a customized resistive heating cuff and tested localized heat application via both resistive heating and INI on the same nerve. The experimental results confirmed that resistive heating can reproduce the size-selective inhibition on small-diameter axons with higher overall energy efficiency. Further numerical simulation showed that INI and resistive heating required similar temperature elevations on the axons for the same inhibitory effect. In addition to the two projects, related preliminary methods and test results are included in the appendix.

Here, we present efforts to provide modalities for size-selective inhibition on small-diameter axons. Further studies in this direction can help researchers and physicians explore the functionalities of small-diameter axons and develop future therapeutic options.

Chapter 1. Introduction

1.1 Motivation

There is an unmet need to block the signaling of small-diameter afferent axons. Small-diameter axons are commonly afferent axons (e.g., unmyelinated C fibers) that carry various sensory signals that are critical for vital physiological conditions [1]. Selective inhibition of dysfunctional small-diameter axons can help treat diseases. For example, it will be valuable to selectively block aberrant, persistent nociceptive pain signals while avoiding disruption to motor functions and other systematic side effects[2,3]. This can be hard to achieve with conventional pharmaceuticals. Another example is persistent hypertension caused by hyperactive sensory feedback signals, which may be blocked by selective inhibition of the small-diameter axons [4]. In addition, selective inhibition of small-diameter afferent fibers can help researchers explore the functionality of neural circuits by manipulating the inputs.

Currently, all standard pathways to block small-diameter fibers have their limitations, despite the many potential applications [1,5]. Conventional pharmaceuticals are limited in their selectivity as the agents usually diffuse throughout the whole body and also affect off-targets that lead to side effects [6,7]. Electrode-based neuromodulation modalities tend to block large-diameter axons as the transmembrane potential evoked by the extracellular electrodes is proportional to the axon diameter. Additional efforts on the electrode configuration and stimulation waveform have to be made to achieve limited success in selective neural inhibition of the small-diameter axons [2]. And the selectivity can be further degraded as the electrode properties change and anatomy structure varies during chronic

implantation. There is a need to develop a neuromodulation modality that can reliably induce selective inhibition of small-diameter axons [1,5].

Infrared (IR) neural inhibition (INI) has been demonstrated in previous studies to selectively inhibit small-diameter axons via the heat induced by the absorption of IR light (e.g., 1470 nm, 1860 nm) [8]. The wavelengths used in INI have a strong water absorption coefficient and can induce heat directly inside the nerve. It has been modeled and experimentally verified that heating during INI caused the acceleration of voltage-gated potassium ion channels which lead to the inhibitory effect [9,10]. The IR application protocol for selective inhibition of small-diameter axons has been explored in invertebrates (*Aplysia*) and successfully transferred to vertebrates (musk shrew) [8], which holds potential for future translation applications. Despite the potential for translational application of INI, there are currently limitations in our understanding of the effects of the thermal loads applied to neural tissue during the procedure. Additionally, the feasibility of using INI *in vivo* with an implantable design has been questioned due to the mechanical stiffness of optical fibers and the relatively low power efficiency of infrared light sources.

1.2 Dissertation outline

In this work, we first explored the possibility of lowering the IR power threshold for INI with isotonic ion replacement in the extracellular fluid. It has been shown that neural conduction can be blocked with isotonic ion replacement alone (i.e., with high glucose saline, high choline saline, or high glucose/high choline saline). We identified the concentration threshold for the ion-replacement agents (i.e., glucose and/or choline) mixed in regular saline for inducing neural inhibition. We applied IR and isotonic ion replacement simultaneously to the same segment of the nerve, both at a sub-threshold level, and achieved selective neural inhibition. The results confirmed that the IR power threshold for

INI can be lowered by isotonic ion replacement, which can help lower the thermal load on neural tissue during INI

Second, we identified that the low conversion efficiency from electricity to IR light at the laser diode was a major limitation for implementing INI with an implantable design. To bypass this limitation, we tested the hypothesis that other heating modalities such as resistive heating (RH), when applied in a similar manner, can induce selective inhibition on the small-diameter axons. To conduct the test, we fabricated a customized resistive heating cuff with a thermal sensor to apply localized heat on the nerve and monitor the induced temperature elevation (ΔT). We tested the heating cuff in comparison with the INI in terms of the ΔT threshold of selective inhibition, the size selectivity across different nerves, and the efficiency of converting electricity to heat. A numerical simulation of the heating process during INI and resistive heating was conducted to explore the uniformity of the induced heat distribution inside the nerve. The simulation suggested that the ΔT thresholds for inducing selective inhibition at the central region where the axons are located were similar between the two modalities. This study proposes a resistive-heating-based neural interface that can be fabricated using flexible materials and has a high energy conversion efficiency, which could significantly increase its feasibility as an implantable solution. Furthermore, this work also suggested that selective inhibition on the small-diameter axons can be an inherent property of heat-based neural inhibition modalities.

In addition, Appendix A included the preliminary test results of the parameter spaces of infrared neural inhibition are included. Appendix B included the protocols for fabricating spiral resistive heating nerve cuffs. Appendix C included the considerations for conducting *ex vivo* electrophysiological tests with *Aplysia* nerve. Appendix D included the

experimental protocols for conducting nerve dissection and *ex vivo* electrophysiological tests for photobiomodulation (PBM) with rat sciatic nerve.

1.3 Summary

The present research summarizes our efforts to provide modalities for size-selective inhibition on small-diameter axons. The isotonic ion replacement method can help lower the thermal dose applied to neural tissues during INI. The resistive heating neural interface showed that thermally-mediated neural inhibition is selective for small-diameter axons. The resistive heating-based neural interface also significantly increased the feasibility of applying thermally-mediated size-selective inhibition with implantable designs. Further studies in this direction can help researchers and physicians explore the functionalities of small-diameter axons and develop future therapeutic options.

Chapter 2. Background

2.1 Neurophysiology

2.1.1 Neurons and action potentials

It is necessary to understand neuroanatomy and how neurons function for developing/optimizing neuromodulation technologies. Neurons are highly specialized cells that can transfer information (i.e., neural activity) via electrochemical signals between neurons and other effector organs (e.g., muscles). Dendrites and axons are the unique cellular structures of a neuron. Dendrites are branched extensions of the neuron's cellular structure, which can receive electrochemical signals from other neurons and send them to the somata for integration. Axons are the major extension of the neuron structure that can connect to other neurons or organs and transfer information over a long distance (up to ~ 1m). A bundle of axons (also called nerve fibers) that travel together is called a nerve.

Within the cell membrane of a neuron, different types of ion channels are expressed to permit the movement of electrically charged ions across the cellular membrane. The ion channels cause the cellular membrane to have selective permeability for each ion species. Types of ion channels can be defined based on the mechanism of gating: voltage-gated ion channels, ligand-gated ion channels, mechanical-gated ion channels, temperature-gated ion channels, light-gated ion channels, and other gating mechanisms [11,12]. There are also ion channels that are not gated and remain open all the time (i.e., "leak channels") [13–15]. The opening of ion channels increases the membrane permeability to specific ion species. The flow direction and flux of ions through ion channels depend on the ion concentration gradient and electrical potential gradient across the membrane. In addition to ion channels, there are ion pump proteins within the neuron

membrane that actively transfer ions across the membrane, using the energy of ATP hydrolysis [16–18]. One example is the Na^+-K^+ pump, which can transfer three Na^+ ions outwards and two K^+ ions inwards at a time, and is important for the maintenance of the ion concentration gradient; it also contributes partially to the resting membrane potential across the membrane [19].

As a result of all the ion movement, the ion concentration is different across the membrane, but on both sides of the membrane, ion concentrations are constrained by the need to maintain bulk electroneutrality and osmotic balance. In the resting state, neurons have a high K^+ ion concentration and a low Na^+ ion concentration within the cytoplasm. The ion concentration gradient across the membrane (from the cytoplasm to the extracellular fluid surrounding the neuron) causes a resting membrane potential that is more negative on the inside of the membrane. Each species of ions contributes to the resting potential by its equilibrium potential according to the Nernst equation:

$$E_x = \frac{RT}{zF} \ln \frac{[ion]_{ouside}}{[ion]_{inside}}$$

where R is the ideal gas constant (8.314 J/mol/K), T is the temperature in degrees on the Kelvin scale, z is the valence (the electrical charge) of the ion, and F is Faraday's constant (F= 96,485 C/mol). When calculating the resting potential, usually only Na^+, K^+, and Cl^- ions are taken into consideration. But other ions, such as Ca^{2+} and Mg^{2+} can also play important roles in establishing membrane potentials. Based on the Nernst equation, a reversal potential can be calculated for each ion species. When the membrane potential is changed across the reversal potential, the ionic current reverses. At the reversal potential, there is no net ion current across the membrane. For most neurons, the reversal potential is about +60 mV for Na^+ ions, about -80 mV for K^+ ions, and about -60 mV for Cl^- ions. As the results of all the ionic current flow across the membrane, most neurons have

a resting membrane potential of about -70 mV. When the gated-ion channel of the specific type of ion is opened, the ion flow across the membrane will bring the membrane potential towards the equilibrium potential of that ion. In other words, the concentration gradient that is actively maintained by the ion pumps provides the driving force for the rapid membrane potential change during neural conduction, as will be described next.

When an electrical or certain chemical stimulus is applied to a neuron's membrane, the membrane potential can be changed. Depending on the intensity of the stimulus, either a graded potential or an action potential can be initiated. Due to the presence of voltage-gated sodium channel thresholds, the response to this change in membrane potential can be divided into graded potentials and action potentials. Local changes in membrane potential can further alter the membrane potential in nearby regions, which at a macroscopic level appears to be the conduction of neural signals.

A graded potential is initiated when the stimulus is not large enough to activate the voltage-gated Na^+ channels sufficiently to generate an action potential. Graded potentials can vary in amplitude and duration based on the stimulus parameters. A graded potential will gradually repolarize/hyperpolarize (depending on the initial stimulus) towards the resting potential by non-gated ion channels and subthreshold responses of voltage-gated channels. When a graded potential is initiated, it can alter the adjacent membrane's potential and induce the passive conduction of neural signals. However, passive conduction attenuates rapidly over distance as it does not induce a regenerative response. When stimuli are applied at short intervals, it is possible to have the summation of graded potentials on the same membrane region, because ion channels need time to change the membrane potential back to the resting potential. A summed graded potential can propagate further via passive conduction as it has a bigger initial amplitude and/or duration. This typically happens on the post-synaptic membrane of dendrites where the summation

of graded potentials changes the excitability of the specific region of the membrane. When the activity of one neuron regulates the excitability of other neuron(s), it is called neuromodulation. Similarly, if a neuron releases a chemical that alters the responsiveness of a neuron to other chemical signals, this is also called neuromodulation. This is the original and biological form of neuromodulation as opposed to the biomedical engineering form of neuromodulation where an external modality is applied to change a neuron's excitability or alter the neural conduction.

In contrast to graded potential and passive conduction, an action potential is initiated when the stimulus is strong enough to depolarize the membrane potential sufficiently that the inward current through the voltage-gates Na^+ ion channels is larger than the outward current through other channels, leading to an explosive regenerative positive feedback loop that rapidly opens many more Na^+ ion channels. There are four phases of an action potential: depolarization, repolarization, hyperpolarization, and recovery (to resting potential). First, the initial membrane depolarization beyond the threshold increases the likelihood of opening the voltage-gated Na^+ ion channels. As some of the voltage-gated Na^+ channels begin to open, Na^+ ions flow into the neuron rapidly and further depolarize the membrane potential. As a result of this positive feedback, more voltage-gated Na^+ ion channels will open and result in a rapid inflow of Na^+ ions. This rapidly depolarizes the membrane potential toward the equilibrium potential of Na^+. At about +30 mV, the voltage-gated K^+ channels begin to open due to the membrane depolarization, but at a rate slower than the voltage-gated Na^+ channels. As the potassium channels begin opening, the voltage-gated Na^+ channels will begin to close and reduce the inflow of Na^+ ions due to the inactivation process caused by sustained depolarization. The peak voltage reaches approximately +40 mV. The peak amplitude of action potentials remains constant for a given neuron membrane and does not depend on the intensity of

the initial stimulus. This is summarized as the "all or none" characteristic of an action potential, similar to a digital discrete signal. Since the peak amplitude does not depend on the initial stimulus, it cannot be used to convey information. Instead, the firing rate of action potentials is used to represent the strength of the neural signal. For example, a higher firing rate of a motor neuron can generate a stronger muscle force. A higher firing rate of a sensory neuron represents a stronger stimulus. It should be noted, however, that the peak of the action potential can vary due to the build-up of sodium inactivation, or to the activation of other slower ion conductances, so the simplification that an action potential is an “all-or-nothing” binary signal is not correct, and the differences in amplitude of the peak of the action potential can also contain information.

After reaching the peak, the repolarization phase of the action potential begins as the outflow of K^+ ions increases. When the membrane repolarizes and reaches the resting potential, the membrane potential will continue to hyperpolarize due to the time lag to close the voltage-gated K+ channels. Then the membrane potential gradually returns to the resting potential as the voltage-gated K+ channels close and potassium permeability returns to its resting state value. After that, the axon membrane is ready for the initiation of the next action potential. Because the action potential is essentially regenerated along the entire length of an axon, the action potentials can propagate rapidly over a long distance without attenuation. Due to the inactivation of the voltage-gated Na^+ channels, there is an absolute refractory period during which the membrane won’t be able to respond to a stimulus. This is followed by a relative refractory period, during which a stimulus stronger than usual will be required for the initiation of an action potential. The existence of refractory time ensures the directional propagation of action potentials and limits the maximum frequency of transmission.

2.1.2 Peripheral nerve structure

The nervous system can be divided into two main parts: the central nervous system (i.e., the brain and spinal cord), and the peripheral nervous system (i.e., the nerves that branch from the brain and spinal cord and innervate the whole body). The peripheral nerves are a collection of axons connecting and communicating with different regions in the body. The axons in the peripheral nerve can be categorized as afferent nerve fibers that relay sensory signals toward the spinal cord or brain or the efferent fibers that relay signals to peripheral organs to achieve an effect (e.g., activate a muscle).

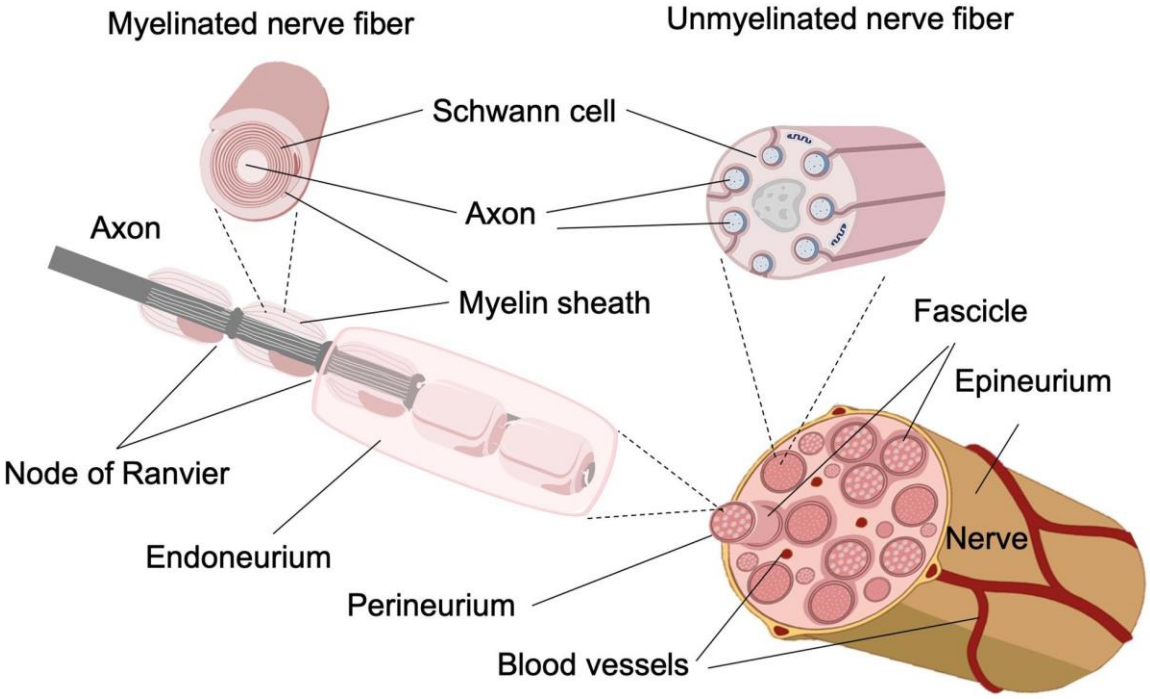

Figure 2.1. Schematic of the structure of a peripheral nerve.

The figure shows the structure of myelinated and unmyelinated axons. It also shows the different layers of connective tissues and other surrounding tissue. (Guedan-Duran et al., 2020. The original work is published with permission under a Creative Commons Attribution 4.0 International License. To view a copy of this license, visit http://creativecommons.org/licenses/by/4.0/).

Since axons project over long distances from the somata to reach their target organs, it is necessary to protect the fragile axons with glial cells. In the peripheral nervous

system, Schwann cells can make myelin to insulate axons and increase signal transduction. Axons with myelinated Schwann cells are called myelinated axons (see Figure 2.1). The myelin forms a laminated structure wrapping around the axon with a period of approximately 12 mm along the length of the axon. The exposed axonal regions between segments of myelin are the nodes of Ranvier. Schwann cells also support and provide nutrition for the unmyelinated axons, by wrapping around a bundle of 5 to 20 unmyelinated axons, which is called a Remak bundle (see Figure 2.1).

Based on the axon diameter and speed of neural conduction along the nerve (i.e., conduction velocity), nerve fibers (axons) can be categorized into A, B, and C fibers. A fibers can be further subdivided into Aα, Aβ, Aγ, and Aδ as the size decreases. A fibers include all the somatic efferent and afferent fibers. B fibers are the preganglionic fibers in the autonomic nervous system. C fibers include both somatic afferent fibers and the postganglionic fibers in the autonomic nervous system. Both A and B fibers are myelinated whereas C fibers are unmyelinated. Here is a summary of the properties of the nerve fiber groups:

Table 2.1. Classification of nerve fibers [20]

Fiber Type	Sub-type	Functions		Radius (μm)	Conductance Velocity (m/s)
A	α	Myelinated somatic afferent and efferent	Proprioception, somatomotor	12-20	70-120
	β		Touch, pressure	5-12	30-70
	γ		Motor for muscle spindles	3-6	15-30
	δ		Pain, cold, touch	2-5	12-30
B		Myelinated preganglionic autonomic		< 3	3-15
C	Dorsal horns	Unmyelinated somatic afferent	Pain, temperature, mechanoreception, reflex response	0.5-2	0.5-2

Fiber Type	Sub-type	Functions		Radius (μm)	Conductance Velocity (m/s)
	Sympathetic	Unmyelinated autonomic postganglionic	Pilomotor, sudomotor and vasomotor	0.7-2.3	0.7-2.3

Further, there are several general principles regarding axon diameter, myelination condition, conduction velocity, and function. First, myelinated axons are generally larger in diameter compared with unmyelinated axons because axons need to be larger than approximately 1 μm for myelination to commence [21]. Second, myelinated axons have a faster conduction velocity compared with unmyelinated axons because the myelination enabled the saltatory conduction between the nodes of Ranvier [22]. Third, under the same myelination condition, axons with a smaller diameter will have a slower conduction velocity. For unmyelinated axons, the conduction velocity is related to the axon diameter through the following approximation equation:

$$v \cong \frac{1}{8}\frac{1}{C_m}\sqrt{\frac{d}{R_m^* R_i}},$$

where C_m is the membrane capacitance per unit area, d is the axon diameter, R_m^* is the membrane resistance of a unit area, and R_i is the intracellular resistivity. Fourth, afferent fibers are mostly small-diameter axons. About 70% of all the noxious afferent fibers are C fibers [11].

In addition to the axons, the design of the neural interface needs to take into account the influence of the other structures that can help protect and provide nutrients to the axons to achieve normal neural conduction (see Figure 2.1). The epineurium is the outermost dense connective tissue that insulates the whole nerve. Within the nerve, the perineurium warps around fascicles, which are bundles of many axons. Within each

fascicle, the endoneurium forms an elongated supporting mesh structure that protects the axons and Schwann cells. Adipose tissue wraps around the epineurium and also around fascicles to provide support for the nerve to slide between muscles and bones [23]. Vasculature exists at all levels of the nerve branching from the arterioles at the epineurium to the capillaries at the endoneurium. The maintenance of normal intraneural blood flow is critical for the supply of oxygen and nutrition that axons need [24]. Intraneural blood is so important that a previous study demonstrated that applying pressures over 20 mmHg can block intraneural blood flow and cause adverse effects [25,26].

Overall, an understanding of the peripheral nervous system's structure, properties, and function can guide the design of new neuromodulation devices that are effective, reliable, and safe.

2.1.3 Dysfunction of small-diameter axons

Dysfunction of small-diameter axons, including the afferent sensory axons (Aδ and C fibers) and the autonomic fibers (B fibers), can severely impact the normal function of the peripheral nervous and autonomic nervous systems. In the peripheral nervous system, Aδ fibers transmit sensory information related to pain, temperature, and mechanical stimuli, while C fibers transmit pain and temperature sensations [27]. This sensory information is critical for both reflexive and voluntary movements. In the autonomic nervous system, the small-diameter axons innervate various organs and provide critical sensory information for the maintenance of homeostasis [28]. Various pathological processes can cause damage to small-diameter axons, including mechanical injury, and underlying medical conditions such as diabetes and autoimmune diseases. Consequently, dysfunction of small-diameter axons can further cause a range of syndromes/disorders, including but not limited to neuropathic pain, persistent hypertension, and heart failure [29,30].

As an example, neuropathic pain is a common issue associated with the dysfunction of small-diameter axons (Aδ and C fibers) [31]. After an injury or other pathological processes, the damaged small-diameter axons may become hyperactive or hypersensitive [32,33], primarily due to the upregulation of sodium-ion channel expression [34–36]. When the hypersensitive C fibers are repeatedly activated or spontaneously firing, dorsal horn neurons will exhibit a progressively increased response to repetitive C-fiber activation which is called the windup effect [37]. The windup effect can further cause central sensitization which means increased sensitivity to C-fiber activity [38]. Eventually, the overwhelming afferent signal will trigger hard-to-treat neuropathic pain [39,40]. The prevalence of neuropathic pain in the general population is about 7 – 10 % [41,42], which makes it a major public health issue [43]. While the symptoms can range from mild to incapacitating [44], the economic burden on the patients and society is universal [45,46]. Research data from the 2006 – 2008 National Health and Wellness Survey shows that 51.2% of neuropathic pain patients report their pain as severe with an annual direct cost of $12,856 [47]. According to a more recent estimation, neuropathic pain caused an $80 billion loss in total lost wages for patients and a related $216 billion loss in the gross domestic product (GDP) [48].

While pharmaceuticals are commonly used to treat disorders related to small-diameter axon dysfunction, the ability to selectively target small-diameter axons with drugs is limited. For example, for pain management, both over-the-counter (OTC) and prescription pain medications can provide a non-invasive intervention. However, these medications can cause systematic side effects as the active ingredients may diffuse throughout the body and bind to receptors in various organs. Therefore, side effects involving the unwanted inhibition of motor functions are common [6]. Pain medications also

often become ineffective after the establishment of drug resistance [49,50]. The local application of anesthetics that work on the axonal membrane, such as lidocaine, can selectively block small-diameter C fibers due to their unmyelinated nature [51–53]. However, this method can only provide temporary pain relief and is not effective in treating chronic pain. Opioid analgesics are used to manage pain that is resistant to other first-line pain medications[54]. However, their use has contributed to the opioid epidemic due to their strong potential for addiction and dose dependence [54–56]. When medication methods are exhausted for treating pain, denervation is often the last resort [57,58], which terminates neural conduction on all axons using tools such as radio-frequency ablation (RFA), and gamma-knife radiosurgery [59–63]. But the function loss of both large- and small-diameter axons can lead to unwanted side effects such as weakness of muscle [64,65]. As another example, renal denervation using (RFA) can be an effective treatment for patients with persistent hypertension caused by abnormal afferent input, who have not responded to pharmaceuticals. [4,66]. But the procedure ablates both afferent and efferent axons without selectivity. Therefore, the potential damage of efferent axons can cause a significant functional loss, which limits its translational application [60,67].

In short, dysfunction of small-diameter axons can lead to severe disorders due to their critical role in the normal functioning human body. Current treatments for small-diameter axon dysfunction, such as medications and denervation procedures, lack the selectivity on small-diameter axons and may have undesirable side effects. The development of modalities for selectively inhibiting small-diameter axons could help identify their roles in the neural circuits and develop new treatments that can effectively target these axons.

2.2 Light tissue interaction

When light is emitted toward a biological tissue, several interactions can happen, including reflection, refraction, scattering, and absorption. When a much higher photon density is applied, nonlinear effects can also happen (e.g., second-harmonic generation, two-photon absorption, and optical parametric oscillation). As infrared neuromodulation does not rely on those nonlinear effects, it will not be discussed here.

2.2.1 Reflection and refraction

When light hits the interface between the tissue's outer surface and the surrounding medium, reflection and refraction can happen. The angle of the incident light and the difference of refractive indexes between the two mediums determine the angle of reflected and refracted light based on the Fresnel equations and Snells law [68]. Further, reflection and refraction can happen wherever there is a refractive index mismatch in the light path. The refractive index, n, can be defined as the ratio between the speed of light in vacuum and the speed of light in a given medium.

2.2.2 Absorption

Electromagnetic absorption can manifest by electronic, vibrational, or rotational transitions. There are several possible outcomes of the excited molecule. For electronic transition, the excited electron can relax to the ground state by emitting another photon (fluorescence or phosphorescence). The absorption of a photon can also stimulate the molecule’s vibrational and rotational modes and manifest macroscopically as heating of the medium. For the wavelengths (1460 nm and 1860 nm) used in infrared neuromodulation, water in biological tissues is the major absorber as it has an absorption coefficient orders higher than other major components in the nerve [69]. For the wavelengths (650 nm, 808 nm, and 980 nm) used in photobiomodulation (PBM), the specific absorber of light is suggested to

be cytochrome C [70], although this is still under debate [71]. To estimate a tissue's light absorption properties, scientists have measured the light absorption spectrum of the common compositions of tissue, such as water melanin, and hemoglobin [72,73].

2.2.3 Scattering

Two types of scattering can happen in biological tissue: elastic and inelastic (e.g., Raman scattering) scattering. Both types of scattering involve the change of photon direction. Elastic scattering does not involve energy exchange between the photon and the scattering particle whereas inelastic scattering does. The probability of inelastic scattering is much lower than elastic scattering and will not be discussed in this thesis. For elastic scattering, the direction of a scattered photon depends on the light wavelength, λ, and the size of the scattering particle. When the scattering particle is much smaller than the wavelength of the incident light, Rayleigh scattering can be used to approximate scattering in the medium. Rayleigh scattering states that the amount of scattering is inversely proportional to the 4^{th} power of the wavelength. Mie theory is typically used for particles similar in size to the wavelength. The Mie solution solves light scattering from a spherical particle using the Maxwell equations. Unfortunately, solutions for other shaped particles are not available and approximations are needed. Geometrical scattering can be used for estimating scattering from particles much larger than the light wavelength.

2.2.4 Modeling of the light propagation in biological tissue

It is very valuable to understand how light is distributed in biological tissues during delivery, not just for optical neuromodulation but also for many other biomedical optical applications. The theoretical calculation of light distribution using Maxwell's equation is only possible for ideal sphere objects, which is not true for biological tissues. It is also impractical to know the exact composition and optical properties of the biological tissue. Taking one step

back, biological tissues can be simplified as the composition of several types of typical tissues for the purpose of light distribution modeling. The level of detail depends on the problem to be solved and the availability of necessary parameters (e.g., structural information and optical properties). Scientists have measured the optical properties of representative molecules and representative biological tissues [74,75]. The widespread scattering process in biological tissues changes the photon direction randomly following an angle distribution and prevents the deduction of light distribution within the tissue using the measurements outside of the tissue.

Different optical properties can be used to characterize light propagation. When the scattering process can be ignored, Beer-Lambert's law can provide an estimate of light distribution at different depths in tissue [76]:

$$I = I_o e^{[-\mu_a(\lambda) \cdot z]},$$

where I_o is the light intensity at the incident surface, μ_a is the absorption coefficient, and z is the depth along the light path. For scenarios where scattering is evident, several optical properties are defined to characterize the light propagation. The scattering coefficient, μ_s, is defined as the probability of a scattering event per unit length in a given medium. The anisotropy factor, g, is used to characterize the change of photon direction, which is the average of the cosine of scattering angles by a given scattering particle. An anisotropy factor can vary between -1 to 1, where 1 indicates that all of the photons are scattered forward, 0 indicates the scattering is happening isotropically and -1 indicates that all of the photons are scattered backward. To characterize the loss of light intensity due to scattering per given length, the reduced scattering coefficient, $\mu_s' = \mu_s \times (1 - g)$, is used [77]. For scenarios where scattering is present but the spatial distribution is not needed, μ_a can be replaced by the total extinction coefficient μ_t, which can be calculated

as $\mu_t = \mu_a + \mu_s$ to provide an estimate of light intensity at a given depth. Scientists have measured the optical properties of typical tissues, such as skin, muscle, fat, and brain [75,78,79] to estimate the optical properties of a given tissue.

2.2.5 Monte Carlo Simulation and diffusion theory

To get an estimate of the spatial light distribution in biological tissue, a Monte Carlo simulation of light propagation can be utilized. Monte Carlo simulation is a stochastic model which simulates the propagation of discrete packets of photons in a computational geometry that consists of many finite elements to approximate the geometry in the real world. Based on the light source's properties, packets of photons are launched with the initial packet weight, direction, and step length. For each step, the attenuation of the photon packet's weight is calculated based on the absorption coefficient of each finite element on the light path. Reflection and refraction are simulated whenever there is a refractive index mismatch between finite elements on the light path. If the photon packet is not considered as terminated (i.e., its weight is larger than the minimum weight threshold), the simulation will continue and the scattering coefficient and anisotropy factor will determine the next step length and direction. The simulation is repeated until the photon packet is terminated or the photon packet leaves the geometry being simulated. By simulating a vast number of photon packets, the summation of the light flux and absorption on each finite element can provide an estimate of the spatial and temporal light distribution in the simulated tissue. Recent works using graphical processing unit (GPU) acceleration of Monte Carlo simulation have greatly reduced the time needed for a simulation and permitted more detailed simulations [80,81]. While Monte Carlo simulation based on voxels can provide a good approximation of light propagation in layered biological tissues[82], recent work using mesh-based Monte Carlo simulation can provide a more accurate representation of the tissue geometry, especially for curved structures [83–

[85]. In a Monte Carlo simulation of highly scattering biological tissue, coherence, polarization, and nonlinearity are commonly neglected as they usually do not noticeably impact the light distribution. Depending on the power of incident light and the absorption coefficient, tissue heating during the light application can cause changes in the tissue's optical properties, which will require incorporating a thermal dynamic simulation into the workflow and updating the tissue's optical properties accordingly [86].

Further, when scattering is the dominant process and absorption is weak, the spatial light distribution in biological tissue can be approximated using Fick's law in diffusion theory [87,88]. The diffusion theory treats light propagation as the diffusing process of diffusive particles, which is not as computationally intensive as the Monte Carlo simulation.

2.3 Neuromodulation for selective neural inhibition

2.3.1 Electrical neuromodulation

Electrical neuromodulation has been the most commonly used non-pharmaceutical method to modulate neural activity. Examples of electrical neuromodulation include deep brain stimulation (DBS) for Parkinson's disease [89], spinal cord stimulation (SCS) for chronic pain [90], and vagus nerve stimulation (VNS) for epilepsy and depression [91]. Electrical nerve interfaces preferentially modulate large-diameter axons [92–95]. For example, in the simplified scenario of two parallel planar electrodes sandwiching an axon, the transmembrane potential evoked by extracellular electrodes is proportional to axon diameter and the small-diameter axons will experience a smaller extracellular voltage. [96,97]. To reverse the preference for the large-diameter axons, complex designs involving specialized multi-electrode layouts [98–100], waveforms [101], and frequencies [102,103] have been

promoted for both stimulation [104] and inhibition [102,103,105]. While these sophisticated designs improve their functionality, further improvements are needed. These designs are more likely to deal with problems such as electrode erosion and dislocation/rotation during long-term implantation, requiring repeated adjustments or even explant from the patient [89,106–108].

2.3.2 Thermally mediated neuromodulation modalities

Researchers have been exploring various physics modalities for selective neural block and comparing their effectiveness for pain management [109,110]. It has been known for decades that temperature has an impact on neural conduction [111]. The thermally-mediated neural inhibition includes both heat-based and cold-based neural inhibition and has been studied for its potential application in pain management [112]. The conventional heat-based neural block involves transcutaneous heat application (e.g., IR lamp, hot pad) and has been widely used to reduce pain [113,114]. It has been reported in rats [115] and humans [116,117] with systematic hyperthermia that the reflex response mediated by the small-diameter afferent fibers was suppressed. It has also been established that localized heat application induces neural conduction block in rat sciatic nerves [118,119], cat pudendal nerves (with heating after cooling) [120], and human median and ulnar nerves [121]. On other hand, inspired by the fact that sensory functions are impaired when the extremities of the human body are experiencing a low temperature, the cooling-based neural block (Cryotherapy) also has been developed for pain management [114,122]. Recent studies also showed that alternation between cooling and heating can lower the threshold of thermally-mediated neural block [120,123].

Other neural inhibition modalities can be affected by heat mechanisms. For example, studies have shown that high-frequency biphasic stimulation's blocking

threshold can be lowered by heating [124–127]. Recent studies showed that clinical kHz spinal cord stimulation and deep brain stimulation protocols can induce tissue temperature elevation as well [128–131]. Both findings show that tissue heating during high-frequency electrical stimulation may play a role in its function. Similarly, recent studies on ultrasound-based neural inhibition suggested that temperature elevation can be the mechanism [132–134]. Unfortunately, in those studies, the size selectivity of neural inhibition was not explored.

The depth of transcutaneous heat/cold penetration is limited to the subcutaneous region because of heat dissipation via the abundant blood flow through the deeper tissues [135]. Simply increasing the heat dose can cause nociceptive stimulation on the skin or even skin burns before raising the intramuscular temperature high enough for the neural block [135]. Other modalities like ultrasound [109,134] and radiofrequency [136,137] are being explored for their heating effect and the capability of the neural block. For those modalities, the advantage of generating heat inside tissue also caused difficulty in measuring tissue temperature and controlling the thermal dose. Therefore, radiofrequency has focused on applications via minimally invasive procedures for thermal ablation of neural tissue which does not require maintaining the temperature elevation within the safety margin [4,138–140]. Similarly, cryoablation has been applied for destructive denervation in the treatment of various diseases [141,142]. In addition, researchers also have demonstrated the possibility of selective ablation of the small-diameter axons via localized application of chemicals like capsaicin [143].

Naturally, thermally mediated neural inhibition is associated with the risk of thermal damage. From the experimental data on the peripheral nerves, the limitation of thermal dose that can be applied is 44 °C and 30 minutes or an equivalent dose at other temperatures [144]. Hyperthermia on the nerve can cause axonal oedema, vasculature alteration[145], and initiating the demyelination/degeneration of axons [144,146] . Both the

duration and the temperature of hyperthermia have an impact on the intensity of thermally-mediated neuronal damage [147]. Intensive acute heat stress on neurons can lead to apoptosis or necrosis via several potential pathways, including the activation of caspase, mitochondria damage (which can lead to accumulation of reactive oxygen species), and protein misfolding [147,148]. Injured/damaged axons can also be hypersensitive/hyperactive, which can lead to excitotoxic and cause neuronal cell death [147]. In contrast to the abundant studies on the hyperthermia of the central nervous system, local hyperthermia's effect on the peripheral nervous system is much less studied [148].

Overall, thermally mediated neural inhibition has the potential to be a promising neural inhibition modality, but several important considerations such as safety, tissue thermal load, and size selectivity must be addressed before it can be effectively translated into clinical applications.

2.3.3 Infrared neuromodulation

For many years, researchers have been investigating the feasibility of using light to modulate neural activities. Compared with other neuromodulation modalities, light can be tightly focused on the targeted region and minimize the potential to affect/damage the surrounding tissue. Before introducing infrared neuromodulation, which is the research focus of my Ph.D. project, I would like to review some other wavelengths and techniques that have been examined in this field first [149–151]. The invention of the laser enabled scientists to test and characterize the neuromodulation effect of intensive light [149,152]. Low-power near-infrared light has been explored for pain management [153,154], wound healing [155], and preventing muscle fatigue [156]. Optogenetics can help identify the critical molecular mechanism of neuropathic pain in animal models [157–160]. However, as it relies on gene editing and the introduction of exogenous agents, there are still many technical and ethical

challenges before it can be implemented in human patients. Our lab and collaborators have been studying infrared neuromodulation which does not rely on exogenous agents for the neuromodulation effect. Here is a brief review of the research on infrared neuromodulation, including infrared neural stimulation and infrared neural inhibition.

Infrared neural stimulation

In 2005, our collaborator from Vanderbilt University first demonstrated the *in vivo* neural stimulation by IR light [161,162]. Infrared neural stimulation has been used to evoke responses in rat's [163,164], and monkey's [165–168] brains for the mapping of neural circuits. Infrared light has also been used for the stimulation of cardiac potentials [169–171]. Infrared stimulation of the cochlear has been developed for over a decade with steadily improving selectivity and functionality [172–174], which has great potential to be a novel implantable solution to deafening [175–178]. Zhu *et al.* also demonstrated the safety of infrared neural stimulation in rat [166], whose results showed that the transient thermal elevation during infrared neural stimulation does not generate acute tissue damage. Using crayfish, Dr. Sanders' group demonstrated infrared inhibition and stimulation on individual neurons and the change in their excitability [179–182]. In addition, researchers have demonstrated that injecting exogenous agents, such as gold nano-particles [183,184], graphene [185], and macromolecular photothermal transducers [186], into the target neural tissue can help increase the localized absorption of infrared light, which can enhance the spatial selectivity and enable infrared neuromodulation in deep tissue [187].

Infrared neural inhibition

The following contents are adapted from a review article that I am the first author of and was accepted for publication in Frontiers in neuroscience – neural technology.

In 2012, Duke *et al.* first reported the inhibitory effect of pulsed infrared light application in *Aplysia* nerves, which they discovered while exploring temporal factors affecting the threshold of hybrid electro-optical stimulation [188]. The inhibitory effect was further explored in *Aplysia* since the anatomy of a buccal nerve and its branches make it tractable for testing the spatial selectivity of infrared neural inhibition (INI), as shown in Figure 2.2 [189]. They demonstrated that infrared (IR) laser light could transiently and reversibly induce inhibition in *Aplysia* axons with precise spatial selectivity. As illustrated in Figure 2.2, electrical stimulation was applied to the proximal buccal nerve trunk and recording was done at all three distal branches. When the infrared laser was applied concurrently with electrical stimulation to one region of the proximal nerve trunk, neural conduction to the corresponding branch was blocked. Once the INI protocol was explored on *Aplysia* axons (Figure 2.2, a - d), the investigators were able to use a nearly identical stimulation protocol to block action potential propagation on the tibial branch of the rat sciatic nerve (Figure 2.2, e - h). A roughly 9 °C temperature elevation was measured during the infrared light application on *Aplysia*. When the infrared laser was turned off, the temperature rapidly dropped, and the inhibitory effect ceased. According to the temporal response test by Lothet et al, the inhibitory effect of INI is caused by a baseline temperature elevation [8] rather than a spatiotemporal temperature gradient, which is critical for infrared neural stimulation [162].

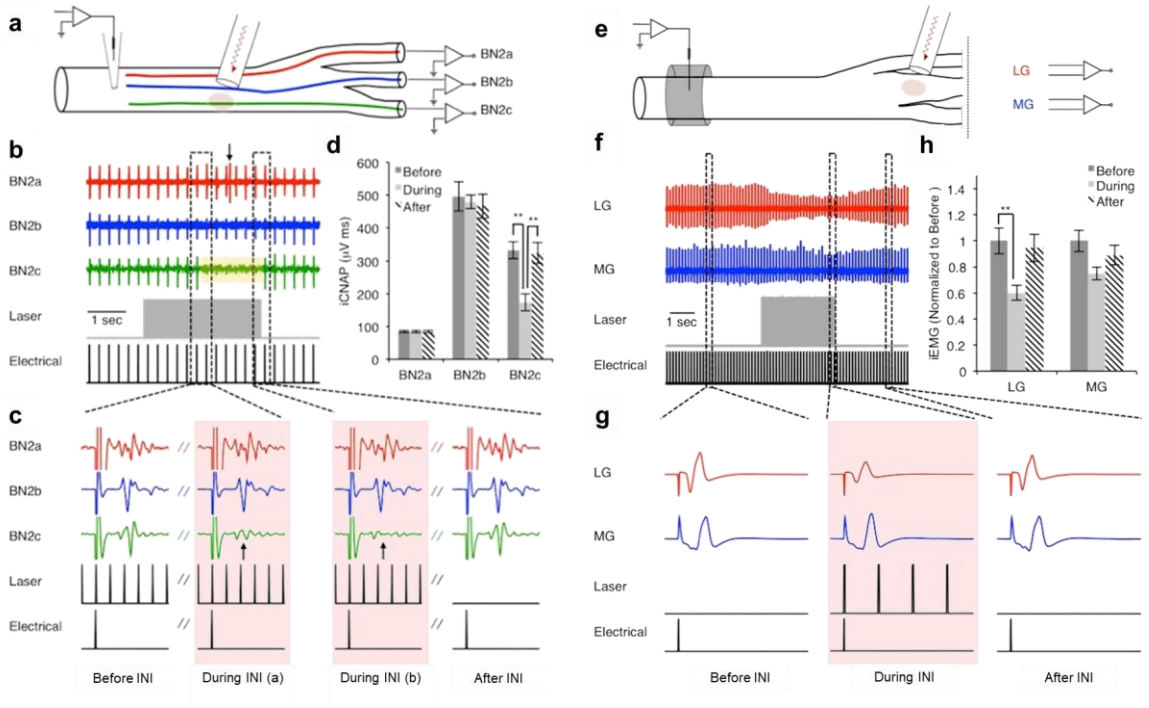

Figure 2.2. Nerve conduction block in buccal nerve 2 (BN2) of Aplysia (a to d) and in rat sciatic nerve (e to h).

Panel a to d: A train of low radiant exposure (0.50 ± 0.02 J/cm2), high frequency (200 Hz) infrared pulses (λ = 1450 nm, pulse width = 0.2 ms) produced a rise in local tissue temperature and blocked responses projecting to BN2c. Panel a: experimental setup; b: overall view of the recorded responses; c: representative signals showing the response before, during, and after the presence of infrared neural inhibition effect; d: calculated area under the curve showed the spatial selective inhibitory effect. Panel e to h: Similarly, applying infrared pulses (same temporal parameters, 75.7 ± 5.3 mJ/cm2) to the tibial branch of the rat sciatic nerve, approximately 1 cm distal to the site of electrical stimulation, reduced evoked EMG amplitude of the lateral gastrocnemius (LG) but not the medial gastrocnemius (MG). Panel e: experimental setup; f: overall view of the recorded responses; g: representative signals showing the response before, during, and after the infrared light application; h: calculated area under the curve showed the spatial selective inhibitory effect. [Reproduced with permission from (Duke et al., 2013). The original work is published under a Creative Commons Attribution-Noncommercial-NoDerivs 3.0 Unported License. To view a copy of this license, visit http://creativecommons.org/licenses/by-nc-nd/3.0/]

In 2017, Lothet *et al.* presented a general theory for how any modality (e.g., infrared neural inhibition) that acted on the axonal *surface* could scale with axon diameter and induce size selectivity [8]. When a neuromodulation modality primarily affects the ion

channels in the axon membrane, it was shown that the minimum required exposure length is proportional to the square root of the axon diameter. The theory suggested that small-diameter axons would be more susceptible to inhibition induced by baseline temperature elevation than large-diameter axons. To demonstrate this, Lothet *et al.* directly used individually identified neurons (B3 and B43) in *Aplysia* that had large and small diameter axons, respectively. As Figure 2.3 shows, the B3 and B43 neurons were electrically stimulated intracellularly while extracellular electrodes recorded propagation of their action potentials through a nerve both before and after an infrared laser application. When infrared light was delivered, only the small diameter axon was inhibited. The experiment was enabled by three unique features of *Aplysia* neurons. First, the average neuron size is larger than other commonly used mammalian neurons, making it easier to conduct intracellular stimulation. Second, there are a variety of neuron sizes accessible in the same ganglion, enabling the comparison between large and small-diameter axons. Third, those specific neurons with different sizes (B3 and B43) are identified and can be found across different individuals, making it possible to repeat the experiment with minimal variance. These features enabled the researchers to directly demonstrate the size-selectivity on small-diameter axons by infrared neural inhibition without ambiguity.

Furthermore, after establishing size-selectivity during INI using single neuron stimulation, the size-selectivity of INI was verified at the whole nerve level using compound action potentials (CAPs). When stimulating the whole nerve, action potentials from all axons with different diameters can be evoked simultaneously and propagate along the axons throughout the length of the nerve. The summation of those action potentials recorded extracellularly forms the CAP. In unmyelinated axons, conduction velocity is proportional to the square root of the axon diameter [190]. Therefore, as the CAP travels along the nerve, the latencies of different CAP components represent the response from

different axon-size subpopulations. The long nerves of *Aplysia* combined with the relatively slow conduction velocity of unmyelinated axons permit researchers to easily differentiate the response from different axon-size subpopulations. Lothet *et al.* developed a size-selective infrared neural inhibition protocol for small-diameter axons in *Aplysia* that was successfully transferred to the vagus nerve in the musk shrew *Suncus murinus* (Figure 2.4). Along with the protocol adaption from *Aplysia* to musk shrew, the baseline temperature elevation threshold of selective inhibition was reduced from ~9 °C to ~3 °C owing to the differences between species [8].

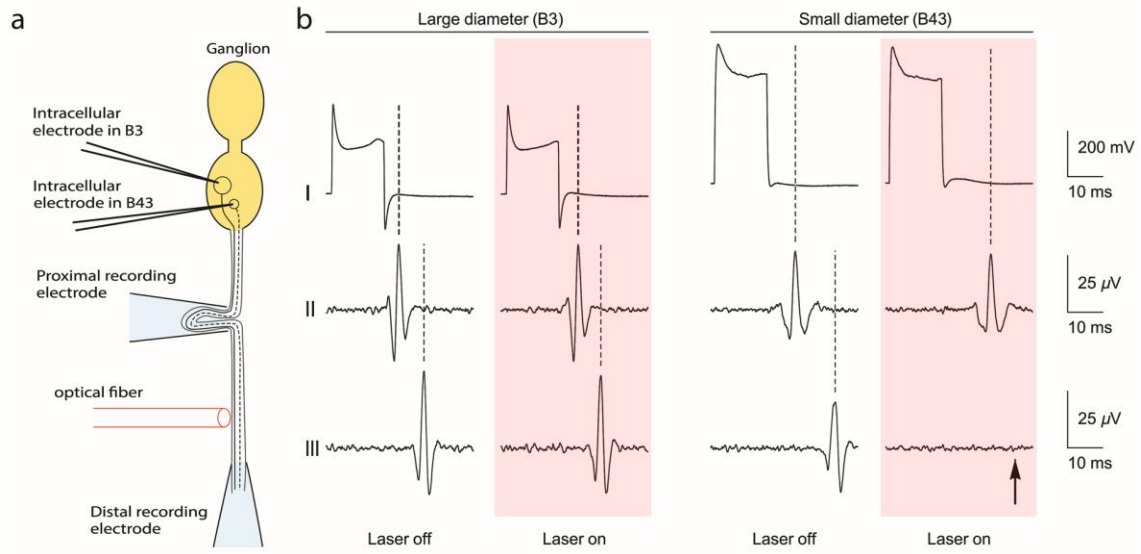

Figure 2.3. Direct demonstration of size-selective neural inhibition with B3 and B43 neurons in the Aplysia buccal ganglion.

Intracellular electrical stimulation was applied to a large-diameter neuron (B3) and to a small-diameter neuron (B43), both of which have axons that project through a common nerve. When infrared laser light was applied via an optical fiber that was positioned between two extracellular recording electrodes on the nerve, only the neural conduction on the small-diameter axon was blocked (indicated by arrow). [Reproduced with permission from Lothet et al. (2017). The original work is published under a Creative Commons Attribution 4.0 International License. To view a copy of this license, visit http://creativecommons.org/licenses/by/4.0/.]

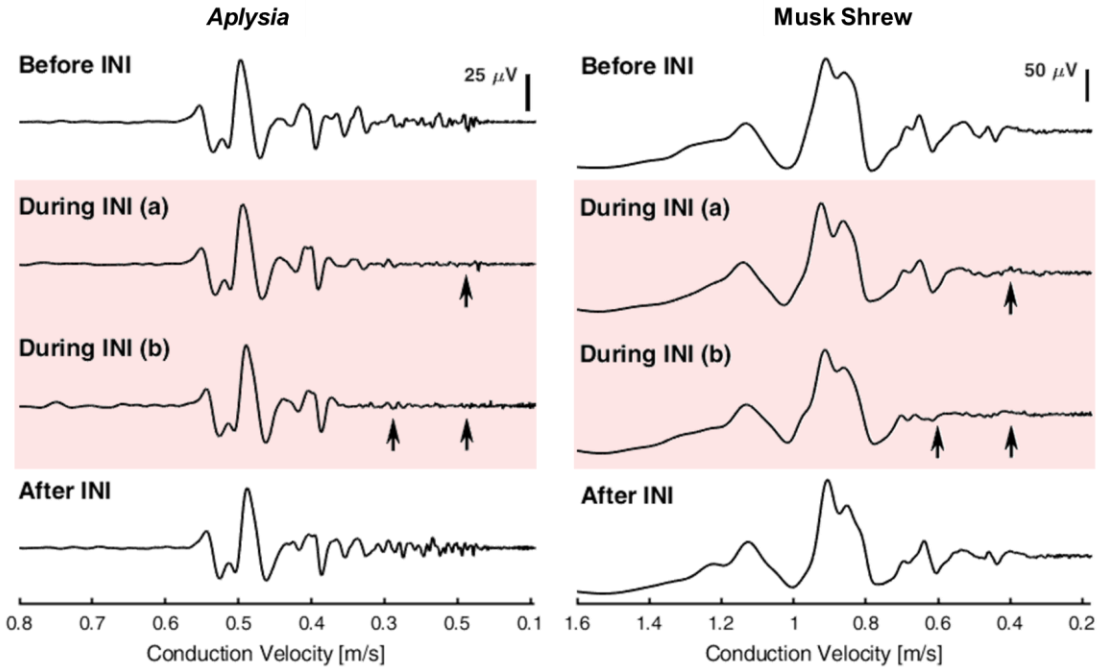

Figure 2.4. Demonstration of selective inhibition on small-diameter axons in Aplysia (left) and Musk Shrew (right).

Compound action potentials (CAPs) were evoked and recorded before, during, and after infrared neural inhibition (INI). Arrows indicate the selective inhibition effect on small-diameter axons that have a slower conduction velocity. The CAPs before and after INI remained similar, suggesting that the selective inhibition effect was reversible and the nerve's health was not compromised acutely. Reproduced with permission from Lothet et al. (2017). The original work is published under a Creative Commons Attribution 4.0 International License. To view a copy of this license, visit http://creativecommons.org/licenses/by/4.0/.]

In 2019, Ganguly *et al.* used a NEURON simulation of a squid giant axon to demonstrate that a likely mechanism for thermal inhibition was the acceleration of the kinetics of the voltage-gated potassium ion channels, resulting in a rapid *depolarization-activated hyperpolarization* due to elevated temperature (see Figure 2.5, a, b) [9]. They also showed that this inhibitory effect would be greater in smaller-diameter axons, as the mathematical model predicted in the previous research by Lothet *et al.* [8].

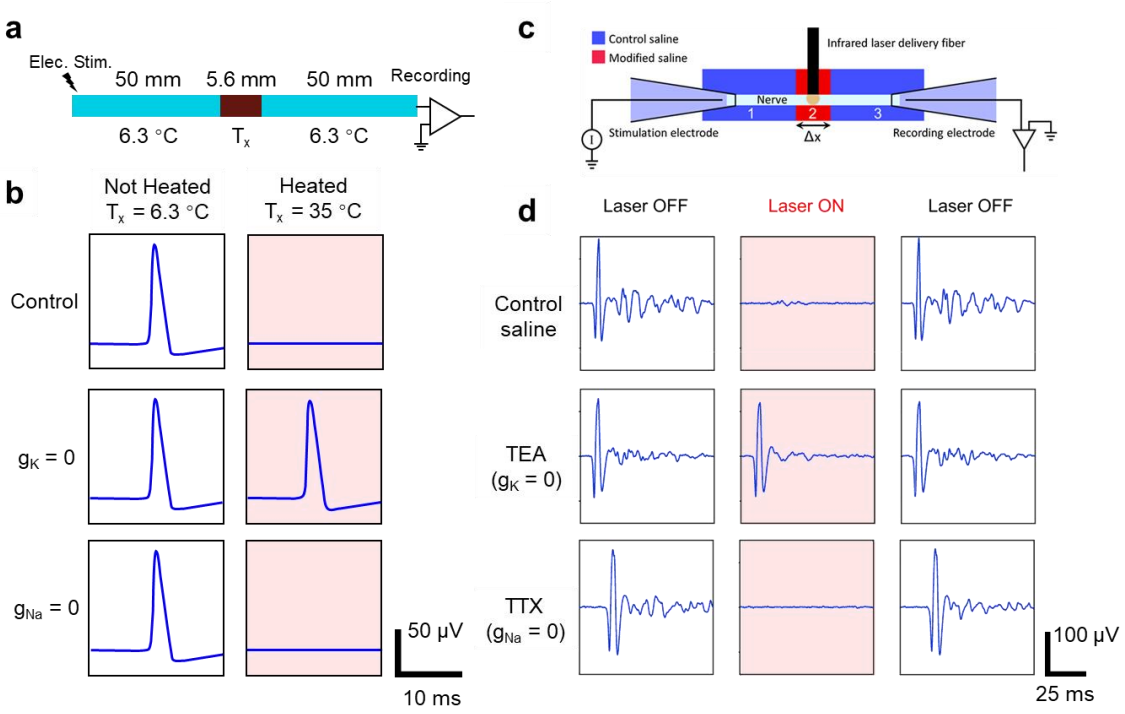

Figure 2.5. Computational modeling (a, b), and experimental validation in an Aplysia nerve (c, d) of the effect of blocking different ion channels on the heat-induced neural block.

(a) A schematic of a model axon with a central region where the temperature can be locally elevated (representing the thermal effect during IR application) and where the ion channel conductance can be set to zero (representing the local application of ion channel blocker). (b) The modeled action potential recordings under different conditions. Only when voltage-gated potassium channels are blocked (g_K = 0) is the heat-induced block effect reversed, suggesting that the heat-induced block requires voltage-gated potassium channels. (c) An experimental schematic of an ex vivo electrophysiology test of an Aplysia nerve. IR light was applied to the central region of the nerve, which was also exposed to modified saline with different ion channel blockers. (d) The recorded CAPs during different combinations of IR light application and ion channel blockers. In agreement with the modeling prediction, only when TEA was applied to block the voltage-gated potassium ion channels was the IR neural inhibition effect reversed. Reproduced from Ganguly et al. 2019 [9,10] with permission. The original works are licensed under the terms of the Creative Commons Attribution 3.0 License and Creative Commons Attribution 4.0 Unported License respectively. See license detail at https://creativecommons.org/licenses/by/3.0/ and https://creativecommons.org/licenses/by/4.0/]

In the same year (2019), Ganguly *et al.* then provided experimental evidence for the hypothesis using *Aplysia* nerves (see Figure 2.5, c and d) [10]. As the *Aplysia* axon and

squid giant axon are both unmyelinated axons with different diameters, the qualitative conclusions from the modeling work should apply directly to *Aplysia* axons. As Figure 2.5d shows, selectively blocking voltage-gated potassium ion channels (using TEA) eliminated the thermal inhibition, whereas blocking voltage-dependent sodium ion channels (using TTX) did not prevent thermal inhibition. Thus, experimental evidence from *Aplysia* confirmed the modeling work based on the squid giant axon and demonstrated that the infrared neural inhibition relies on the accelerated potassium-channel kinetics during baseline temperature elevation induced by the absorption of infrared light in the nerve.

These studies were extended by Ford *et al.* showing that one could reduce the IR dose required for thermal inhibition by illuminating a greater length of the nerve [191,192], and by Zhuo *et al.* showing that ion substitution could also reduce the dose of laser light needed for thermal inhibition (included in chapter 3) [193]. Most recently, Zhuo *et al.* have demonstrated that selective IR inhibition can be reproduced by resistive heating (included in chapter 4) [194]. Further studies are needed to apply this thermally mediated selective inhibition in both basic neuroscience research and potentially translational applications.

2.4 *Aplysia* as the animal model

The majority of the research in this thesis is conducted on *Aplysia californica*, which is a robust animal model for developing novel neuromodulation technologies that can selectively inhibit small-diameter axons. This session briefly describes the aspects of *Aplysia's* physiology that make it advantageous for developing novel neuromodulation modalities and neural interfaces. The following contents in this section are adapted from my first-author review article:

Zhuo J, Gill JP, Jansen ED, Jenkins MW and Chiel HJ (2022) Use of an invertebrate animal model (*Aplysia californica*) to develop novel neural interfaces for neuromodulation. Front. Neurosci. 16:1080027. doi: 10.3389/fnins.2022.1080027

2.4.1 *Aplysia* neurophysiology

New tools for monitoring and manipulating neural activity will be critical for understanding the function of neural circuits and for treating nervous system diseases. In recent years, many new approaches have been developed whose functionality, specificity, and reliability have steadily improved. Here we review the use and utility of an invertebrate animal, the marine mollusk *Aplysia* californica, to develop novel neural interface technologies for recording and/or modulating neural activities. After briefly describing the advantages of *Aplysia*'s physiology for developing novel neural interfaces, we will focus on a specific example that illustrates the power of *Aplysia* for accelerating technology development: using heat to selectively inhibit small-diameter unmyelinated axons.

In the 1960s, *Aplysia*'s large, pigmented neurons attracted the attention of neuroscientists who wanted to better understand the biophysical properties of individual neurons. Early studies demonstrated that the neurons could be repeatedly and reliably identified by their location and anatomy, their electrophysiological properties, their synaptic inputs and followers, their biochemical properties, and their functional roles as sensory neurons, motor neurons, and interneurons [195,196]. The neurons' somata (cell bodies) are very large (about 30 to 500 µm in diameter). A major advantage of *Aplysia*'s neuron is that its soma is electrically compact just like vertebrate neurons [197,198], allowing the neurites to be electrically manipulated from a single control point. In contrast, arthropod neurons (e.g., crustacean and insect neurons) are often not electrically compact and their somata are not often excitable [199]. Thus, in *Aplysia*, researchers can easily

monitor neuronal activity via the somata, which is the largest and most accessible part of the cell. Furthermore, because the *Aplysia* neuron's somata are electrically excitable, activating or inhibiting neurons at these locations can turn the rest of the neuron on or off, making it possible to test the ability of novel neural interfaces to monitor and manipulate individual identified neurons in a neural circuit. The neurons are arranged in groups (referred to as ganglia) that generally contain ~2000 neurons. The entire nervous system contains approximately 20,000 neurons. Studies of neural circuitry and behavior in *Aplysia* have clarified the neural, biophysical, and molecular basis of learning and memory [200,201], sleep [202,203], and complex behaviors such as mating [204] and feeding [205,206]. Many novel technologies can take advantage of the deep understanding of neural circuitry controlling behavior in *Aplysia* to study the effects of manipulating single neurons or small numbers of neurons on behavior in both reduced preparations and intact, behaving animals.

2.4.2 Advantages and examples of using *Aplysia* for developing novel neural interfaces

In addition to the advantages that led researchers to initially use *Aplysia's* nervous system in their work, there are several other reasons to use *Aplysia*. Here, we highlight the rationale for using *Aplysia* for the development of novel interface technologies that focus on monitoring or manipulating axons.

First, *Aplysia* does not produce myelin, providing a model animal where the conclusions based on the Hodgkin-Huxley model and its variants can be directly tested in the laboratory, as Ganguly *et al.* did in 2019 regarding the critical role of voltage-gated potassium channels during INI [9,10]. *Aplysia* nerves connect the different ganglia which consist of many neurons that have been identified previously. The nerve bundle consists of populations of unmyelinated axons whose diameters range from less than one μm to

over ten µm. Thus, one can examine the effects of a variety of techniques for manipulating axonal activity in a pure population of unmyelinated axons that vary greatly in diameter. This makes the animal a particularly useful model of the unmyelinated C fibers in vertebrates that are known to carry important sensory information, including those that signal pain.

One example is how *Aplysia* nerves helped researchers explore the feasibility of selective neural inhibition using high-frequency alternating current (HFAC), which has been studied for decades for its capability to reversibly and repeatedly block neural conduction in frogs, rats, and cats [95,207,208]. From computational simulations and experimental studies, it was believed that the block threshold (i.e., minimum HFAC amplitude required) increases monotonically with frequency for all nerve fibers, and those small-diameter axons would therefore have a higher block threshold than larger-diameter axons. These observations suggested that it would be impossible to selectively inhibit small-diameter axons with HFAC, as it would primarily block the large-diameter axon first. However, a more recent experiment on unmyelinated *Aplysia* axons [105] showed that, once the HFAC frequency was higher than 12 kHz, the block threshold of these unmyelinated small-diameter axons would begin to decrease, instead of constantly increasing as previously believed. Therefore, the findings from this *Aplysia* experiment provided the theoretical basis for selective inhibition of different axon types with different frequencies. In other words, with a high enough HFAC frequency, the block threshold for small-diameter axons could be decreased to be lower than the threshold for large-diameter axons, which would permit selective inhibition of small-diameter axons. This hypothesis for selective inhibition was successfully verified in frogs and rats [102,103]. Additionally, researchers also used *Aplysia* to demonstrate the possibility of combining HFAC with infrared neural inhibition (INI) to block the onset response during HFAC application [209].

Second, neural tissue harvested from *Aplysia* can be kept viable with active neural signaling for many hours. The reason is that *Aplysia* lives in the intertidal zone. Thus, unlike many marine animals that live in the ocean, *Aplysia* is regularly found in tide pools that are exposed to significant changes in temperature, salinity (e.g., high salinity as pools dry out and low salinity during rain), and tidal surge. Since the animals do not maintain a fixed body temperature, and their soft bodies readily change volume in response to osmotic changes, their nervous systems, which are exposed to the animal's open circulatory system, are very robust. Excised musculature and nervous systems from *Aplysia* can be maintained without anesthesia at room temperature. The excised tissue respires slowly, so it can be studied for many hours without significant changes in function. Although rarely mentioned in research articles, this advantage greatly extends the experimental time and increases the ability to collect data from the same animal, collect longitudinal data, and limits data noise due to inter-animal variance. These advantages are especially important for novel neural modulation technologies, as researchers need to explore the parameter space to identify an effective configuration.

For example, Duke *et al.* developed a sophisticated experimental design with *Aplysia* nerve consisting of four electrodes and two optical fibers, which they used to establish their INI protocol and demonstrate its capabilities [189]. As the authors wrote in their paper, "hours of intermittent stimulation" was done and the response was stable without visibly identifiable damage or significant change in the physiological recordings. Later in the process of optimizing the infrared neural inhibition threshold, both Ford *et al.* and Zhuo *et al.* have explored the parameter space of INI protocols, which required a substantial number of repeated experiments on the same nerve to avoid variation between animals [192,193]. Furthermore, in the research of comparing the dose-response curve between resistive heating and INI, Zhuo *et al.* applied both heating modalities with different

levels of power on the same nerve sequentially and compare the responses [194]. The robustness of the *Aplysia* preparation enabled those studies to be conducted in a reasonable amount of time and with a minimal number of animals.

The *Aplysia* nerve's robustness is not limited to thermally mediated neuromodulation. It has been demonstrated that focused ultrasound (FUS) applied to the central nervous system can stimulate or inhibit neural activity in a wide range of vertebrate animal models, but the optimal paradigm for each type of effect is still yet to be determined due to the complexity of neural circuits in the brain [210,211]. In contrast, *Aplysia* ganglia consist of much smaller numbers of neurons and therefore provide a more tractable animal model for researchers to study. It has been reported that FUS can alter the excitation level of *Aplysia* neurons [212]. In recent studies, an *ex-vivo* FUS testing system used an isolated *Aplysia* ganglion and connected nerve, enabling the researchers to thoroughly explore the FUS parameter space on the same ganglion, and investigate the mechanisms of action [213].

Third, in large *Aplysia*, the nerves between the ganglia may be many centimeters in length. The nerve length makes it possible to easily discriminate large-diameter axons from small-diameter axons based on the conduction velocity difference. When stimulating a nerve, a compound action potential (CAP) can be evoked, which is the summation of action potentials conducted on all the different axons. Since axonal conduction velocity decreases proportionally to the square root of axon diameter in unmyelinated axons, by the time the CAP reaches the other end of the long nerve, it naturally separates into different components. Researchers can explore the size selectivity of a given neuromodulation modality based on the response from different CAP components.

In addition, *Aplysia* neurons are large and can be repeatedly identified, which has been used to develop novel single-cell neural interfaces. *Aplysia* neurons have been used to develop both diamond electrodes [214] and carbon fiber microelectrodes [215]. In both studies, *Aplysia* was selected as the animal model since there are neural circuits that are thoroughly studied with standard electrophysiological methodologies that can be used as the gold standard for comparison. The surgical procedures are also simpler than in rats, mice, or other vertebrate animals, so that iterations of the novel neural interface design can be tested rapidly to quickly achieve the goal.

Overall, these results demonstrate that *Aplysia* californica as a tractable experimental system has several unique advantages: Neurons that can be repeatedly identified and excited; neural tissues that can last for a long period in an *ex vivo* experimental setup; nerves consisting of pure unmyelinated axons with different diameters; and neural circuits that are well-studied and that permit different levels of experimental design (from single neuron tests to whole behavioral tests). Generally, *Aplysia* is suitable for testing modalities in which the basic biophysics of that modality is likely to be similar across species (e.g., responses to temperature or changes in ionic concentration), and during initial tests of novel modalities in which the exploration of parameter spaces and the determination of fundamental mechanisms are likely to be broadly applicable across species. Previous studies have demonstrated that novel technologies that interface with and manipulate the nervous system can be developed using *Aplysia* and then migrated to vertebrate animals [8,189]. As a tractable experimental system, *Aplysia californica* can help the rapid development of novel neuromodulation technologies.

Chapter 3. Isotonic ion replacement combined with infrared neural inhibition

3.1 Preface

This chapter presented the effort to lower the threshold of selective infrared neural inhibition. Section 3.2 was published as:

> Zhuo, J., Ou, Z., Zhang, Y., Jackson, E. M., Shankar, S. S., McPheeters, M. T., ... & Jenkins, M. W. (2021). Isotonic ion replacement can lower the threshold for selective infrared neural inhibition. Neurophotonics, 8(1), 015005.

This work was inspired by both the previous hypothesis by Lothet et al. that a modality that primarily acts on the axon membrane will have a selectivity on the small-diameter axons and the modeling and experimental work by Ganguly et al. showing that thermally-accelerated voltage-gated potassium ion channels are critical for the selective infrared neural inhibition effect. This work discussed how isotonic ion replacement with glucose and/or choline can lower the power threshold for infrared neural inhibition and maintain the size selectivity on the small-diameter axons. The presented work of IR inhibition combined with isotonic ion replacement can guide further development of a more effective size-selective IR inhibition modality for future research and translational applications.

3.2 Isotonic ion replacement can lower the threshold for selective infrared neural inhibition

Junqi Zhuo [1], Zihui Ou [2], Yuhan Zhang [2], Elizabeth M. Jackson [2], Sachin S. Shankar [1], Matthew T. McPheeters [1], Jeremy B. Ford [3, 4], E. Duco Jansen [3, 4, 5], Hillel J. Chiel [1, 2, 6], and Michael W. Jenkins [1, 7]

Abstract

Significance: Infrared (IR) inhibition can selectively block peripheral sensory nerve fibers, a potential treatment for autonomic-dysfunction-related diseases (e.g., neuropathic pain and interstitial cystitis). Lowering the IR inhibition threshold can increase its translational potential. **Aim:** Infrared induces inhibition by enhancing potassium channel activation. We hypothesized that the IR dose threshold could be reduced by combining it with isotonic ion replacement. **Approach:** We tested the IR inhibition threshold on the pleural-abdominal connective of *Aplysia californica*. Using a customized chamber system, the IR inhibition was applied either in normal saline or in isotonic ion-replaced saline, which could be high glucose saline, high choline saline, or high glucose/high choline saline. Each modified saline was at a subthreshold concentration for inhibiting neural conduction. **Results:** We showed that isotonically replacing ions in saline with glucose and/or choline can reduce the IR threshold and temperature threshold of neural inhibition. Furthermore, the size selectivity of IR inhibition was preserved when combined with high glucose/high choline saline.

[1] Case Western Reserve University, Department of Biomedical Engineering, Cleveland, Ohio, United States
[2] Case Western Reserve University, Department of Biology, Cleveland, Ohio, United States
[3] Vanderbilt University, Department of Biomedical Engineering, Nashville, Tennessee, United States
[4] Vanderbilt University, Biophotonics Center, Nashville, Tennessee, United States
[5] Vanderbilt University, Department of Neurological Surgery, Nashville, Tennessee, United States
[6] Case Western Reserve University, Department of Neurosciences, Cleveland, Ohio, United States
[7] Case Western Reserve University, Department of Pediatrics, Cleveland, Ohio, United States

3.2.1 Introduction

Inhibition of peripheral nerves can be useful for treating disease (e.g., pain,[216] persistent hypertension,[217] or obesity [218]). We showed that infrared (IR) light can block action potential propagation in both neural and cardiac tissues [8,188,189,219] and others have confirmed these findings [179,220–223]. Unlike IR stimulation, which depends on spatiotemporal thermal gradients $(dT/dt, dT/dz)$ [169,224–227], studies suggest that IR inhibition is due to an IR-induced baseline temperature increase [228]. Recently, we showed that temperature increases lead to rate increases in Hodgkin–Huxley gating mechanisms so that the K^+ channel activation rate overwhelms the Na^+ channel activation rate [9,10]. We have modeled, experimentally demonstrated, and mathematically proven that IR inhibition can preferentially block action potential propagation in small-diameter sensory fibers [8–10].

We have explored ways to apply IR inhibition effectively and safely for translational applications [191]. We showed that IR inhibition is safe and reversible in previous acute studies [8,219]. In addition to optimizing the IR inhibition protocol (e.g., changing the block length [191]), we are exploring whether other inhibition modalities could be combined to reduce the IR threshold. For example, combining IR with electrical current lowered the threshold for IR neural stimulation [188,226]. Similarly, we hypothesized that adding another inhibitory modality could reduce the IR inhibition threshold, enhancing potential translational applications.

Since IR inhibition speeds up the gating of voltage-gated potassium channels [9,10], adding a different modality that works via the axon membrane, such as affecting the voltage-gated sodium channels, could demonstrate synergy. Glucose block, which replaces isotonic glucose solution for normal saline, has been used for safe and reversible neural conduction inhibition since the 1930s [229–232]. Similarly, choline chloride has been used for

sodium-ion substitution. Using the pleural-abdominal connective of *Aplysia californica*, we tested the hypothesis that replacing part of the saline with isotonic glucose or choline solution can reduce currents through ion-selective channels and lower the IR inhibition threshold. An additional test with both glucose and choline was conducted to explore if there is any synergetic effect on the IR threshold reduction when both isotonic ion substitutions were used.

3.2.2 Method

Animal Preparation

We used the pleural-abdominal connectives from *Aplysia californica* (298 $\pm$ 58 g, South Coast Bio-Marine, California), a nerve that consists solely of unmyelinated axons. The nerve on both sides was dissected after anesthetizing the animal with magnesium chloride solution (333 mM, 50% body weight). Nerves were kept in normal *Aplysia* saline (460 mM NaCl, 10 mM KCl, 10 mM MOPS, 10 mM glucose, 22 mM $MgCl_2 \cdot 6H_2O$, 33 mM $MgSO_4 \cdot 7H_2O$, 13 mM $CaCl_2$, pH 7.5) at room temperature ($\sim$22°C).

Experimental Setup

a. Electrophysiology

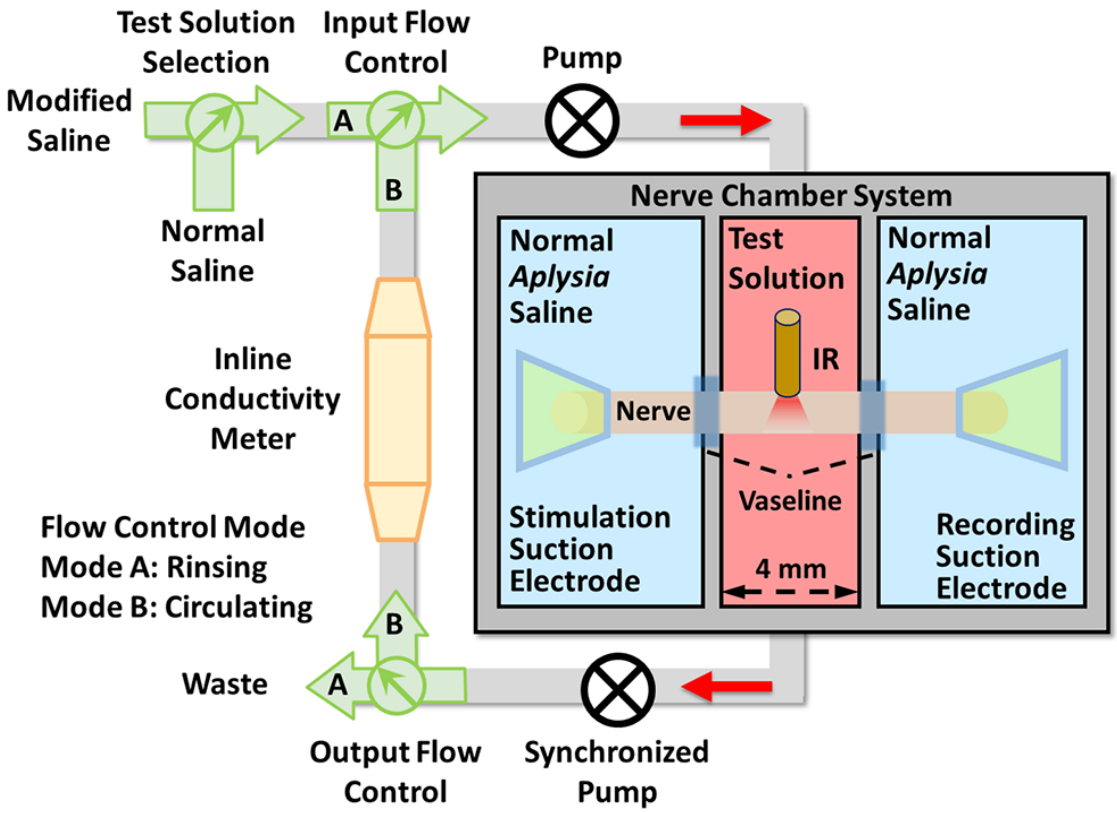

Figure 3.1. The experimental setup.

The system shown schematically makes it possible to position a nerve across three isolated chambers. In the two outer chambers, the nerve was stimulated and recorded using suction electrodes in normal Aplysia saline. In the middle chamber, a 600-µm optical fiber in contact with the nerve delivered IR light at the same time that the nerve could be bathed in either normal saline or modified saline. The modified saline could be high glucose saline, high choline saline, or high glucose/ high choline saline, each of which was at a subthreshold concentration for inhibiting neural conduction. Perfusion of either the modified saline or normal Aplysia saline was monitored by an inline conductivity meter.

Electrical stimulation and recording via suction electrodes (0.35-mm inner diameter) were used to assess neural conduction (Figure 3.1). The nerve was stimulated with bipolar electrical current pulses (1 Hz, 2 ms, 0.1 to 0.5 mA) generated by a pulse stimulator (Model 2100, A-M Systems, Washington) and delivered by a stimulus isolator (A395, World Precision Instruments, Florida). The current was adjusted to ensure that a full compound action potential (CAP) was evoked. The evoked CAPs were amplified and band-pass

filtered (×10; 000, 100 to 500 Hz) by a differential ac amplifier (Model 1700, A-M Systems, Washington). The amplified signal was recorded by a data acquisition (DAQ) device (USB-6003, National Instruments, Texas) using the AxoGraph X software (AxoGraph, California).

b. Modified saline and fluid control

In the chamber system, the test nerve was placed in a groove that went across three chambers, while the middle chamber was perfused with different solutions using a peristaltic pump (7524- 10, Barnant Co, Illinois), allowing the simultaneous application of both inhibitory modalities (Figure 3.1). The solution was either normal *Aplysia* saline (in which the standard glucose concentration is 10 mM/L) or one of the modified saline solutions:

1. High glucose saline: 20% v/v of isotonic glucose solution mixed with 80% v/v normal *Aplysia* saline, in which all the ion concentrations were diluted to 80% of the level in normal *Aplysia* saline. The elevated glucose concentration (235 mM/L) was the minimum level that did not cause significant inhibition or spontaneous activity in our preliminary test. In the same test, the threshold for acute inhibition with glucose was 1105 ± 20 mM/L ($N = 5$, data not shown).

2. High choline saline: 20% v/v of isotonic choline chloride solution mixed with 80% v/v normal saline. The choline chloride concentration (113 mM/L) was selected to match the osmotic concentration of the additional glucose in the high glucose saline, so the dilution to the other ions was the same (80%). Since we are using choline chloride, the chloride concentration was maintained instead of being diluted, which does not have a significant effect on neural conduction.

3. High glucose/high choline saline: 10% v/v of isotonic glucose solution and 10% v/v of isotonic choline chloride solution mixed with 80% v/v normal saline. The dilution of other ions was the same as the 80% level (except that it was 90% for chloride). In this modified saline, concentrations of the added glucose and choline were cut in half (glucose: 121 mM/L, choline: 57 mM/L).

Normal *Aplysia* saline was used in the two outer chambers. The chambers were isolated using Vaseline Petroleum Jelly (Unilever, Connecticut. We incorporated a conductivity meter (CON6+, OAKTON Instruments, Illinois) into the perfusion line to monitor the solution's concentration based on the conductivity difference between the modified saline and normal *Aplysia* saline, which is caused by the dilution of ion concentrations. The solution in the middle chamber was considered correctly perfused when a stable conductivity reading equal to the reference value of the modified saline was achieved. All test solutions were kept at room temperature (~22°C) during the experiment for consistent conductivity measurements.

c. Laser

The IR light was generated by a single-mode laser diode (λ = 1485 nm, QFBGLD-1480-500, QPhotonics, Michigan) driven by a diode driver and thermoelectric cooler controller (6340-4A, Arroyo Instruments, California). The laser was coupled into a 600-μm multimode optical fiber (P600-5 VIS-NIR, Ocean Insight, Florida), which was held in direct contact with the nerve by a micromanipulator. The 10-second laser pulse train (1250 Hz, 400 μs pulse width) was triggered by a DAQ device (USB-6218, National Instruments, Texas). Radiant exposure level was calculated using the average power measured by a power meter (PS19Q, Coherent, California).

Thermal Measurements

To measure the IR-induced temperature rise under different IR thresholds, we used a thermal camera (FLIR A325sc, Oregon) to measure the temperature distribution of an approximated midplane solution as previously reported [8,219]. In brief, we cut a Petri dish along its midline and covered the cut end with a thin flat cover glass. The dish was filled with normal *Aplysia* saline or modified saline to mimic the experimental conditions. A 600-*μ*m optical fiber was positioned vertically aiming downward so that its enface diameter was bisected by the glass–water interface and in contact with the cover glass's upper edge. With calibration, the measured temperature distribution on the outer surface of the thin cover glass is an approximation to the actual mid-plane temperature distribution in the solution. When the laser light was applied through the fiber, we extracted the maximum temperature from the thermal distribution to represent the thermal condition that a nerve may experience during the IR application. The same IR parameters as applied in the inhibition experiments were used to determine temperature changes induced by IR inhibition alone versus IR inhibition combined with glucose.

Experimental Design and Analysis

We used separate groups of nerves to test the hypothesis that the IR inhibition threshold can be lowered by combining each type of isotonic ion-replaced saline. Using high-glucose saline as an example, here are the testing steps: (1) verify that high-glucose saline could not induce inhibition; (2) identify the IR threshold (I_{combined}) for inhibition when IR was applied along with the high-glucose saline in the middle chamber; (3) verify that the identified IR threshold (I_{combined}) in the previous test was a subthreshold IR level that alone could not induce inhibition; (4) identify the IR threshold (I_{IR}) in normal *Aplysia* saline. Control tests to generate CAPs in normal *Aplysia* saline before and after all the inhibition tests were conducted to assess the nerve's health. More specifically, in each 105-second experimental

trial, three 10-second applications of IR light were applied at the 10th, 45th, and 80th seconds of the trial. The IR power was carefully ramped up across trials to identify the IR threshold for inhibition.

We calculated and compared the rectified area under the curve (RAUC) of the CAPs to verify that the IR thresholds under different testing solutions correspond to the same inhibition level. Since heat accumulates during the first 6 seconds, only the CAPs from the 7th to 10th second of each IR application were analyzed. For the initial and final trials without IR application, CAPs at identical time points were used, which helped take account of the very gradual rundown of the CAP due to electrical stimulation over time. To make a comparison of inhibition strength across nerve samples, the average RAUC of each nerve's response at the designated time points was normalized to the average RAUC of the first 10 CAPs of its first normal saline control test. For each group of nerves tested with given modified saline, we compared the IR thresholds in the modified saline versus in normal saline, once the normalized RAUC response confirmed the consistency of IR inhibition strength. A one-tailed t-test was conducted on the IR thresholds to see if it was lowered by the given modified saline. Finally, we calculated the percent change of the IR threshold as follows:

$$Percent\ Change\ of\ IR\ threshold = \left(\frac{I_{combined}}{I_{IR}} - 1\right) \times 100\ (\%). \quad (1)$$

We conducted an ANOVA test on those percentage changes in IR threshold under different types of modified saline to explore if there was a preferable method. For the quantification and statistical analysis of size selectivity, we used the same method as previously described [8]. The CAPs were divided into fast-conducting and slow-conducting regions at a point of low variability. To be more specific, because all axons were stimulated simultaneously by the suction electrode, the latency of the CAP subcomponents arriving at the recording electrode was inversely proportional to the conduction velocity. For

unmyelinated axons, large-diameter axons typically have a higher conduction velocity and are responsible for motor output, whereas smaller axons have a slower conduction velocity and are responsible for sensory input [233]. Therefore, we separated the CAP signal into two subpopulations, fast- and slow-conducting axons, based on latency, which allowed us to examine the selective inhibition effect across different axon subpopulations, as has been done in previous research [8,192].

The segmentation of CAPs was done by defining the two outer boundaries that cover the whole duration of the CAP, and an inner boundary between the fast- and slow-conducting subpopulations. Although the general CAP shape and conduction velocity distribution remain similar across nerves, the conduction velocity can shift over time owing to fatigue [234], temperature [111], or variance across preparations. As a consequence, the segmentation boundaries of CAPs were detected by a custom algorithm and manually inspected for each nerve. The outer boundaries of the CAPs were detected as the CAP signal amplitude rises/falls beyond the normal range of background noise (mean ± 3*standard deviation). The inner boundary between the fast- and slow-conducting subpopulations was selected by determining the minimum value for the variance across heating trials. This minimized the fluctuation caused by the shift of CAP subcomponents across the inner boundary.

Next, we calculated the normalized RAUC within each region using the defined boundary between the fast- and slow-conducting regions. For both fast and slow regions, we categorized a region as inhibited during a given CAP only when the normalized RAUC was lower than 0.6. Twenty-eight CAPs (four per animal) were analyzed for each type of modified saline. The chi-squared test was used to compare the inhibition effect on fast-conducting large-diameter axons and slow-conducting small-diameter axons.

3.2.3 Results

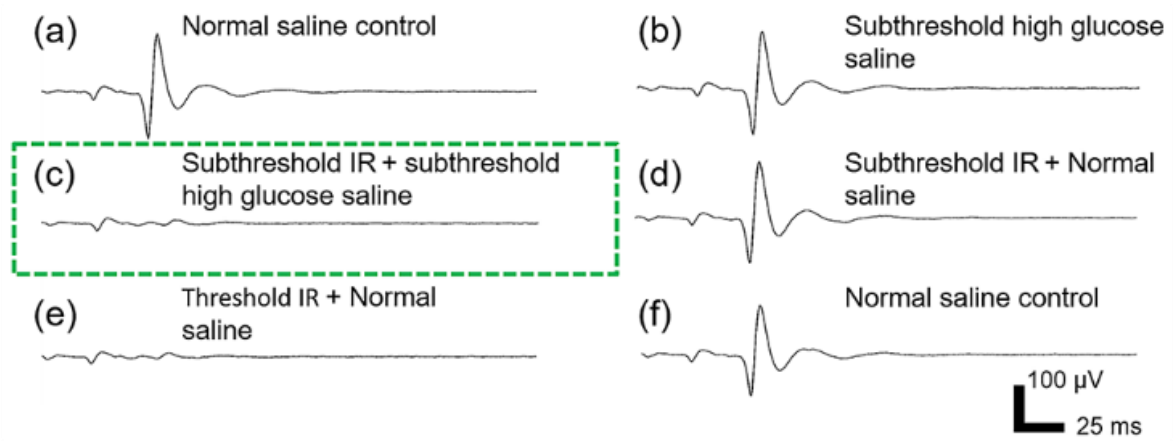

Figure 3.2. Representative data of the test of combined inhibition effect.

A typical raw data set shows that subthreshold IR combined with subthreshold high glucose saline can achieve full inhibition similar to the threshold level IR alone in normal saline. a) A normal saline control experiment elicited a full CAP from electrical stimulation. b) Subthreshold high glucose saline did not elicit a significant inhibitory effect. c) When subthreshold IR was combined with subthreshold high glucose saline, an almost full inhibitory effect was observed. d) When the same subthreshold IR level was applied alone, it did not show a significant inhibitory effect. e) When IR was applied in normal saline alone, a higher power level was needed to induce an inhibition effect similar to panel c. f) A normal saline control test after all the tests showed a CAP similar to panel a, suggesting the nerve's health was not affected.

All three types of subthreshold ion-replaced saline were able to lower the IR inhibition threshold. For example, Figure 3.2 shows a typical dataset in which the IR inhibition threshold was lowered by high glucose saline. As positive controls, neither subthreshold high glucose saline nor subthreshold IR radiant exposure (12.2 mJ/cm^2) alone could inhibit the CAPs (Figure 3.2 b and d). In contrast, when the same subthreshold IR radiant exposure was combined with the subthreshold high glucose saline, full inhibition was achieved (Figure 3.2 c). The radiant exposure threshold for IR inhibition alone in normal *Aplysia* saline was higher (13.7 mJ/cm^2, Figure 3.2 e). The CAPs in the normal saline control tests before and after inhibition tests (Figure 3.2 a and f) did not show an obvious difference. The experiments were repeated seven times for high glucose saline and the

normalized RAUC results are shown in Figure 3.3.

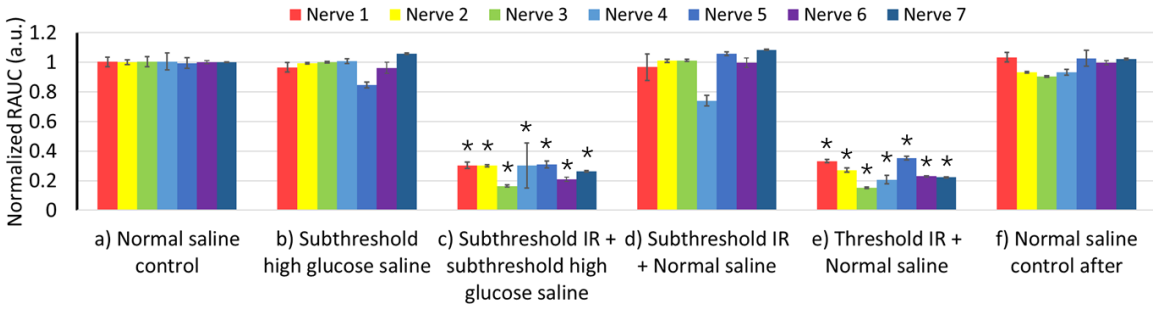

Figure 3.3. Normalized RAUC results from seven nerves.

For each nerve, the absolute RAUC number was normalized to the averaged RAUC from the first 10 CAPs of the initial normal saline control experiment. Group b and d show little to no inhibition with a RAUC well above 0.6, suggesting that both subthreshold high glucose saline and subthreshold IR cannot inhibit the action potential conduction alone. Both groups c and e show a strong inhibitory effect (normalized RAUC < 0.6, p< 0.05 for paired test with the control group a) suggesting that the combined modality (c) can achieve a similar inhibition as IR alone (e) but requiring lower IR levels. The nerve's health was not affected by the different treatments as groups a and f did not show significant differences.

The RAUC result confirmed that IR combined with high glucose saline achieved the same inhibitory effect as IR alone, but required lower IR levels. A paired t-test between the combined inhibition and IR inhibition (Figure 3.3 c and e) did not show a significant difference ($p = 0.539$). Neither subthreshold modality lowers the RAUC below 0.6, a level we considered as obvious inhibition (Figure 3.3 b and d). The RAUC for the two control tests (Figure 3.3 a and f) did not show a significant difference in the paired t-test ($p = 0.274$). Thus, inhibition tests did not significantly affect the nerve's health. The same RAUC analysis was conducted on the results from the high choline saline group and high glucose/ high choline saline group, and our paired t-tests showed consistent inhibition between groups c and e for each type of modified saline. This enabled accurate measurements of the reduction in IR threshold or temperature.

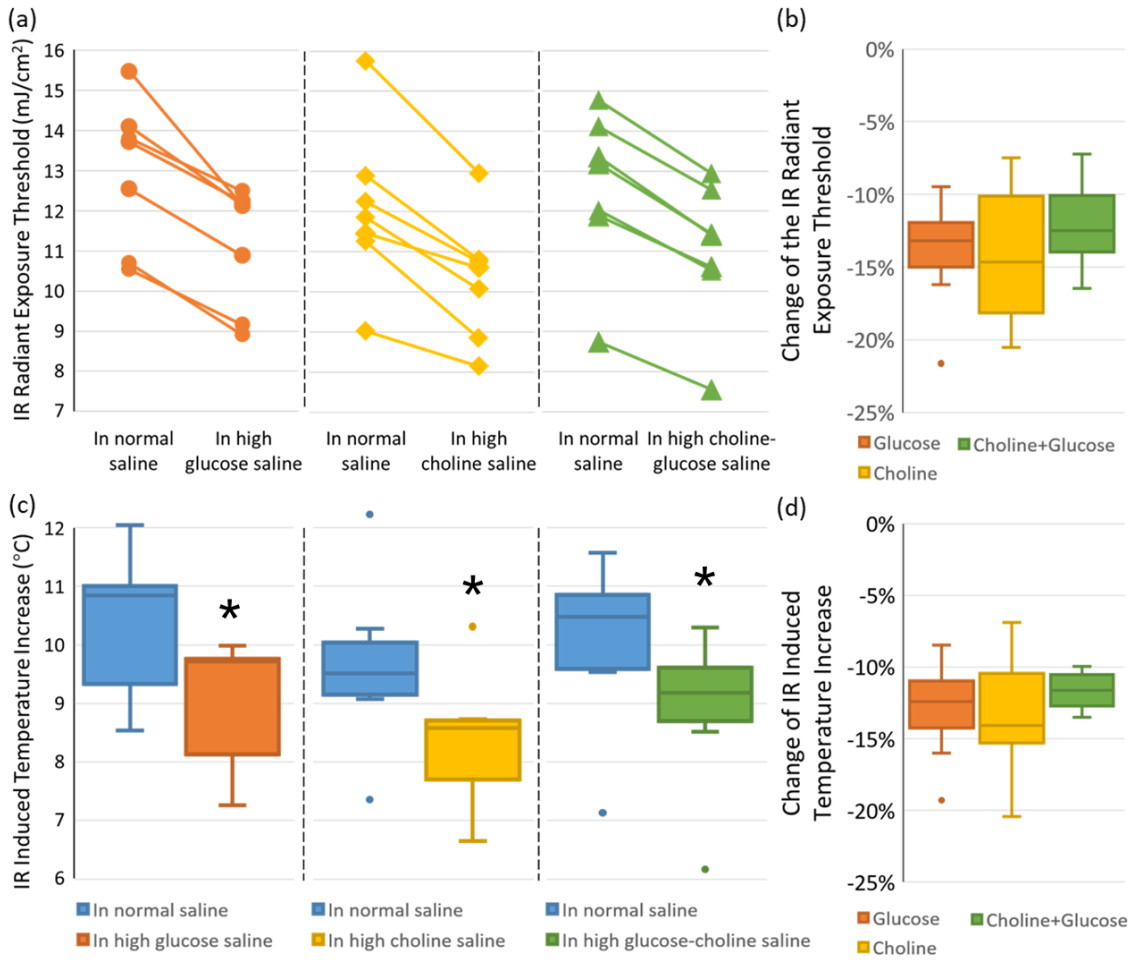

Figure 3.4. The IR radiant exposure threshold and the IR-induced maximum temperature change in normal Aplysia saline versus in each type of isotonic ion-replaced saline.

(a) The IR radiant exposure threshold for inhibition in each type of isotonic ion-replaced saline showed a significant drop compared with the threshold in normal Aplysia saline. Each line indicates a pair of IR thresholds tested on the same nerve in different conditions. IR radiant exposure thresholds for inhibition were significantly lower (one-tailed t-test, $p < 0.05$) in all three types of ion-replaced saline than in normal Aplysia saline (b) The changes in IR thresholds were not significantly different between different types of modified saline. A one-way ANOVA test of the IR threshold changes across different types of modified saline did not show a significant difference ($p = 0.724$). (c) The box-whisker plot of maximum IR-induced temperature rise showed a significant drop when IR is applied in each type of modified saline compared with the reading in normal Aplysia saline. The thermal camera measurement showed a significant drop (one-tailed t-test, $p < 0.05$) of the IR-induced maximum temperature rise in all three types of modified saline compared to the temperature needed for IR alone in normal Aplysia saline (d) The changes in IR-induced maximum temperature increase were not significantly different between different types of modified saline. A

one-way ANOVA test of the temperature threshold changes across different types of modified saline did not show a significant difference (p = 0.653).

IR radiant exposure thresholds for inhibition were significantly lower (one-tailed t-test, $p < 0.05$) in all three types of ion-replaced saline than in normal *Aplysia* saline (Figure 3.4 a). The percentage changes in the IR threshold were: 14.1 ± 3.7% for high glucose saline, 14.3 ± 4.5% for high choline saline, and 12.6 ± 1.3% for high glucose/ high choline saline (Figure 3.4 b). A one-way ANOVA test of the IR threshold changes across different types of modified saline did not show a significant difference ($p = 0.724$). The thermal camera measurement showed a significant drop (one-tailed t-test, $p < 0.05$) of the IR-induced maximum temperature rise in all three types of modified saline compared to the temperature needed for IR alone in normal *Aplysia* saline (Figure 3.4 c). The percentage changes of the IR-induced maximum temperature rise were: 12.9 ± 3.4% for high glucose saline, 13.3 ± 4.1% for high choline saline, and 11.7 ± 1.3% for high glucose/ high choline saline (Figure 3.4 d). A one-way ANOVA test of the temperature threshold changes across different types of modified saline did not show a significant difference ($p = 0.653$).

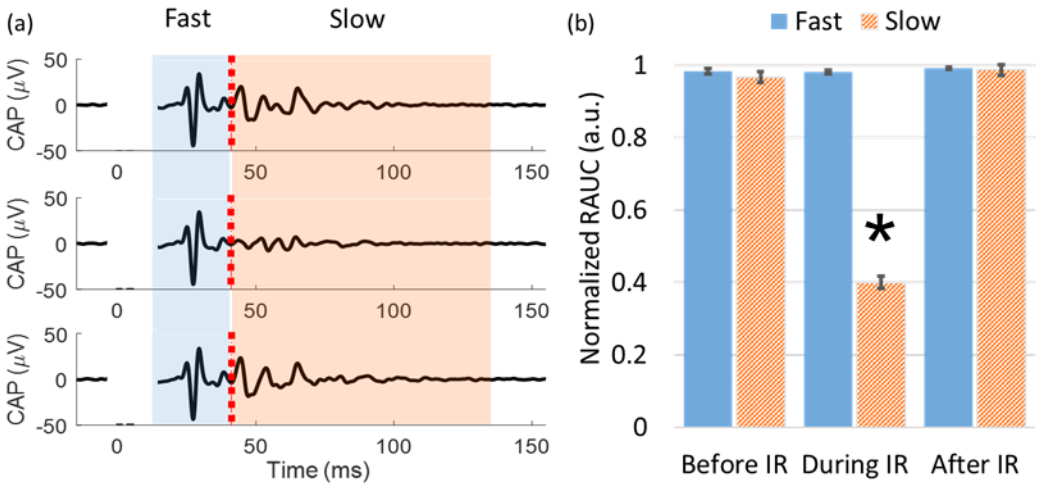

Figure 3.5. Selective inhibition on slow-conducting small-diameter axons when IR was applied in subthreshold high glucose/ high choline saline.

(a) Partial block of the compound action potential (CAP) components carried by the slower-conducting small-diameter axons. From top to bottom is the CAP before, during, and after the

partial block. The red dashed line indicates the low variability point for separation. The artifact caused by electrical stimulation was blanked. (b) The normalized RAUC quantification in panel b showed that only the slow components were significantly inhibited by the IR application, two-sample t-test ($p < 0.05$).

Selective inhibition of slow-conducting small-diameter axons was observed with each type of isotonic ion-replaced saline. A typical CAP is shown in Figure 3.5 a for IR combined with high glucose/ high choline saline. As shown in Figure 3.5 b, the fast-conducting components carried by the large-diameter axons were not inhibited while the slow-conducting components carried by the small-diameter axons were inhibited (two-sample t-test, $p < 0.05$). For all three types of modified saline, we conducted the same RAUC calculation and categorization of the fast/slow components of the CAPs during IR application. After the categorization, the cumulative number of CAPs in response to the IR application combined with each type of modified saline is shown in Table 3.1.

Table 3.1. Cumulative number of categorized CAPs when IR was applied in combination with different types of isotonic ion-replaced saline

Type of modified Saline	**Type of response**	**Number of CAPs**	
		Fast-conducting, large-diameter	Slow-conducting, small diameter
High glucose saline	Uninhibited	18	4
	Inhibited	10	24
High choline saline	Uninhibited	24	0
	Inhibited	4	28
High glucose-high choline saline	Uninhibited	24	8
	Inhibited	4	20

Using chi-squared tests, all three types of modified saline showed statistically significant inhibition preference in the slow-conducting regions as compared to the fast-

conducting regions ($p < 0.05$ for all three groups). This suggests that the size-selectivity of IR inhibition was preserved when combined with isotonic ion-replaced saline which is similar to our previous results using IR alone [8].

3.2.4 Conclusion and Discussion

The results confirmed our hypothesis that combining IR inhibition with isotonic ion replacement by glucose and/or choline can lower the required radiant exposure threshold for IR inhibition. The combined method can lower the IR-induced temperature increase, which can potentially reduce the risk of damage due to acute IR-induced heating. More importantly, the size selectivity on small-diameter axons of IR inhibition was preserved when combined with isotonic ion replacement. The combined method appears to be safe in the acute setting since the inhibition effect is reversible after each inhibition modality.

For all three types of modified saline, we observed a similar reduction effect on the IR threshold, suggesting that the similar level of dilution to the ions in the modified saline was the major reason for the reduction effect. These results are consistent with our previous mathematical analysis [8] that any modality (e.g., isotonic ion replacement used in the combination here) that primarily works on the membrane will selectively affect small-diameter axons. It is important to point out that when glucose and choline were both applied in half the osmotic concentrations that they had been applied alone, the modified saline still induced a similar reduction in IR threshold as the reduction when glucose or choline was applied alone. This finding provides a basis for future studies using several solutes for isotonic ion replacement to lower the IR inhibition threshold, keeping each solute within safe concentrations. It has not escaped our notice that diabetes patients already have an elevated glucose level that is 2 to 4 times higher than normal, which can make neural conduction more vulnerable and cause chronic neuropathy or functional toxicity [235–237]. Oral administration of phosphatidylcholine as a choline supplement has shown a maximum ~4

times elevation of plasma choline concentration [238]. Therefore, it may be feasible to lower the threshold for IR inhibition or other heating modalities to treat the neuropathic pain caused by diabetes by the administration of choline and/or other ion-substitution solutes, in addition to the already elevated glucose level.

The present work is an acute study of IR inhibition combined with isotonic ion replacement. To accurately find the IR threshold for each condition, six tests were performed (see Figure 3.3), which took multiple rounds of IR application and fluid changing. This experimental design allowed us to measure two IR inhibition thresholds for each nerve: one in the normal saline and one in the test solution while ensuring that the nerve's health remained consistent (e.g., control tests did not show significant differences in RAUC) throughout the experimental process. The results confirmed that the selected substrate concentrations, although higher than therapeutic levels [239], were safe for the present acute *ex vivo* tests. More importantly, those acute tests demonstrated that isotonic ion replacement can lower the IR threshold regardless of the substrate or substrate mix used for the ion replacement. This finding will serve as the basis for further chronic studies of IR inhibition combined with isotonic ion replacement to explore: (1) the stability of the isotonic ion-replaced saline's reduction effect on the IR inhibition threshold over the repeated test; (2) multiple ion-replacement compounds, in combination, could be used at concentrations that were suitable for potential translational applications; (3) the ratio between the inhibition threshold and the damage threshold in normal saline versus in isotonic ion-replaced saline.

Infrared neuromodulation has been combined with other modalities to lower the IR threshold. For example, Duke et al [226]. demonstrated that combining electrical and IR neural stimulation (INS) could reduce the threshold for INS. Our data highlight the potential practical benefit of combining IR inhibition with other inhibitory modalities. The

combination of IR inhibition with isotonic ion replacement lowered the IR threshold and the related temperature rise while preserving the size selectivity on the small-diameter axons. These results will guide the development of a more effective size-selective IR inhibition modality for future research and translational applications.

Chapter 4. Resistive heating for size-selective neural inhibition

4.1 Preface

This chapter presented the work of reproducing the infrared neural inhibition's size-selectivity via resistive heating. Section 4.2 was published as:

> Zhuo, J, Weidrick, C. E., Liu, Y., Moffitt, M. A., Jansen, E. D., Chiel, H. J., Jenkins, M. W. (2023). Selective IR neural inhibition can be reproduced by resistive heating. Neuromodulation: Technology at the Neural Interface, (accepted)

This work was motivated by the need for an implantable system to test localized heat application on the peripheral nerve *in vivo*, both acutely and chronically. The overall energy efficiency of neural inhibition systems based on infrared light applications is limited by the conversion efficiency from electricity to infrared light at the laser diode. This has been greatly improved over the past years and remains 25% or lower for the wavelength we have been using (e.g., 1470 nm and 1860 nm). This efficiency limitation makes it difficult to design a battery-powered implantable infrared neural inhibition system for *in vivo* tests. On top of that, infrared light delivery relies on optical fibers that are much stiffer than biological tissues and can cause difficulties for implantable device design. We were inspired by Dr. Ganguly's modeling and experimental work showing that the thermally accelerated temporal dynamics of voltage-gated potassium ion channels is the mechanism of infrared neural inhibition [9,10]. In other words, other heating modalities should be able to reproduce the inhibition effect induced by the infrared neural inhibition protocol. More importantly, with the mathematical analysis in the supplemental material of the size-selective inhibition demonstration paper by Lothet et al. [8], we were expecting that other

heating modalities should be able to reproduce the size-selectivity on the small-diameter axons. We selected resistive heating as the alternative heating modality as it has great energy efficiency in converting electricity to heat. Although we were not able to make the whole implantable thermally-mediated neural inhibition system for an in-vivo test, owing to time limitation and fabrication capabilities, the *ex vivo* results proved the feasibility of designing such a system for inducing size-selective inhibition on the small-diameter axons with resistive heating. To our knowledge, this is the first comprehensive comparison between infrared neural inhibition and resistive heating for size-selective neural inhibition.

4.2 Selective IR neural inhibition can be reproduced by resistive heating

Junqi Zhuo, MS[2]; Chloe E. Weidrick, BA; Yehe Liu, PhD[1]; Michael A. Moffitt, PhD[1]; E. Duco Jansen, PhD[3,4,5]; Hillel J. Chiel, PhD[6,7,1]; Michael W. Jenkins, PhD[1,8]

Abstract

Objectives: Small-diameter afferent axons carry various sensory signals that are critical for vital physiological conditions but sometimes contribute to pathologies. Infrared (IR) neural inhibition (INI) can induce selective heat block of small-diameter axons, which holds potential for translational applications such as pain management. Previous research suggested that IR-heating-induced acceleration of voltage-gated potassium channel kinetics is the mechanism for INI. Therefore, we hypothesized that other heating methods, such as resistive heating (RH) in a cuff, could reproduce the selective inhibition observed

[2] Department of Biomedical Engineering, Case Western Reserve University, Cleveland, OH, USA
[2] Department of Nutrition, Case Western Reserve University, Cleveland OH, USA
[3] Department of Biomedical Engineering, Vanderbilt University, Nashville, TN, USA
[4] Biophotonics Center, Vanderbilt University, Nashville, TN, USA
[5] Department of Neurological Surgery, Vanderbilt University, Nashville, TN, USA
[6] Department of Biology, Case Western Reserve University, Cleveland OH, USA
[7] Department of Neurosciences, Case Western Reserve University, Cleveland, OH, USA
[8] Department of Pediatrics, Case Western Reserve University, Cleveland, OH, USA

by INI. **Materials and Methods:** We conducted *ex vivo* nerve heating experiments on pleural-abdominal connective nerves of *Aplysia californica* using both IR and resistive heating. We fabricated a transparent silicone nerve cuff for simultaneous IR heating, RH, and temperature measurements. Temperature elevations (ΔT) on the nerve surface were recorded for both heating modalities, which were tested over a range of power levels that cover a similar ΔT range. We recorded electrically evoked compound action potentials (CAPs) and segmented them into fast and slow subcomponents based on conduction velocity differences between the large and small diameter axonal subpopulations. We calculated the normalized inhibition strength and inhibition selectivity index based on the rectified area under the curve (RAUC) of each subpopulation. **Results:** INI and RH showed a similar selective inhibition effect on CAP subcomponents for slow-conducting axons, confirmed by the inhibition probability vs. ΔT dose-response curve based on approximately two thousand CAP measurements. The inhibition selectivity indices of the two heating modalities were similar across six nerves. RH only required half of the total electrical power required by INI to achieve a similar ΔT. **Significance:** We show that selective INI can be reproduced by other heating modalities such as resistive heating. Resistive heating, because of its high energy efficiency and simple design, can be a good candidate for future implantable neural interface designs.

4.2.1 Introduction

Selective inhibition of small-diameter axons is a critical and unmet medical need. Small-diameter nerve fibers carry various sensory signals that are critical for the homeostasis of vital physiological conditions [27,240]. Selective inhibition of small-diameter axons has the potential to treat various diseases (e.g., pain [216], obesity [218], and hypertension [217]) that are difficult to treat using conventional pharmaceuticals [2]. The current use of local anesthetics

cannot reliably induce selective block of small-diameter fibers [241,242] while the use of systemic drugs, in particular opioids, has numerous deleterious side effects [56,243].

Traditional electrode-based neuromodulation can induce neural block but has had limited success in preferentially blocking small-diameter axons. Examples include direct current (DC) nerve block [94,97] and high-frequency alternating current stimulation (HFAC) [244,245]. These neuromodulation modalities preferentially block large-diameter efferent axons because the transmembrane potential evoked by the extracellular electrode is proportional to the axon diameter [96,97]. Therefore, selective inhibition of small-diameter axons requires additional effort, such as changing the stimulation frequency of HFAC [102,103]. The small-diameter axon selectivity can be further degraded due to electrode corrosion and dislocation during chronic implantation [246,247]. There is still a need for a selective neuromodulation modality for small-diameter axons.

We have previously shown that infrared (IR) neural inhibition (INI) can selectively inhibit the small-diameter slow-conducting nerve fibers [8]. This is achieved using IR light (e.g., $\lambda \sim 1470$ nm, 1550 nm, and 1860 nm) with a high water absorption coefficient. INI can inhibit the propagation of both neural [8,182,188,189] and cardiac action potentials [219]. In addition to size selectivity, IR light can also achieve spatial selectivity of fine structures (e.g., neurons) to explore their functionality [180,220–222]. At the same wavelength, infrared neural stimulation (INS) can be achieved using a spatial-temporal thermal gradient caused by the absorption of short IR pulses [169,224–227]. In contrast, INI relies on the IR-induced baseline temperature elevation that causes thermal acceleration of K+ channel kinetics to block neural conduction [9,10,228]. The power threshold for INI can be lowered by changing the length of the axon along which IR is applied [191,192] or by isotonic extracellular ion replacement [193] while maintaining the size selectivity during inhibition. In addition, other IR

wavelengths have been used to modulate neural activity in vertebrate animals [166,180,183,248–250].

Heat-induced inhibition of neural conduction has been reported in previous studies. Hodgkin and Katz reported a heat-induced neural block effect on giant squid axons in 1949 [111]. Direct heat application induces neural conduction block in rat sciatic nerves [118,119], cat pudendal nerves (with heating before cooling) [120,123], and human median and ulnar nerves [121]. Other neural inhibition modalities are affected by heating. For example, studies have shown that high-frequency biphasic stimulation's blocking threshold can be lowered by heating [124–127]. Recent studies showed that clinical kHz spinal cord stimulation and deep brain stimulation protocols can also induce tissue temperature elevation [128–131]. Both findings indicated that the heating effect during high-frequency electrical stimulation may be related to its mechanism of action. Similarly, recent studies on ultrasound-based neural inhibition suggested that temperature elevation may be the mechanism [132–134]. Unfortunately, in those studies, the size selectivity of neural inhibition was not explored. But it has been reported in rats [115] and humans [116,117] that during hyperthermia, the reflex response mediated by the small-diameter afferent fibers was suppressed. Previous studies also suggested that the selective inhibition effect during INI was heat-based [8–10].

Therefore, we hypothesized that selective inhibition with INI could be reproduced using another heating modality, resistive heating (RH). In this study, we developed a nerve cuff for RH and temperature monitoring. We compared the inhibition strength under different temperature elevations (dose-response) and the selective inhibition as a function of axon diameter in response to INI and RH on the pleural-abdominal connective nerve in *Aplysia californica*, a preparation consisting solely of unmyelinated axons of varying diameters. We selected RH as the representative heating modality, primarily because it can be designed to minimize the spatial variance of induced temperature elevation. In addition,

RH can be applied in a relatively simple design and could have better energy efficiency than INI. These advantages could facilitate the further development of battery-powered implantable devices, increasing the availability of selective inhibition of small-diameter axons for basic research and translational applications.

4.2.2 Materials and Methods

Animal Model

We tested our hypothesis *in vitro* (N = 6) on the pleural-abdominal connective nerve of *Aplysia californica* (278 ± 40 g, South Coast Bio-Marine, CA). Although the use of *Aplysia*, an invertebrate animal, does not require Institutional Animal Care and Use Committee (IACUC) approval, we ensured that animals were fully anesthetized before extracting nerves, and then were euthanized with an excess of anesthetic (magnesium chloride). The *Aplysia* nerve consists only of unmyelinated axons with large and small diameters, because *Aplysia* does not make myelin. This provides a robust testing platform for exploring the relationship between the inhibitory effect and axonal size differences without having to consider the effects of myelination [8,105]. While further studies and parameter optimization would need to be carried out when translating selective block by RH to vertebrate neurons, our previous work has shown that IR-based heating translates directly from *Aplysia* to vertebrate systems (rat and musk shrew) at much smaller values of ΔT. [8,188,189].

Electrophysiological recording

Customized suction electrodes (0.35 mm inner diameter) were printed using a 3D printer (Form 3, Formlabs, MA, USA) for electrical stimulation (2 Hz with 2 ms symmetric biphasic current pulses, 1 ms per phase) and compound action potential (CAP) recording. The stimulation pulsing signal was generated using a pulse stimulator (Model 2100, A-M

Systems, WA, USA) and converted into current pulses using a stimulus isolator (A395, World Precision Instruments, FL, USA). The current was adjusted for each nerve between 0.3 – 0.5 mA to ensure full recruitment of all CAP components. The evoked CAPs were amplified and filtered (×10,000, 100–500 Hz) using a differential AC amplifier (Model 1700, A-M Systems, WA) and digitized with a data acquisition (DAQ) device (USB-6003, National Instruments, TX, USA) at 5000 Hz sampling rate using AxoGraph X software (AxoGraph, CA, USA). The nerve was placed in a chamber filled with *Aplysia* saline (460 mM NaCl, 10 mM KCl, 10 mM MOPS, 10 mM glucose, 22 mM $MgCl_2 \cdot 6H_2O$, 33 mM $MgSO_4 \cdot 7H_2O$, 13 mM $CaCl_2$, pH 7.5) at room temperature (~20 °C) to sustain the health of the nerve during the experiments.

2.3 Resistive heating (RH)

We fabricated heating cuffs by embedding nichrome heating wires (#761500, 25.4 µm bare diameter, A-M Systems, WA, USA) between two layers of medical grade polydimethylsiloxane (PDMS) tubing (#60-011-05 and #60-011-08, Dow Corning, MI, USA) for the application of RH. Figure 4.1 (a) illustrates the heating cuff design and the constructed heating cuff is shown in Figure 4.1 (c) and (d). Here are the fabrication steps of the miniature resistive heating cuff:

1) The outer PDMS tube (1.575 mm inner diameter, McMaster-Carr, OH, USA) was cut axially and unwrapped into a flattened sheet; 2) the nichrome heating wire (#761500, 25.4 µm bare diameter, A-M Systems, WA, USA) was sewed into the unwrapped outer PDMS tube; 3) the outer PDMS tube was re-wrapped around the inner PDMS tube (1.016 mm inner diameter, McMaster-Carr, OH, USA); 4) the thermocouple (5SC-TT-T-40-36, dia. = 200 µm, Omega Engineering, CT, USA) was sewn through both layers of the PDMS tube and placed on the inner surface of the cuff; 5) the inner cuff was cut along the slit of the outer PDMS tube; 6) the entire heating cuff assembly was

encapsulated with silicone adhesive (KWIK-SIL, World Precision Instruments, FL, USA) while using a steel pin (0.024 in. diameter, McMaster-Carr, OH, USA) as the place holder for the nerve; 7) A slit was cut through all layers of material along the existing cut of the outer PDMS tube; 8) the pin was removed to leave an opening for the nerve after curing the silicone adhesive; and 9) excessive silicone adhesive was trimmed away.

The fabricated heating cuff has the following dimensions: an inner diameter of 0.7 mm; an outer diameter of 4.3 mm and an overall length of 10.1 mm. A ~4.5 mm (longitudinal) region of the core channel was surrounded by the embedded heating wire and the heated length of the nerve will be slightly longer than that due to thermal diffusion. A thermocouple (5SC-TT-T-40-36, dia. = 200 µm, Omega Engineering, CT, USA) was embedded using silicone adhesive (KWIK-SIL, World Precision Instruments, FL, USA) on the inner side of the heating cuff to measure the temperature of the nerve surface. Two multi-strand copper wires (30 American-wire-gauge) were used to connect the heating cuff to the temperature controller. The total DC resistance (including the connection wires) was 40.1 Ω, including a 3.0 Ω resistance of the contacts and a 37.1 Ω resistance of the heating wire embedded in the cuff. A modified temperature controller (TC-324C, Warner Instruments, MA, USA) was used to control the direct current level passing through the heating wire. See supplemental materials for the fabrication process and the relationship between direct current level and temperature elevation (Figure 4.2). The heating cuff was applied by sliding a nerve into the core channel of the heating cuff via the slit. The heating circuit was fully insulated and driven by direct current instead of alternating current to minimize the chance of interfering with electrophysiological recordings. Figure 4.2 showed the relationship between the direct current applied and the induced temperature elevation at the nerve surface.

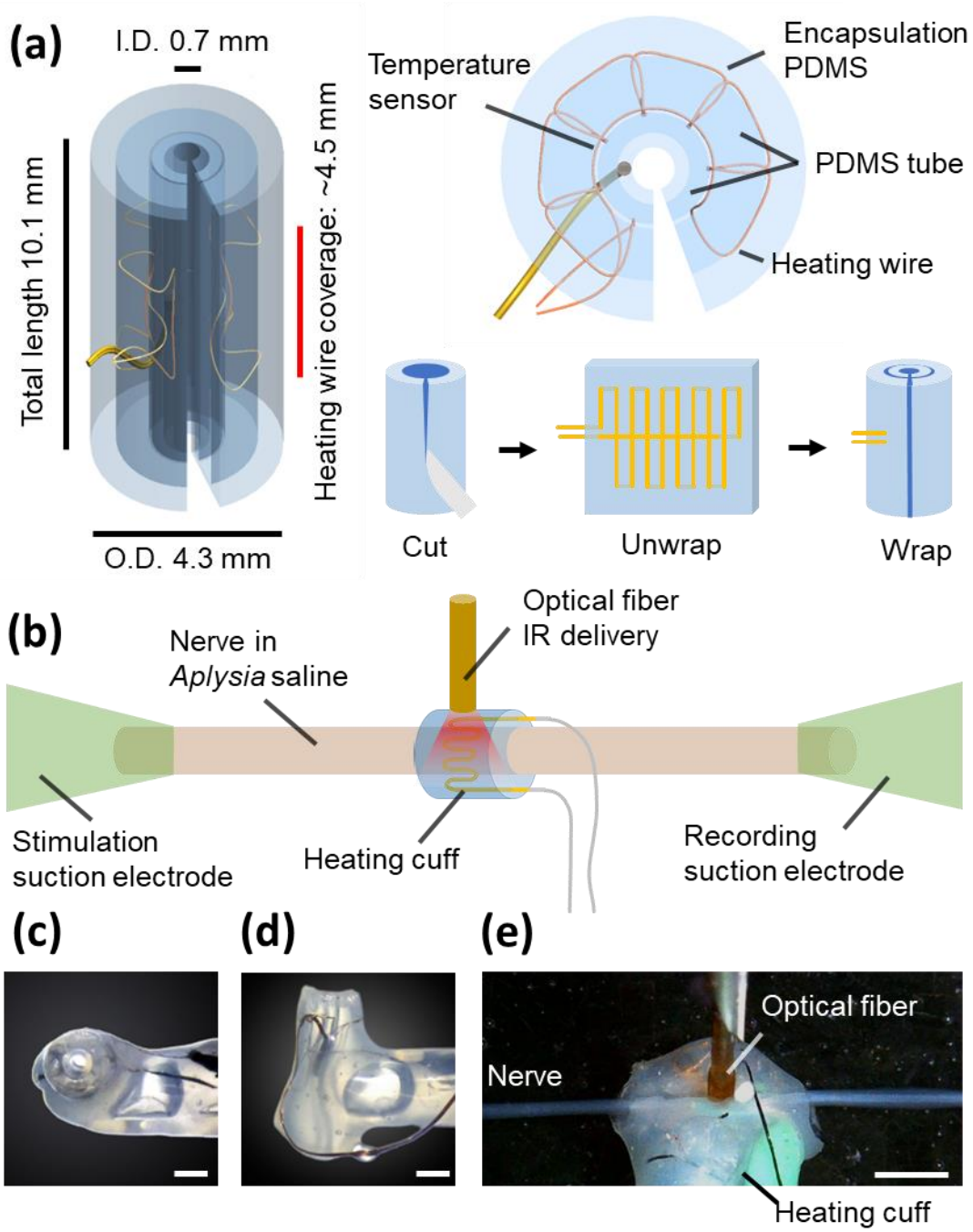

Figure 4.1. The schematic and image of the heating cuff design and the experimental setup.

Panel (a) shows the side view (left) and top view (top right) of the heating cuff along with the main fabrication steps (bottom right; see supplemental material for detailed steps). Note that the slit opening angle for nerve positioning and optical fiber insertion in the schematic is enlarged for the purpose of illustration. Panel (b) shows the schematic of the experimental setup where the nerve was stimulated and recorded by suction electrodes while the optical fiber for IR light delivery and

the heating cuff were collocated on the same segment of the nerve. Panels (c and d) show the top- and side-view of the constructed heating cuff (scale bar: 2 mm). Panel I shows a zoomed-in view of the experimental setup. A heating cuff was wrapped around an Aplysia's pleural-abdominal connective, with an optical fiber inserted into the slit for infrared light delivery. Suction electrodes are not shown in the image as they are further away, located at the nerve ends. Scale bars in panel c to d: 2 mm. I.D.: inner diameter. O.D.: outer diameter.

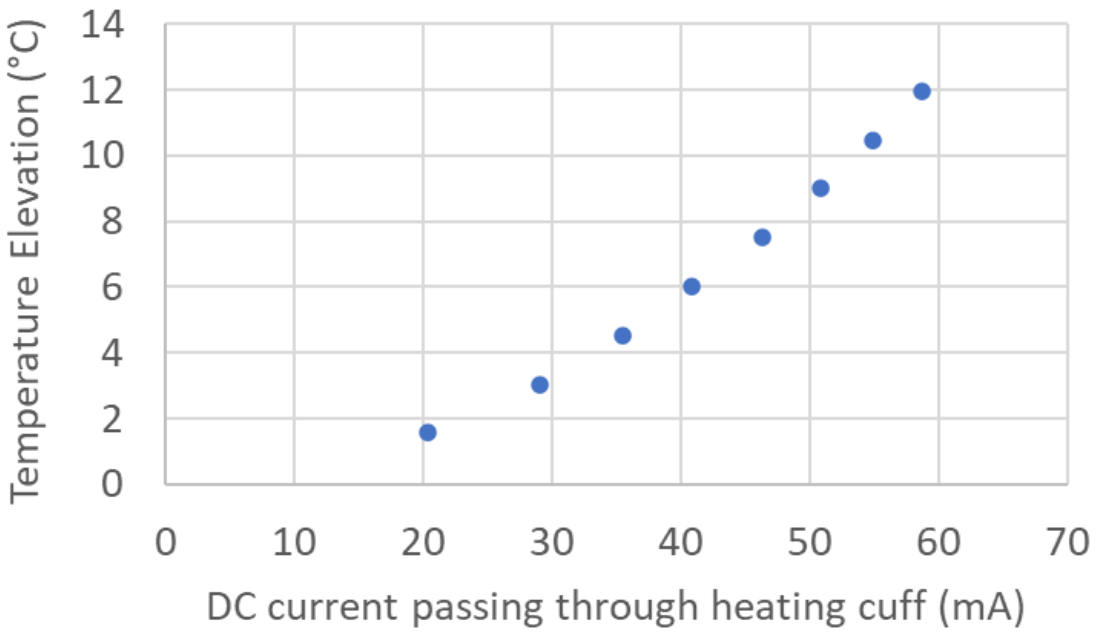

Figure 4.2. The direct current level vs. temperature elevation for the heating cuff.

Because $Power = I^2 \cdot R$ *and* $\Delta T \propto Power$*, we have* $\Delta T \propto I^2$*. The resistance of the heating wire can be considered as unchanged as the nichrome heating wire has a very low temperature coefficient of resistivity (0.017% resistivity change per °C).*

Infrared neural inhibition (INI)

IR light was generated with a single-mode laser diode (QFBGLD-1470-250, QPhotonics, MI, USA, λ = 1470 nm) and a controller (6340-4A, Arroyo Instruments, CA, USA). The optical power was controlled by setting the current. A DAQ device (USB-6218, National Instruments, TX, USA) triggered 60-second laser pulse trains (1250 Hz, 400 µs pulse width). The relationship between the IR laser diode current and IR optical power at the fiber tip was determined using a power meter (PS19Q, Coherent, CA, USA). The laser

diode temperature was held constant at 20 °C for stable and repeatable optical power output. IR light was delivered to the targeted nerve region via an optical fiber (P600-VIS-NIR, Ocean Insight FL, USA, 600-μm core, NA = 0.39). While 600 μm is the illuminated area, the heated region will be slightly larger than that as previous studies have demonstrated [191,192]. As shown in Figure 4.1 (e), the optical fiber was inserted into the slit of the heating cuff to directly touch the nerve and fix its location relative to the nerve through the experiments.

Temperature elevation (Δ T) measurement

RH and INI were applied to the same nerve segments to minimize variability. The heating cuff, optical fiber tip, and nerve were fully immersed in saline to provide a stable thermal environment. The temperature at the nerve surface was recorded using the thermocouple embedded in the heating cuff, see Figure 4.1 (a). The temp signal was converted by a thermocouple-to-analog converter (SMCJ-T, Omega Engineering, CT, USA) to an analog voltage signal (0-100 mV for 0-100 °C), which then was digitized and recorded using the same DAQ device for the CAP acquisition. And then Δ T was calculated by subtracting the baseline temperature from the temperature during heating, see Figure 4.3. As the temperature and CAP were recorded simultaneously, we calculated ΔT for each CAP using the temperature recorded when the CAP was evoked. For all six nerves, the baseline temperature was similar (20.2 ± 0.3 °C). Because the fluctuations in baseline temperature are negligible compared to the temperature rise induced by the heating trials, and also to make the subsequent discussion about CAP response versus temperature more intuitive, we chose to use show Δ T in the subsequent analysis.

Experimental protocol

The experiments were performed in six excised pleural-abdominal connectives from *Aplysia* to test the effects of INI and RH on neural conduction. Each nerve was tested with INI and RH sequentially. We randomized the sequence of INI and RH tests to minimize the accumulative effect due to the previous heating modality. Of all six nerves, three were first tested with INI, and the rest were first tested with RH. Both heating modalities were evaluated with a series of 150-second heating trials with increasing power applied at the neural interface until predefined endpoints were met (a partial inhibition was evident, or the maximum $\Delta T \geqslant 15\ ^{\circ}C$). The step increase of power applied was set so that the maximum ΔT during a given heating trial was approximately 2 °C higher than the previous one. The empirical maximum ΔT limit at 15 °C was determined based on our previous experience with repeated heating tests. To be more specific, from our experience in previous studies and the preliminary tests, when the maximum temperature elevation is greater than 15 °C, there is a high likelihood of inducing an irreversible inhibitory effect, which may be due to thermally induced irreversible tissue damage that prohibited any further testing on the same nerve. Therefore, it was necessary to limit the maximum temperature elevation to 15 °C, which permits us to maintain the nerve's health after completing the test of the first heating modality. On the other hand, this maximum temperature elevation limit prevented us from conducting the temperature threshold analysis for the large-diameter axons, as they remain uninhibited most of the time in this temperature range. Since we are focusing on the selective inhibitory effect, we considered this limitation acceptable.

Each 150-second heating trial consisted of a 10-second control period (no heating), a 60-second heating period, and an 80-second cooling period, as shown in Figure 4.3 (a). Electrical stimulation was applied throughout the heating trials to monitor the neural

conduction status, as shown in Figure 4.3 (b). The inhibitory effect was assessed by comparing the CAPs during the initial 10-second control period and the 60-second heating period. The acute health conditions of the nerves after heating were assessed by comparing the CAPs at the end of the initial 10-second control period and at the end of the 80-second cooling period.

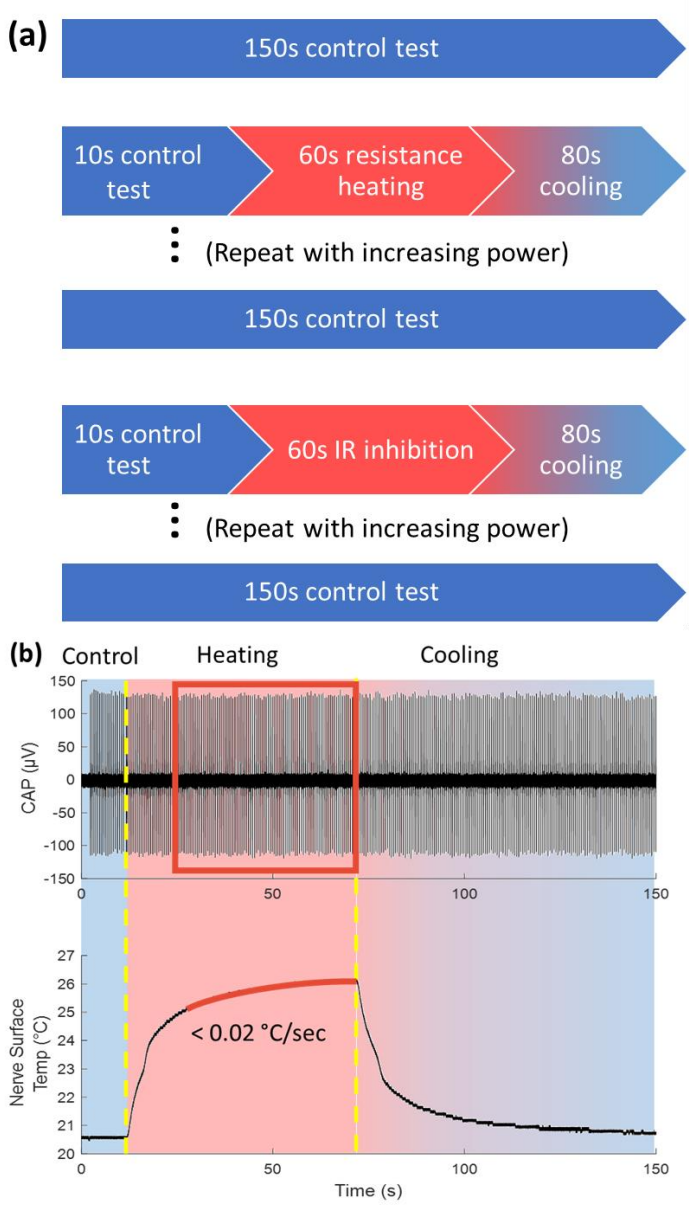

Figure 4.3. The heating test protocol and a representative CAP recording with ΔT change during the 150-second heating trial.

(a) Two heating modalities were tested sequentially on the same nerve. Each heating modality was tested with gradually increasing power applied at the neural interface until predefined endpoints were met (a partial inhibition was evident or the maximum ΔT ≥ 15 °C). (b) A representative compound action potential (CAP) recording and ΔT change. The yellow dashed lines indicate the time point between different phases of the heating trial. The red box and curve indicate where the temperature was considered quasi-stable (changing rate < 0.02 °C/sec) and used for extracting CAPs and ΔTs for data analysis.

To identify any potential methodological bias between the two heating modalities, it is necessary to compare the total thermal dose applied to the nerve by each heating modality. However, calculating the commonly used cumulative temperature elevation dose (CEM_{43}) using absolute temperature [251,252] is not applicable since *Aplysia* is a heterothermic animal. As *Aplysia's* natural habitat is intertidal pools, its body temperature can be changed by the environment [253] rather than maintaining a constant body temperature as is done by mammals. Therefore, we calculated the thermal dose for each heating modality as follows for a first approximation:

$$Thermal\ dose = \sum \Delta\mathrm{T} \cdot \text{duration of each } \Delta\mathrm{T}$$

Data analysis

CAP recording pre-processing

To prepare the CAP data for analysis, several pre-processing steps were applied (see details in the supplemental materials):

We removed the DC components from the recorded CAPs by a high-pass filter at a 1 Hz cut-off frequency to avoid any drift due to electrodes or circuitry. We collected a background noise sample by recording a short period from the CAP channel during which no electrical stimulation was applied. The background noise sample and its properties were then used to subtract the noise from subsequent analyses.

For the analysis, we selected only the CAPs during the quasi-steady temperature period during which the temperature change rate was smaller than 0.02 °C/s. As shown in Figure 4.3, when heating was applied, the temperature increased rapidly during the initial 15 s and then stabilized. Preliminary experiments indicated that the profiles of the tissue heating ramps were different between the two heating modalities (INI vs. resistive, yielding internal absorption of light vs. heating from the surface), and the inhibition effect was therefore different during this ramp period. In comparison with INI, resistive heating inherently produces a slower change of temperature in the nerve because heat needs to be conducted from the surface inward. The temperature elevation is independent of the heating method only after it reaches a steady state. Therefore, we limited the comparison of the inhibition effect (i.e., CAP analysis) to the period in which temperature was near a steady state. Therefore, we have empirically defined the quasi-steady temperature period for CAP extraction as corresponding to a temperature change rate < 0.02 °C/s (as shown by the red curve in Figure 4.3).

Because axonal subpopulations with different diameters have different conduction velocities (i.e., larger diameters correspond to faster conduction velocities), we then segmented the CAPs into fast- and slow-conducting subcomponents which correspond to large- and small-diameter axons, as we did in the previous studies[8,191,192]. Please see the details in session 3.2.2. The boundary detection results between the fast- and slow-conducting subcomponents were inspected to ensure that the boundary did not bisect CAP components, and in 97/111 trials, no adjustments were necessary.

Quantification of inhibition effect

To quantify inhibition strength, we separately calculated the rectified area under the curve (RAUC) for the fast- and slow-conducting subpopulations in the CAP, as shown in Figure 4.4. The RAUC during the heating period was normalized to the average RAUC during the

last three seconds of the control period. The normalized inhibition strength (NIS) can then be calculated as the reduction in the normalized RAUC:

$$Normalized\ inhibition\ strength = 1 - Normalized\ RAUC.$$

The NIS value will increase from 0 up to 100% if an inhibitory effect is present. A NIS below 0 indicates an excitatory effect. It can be compared across different subpopulations and nerves as it does not depend on the absolute value of the RAUC.

We calculated the inhibition probability for each axonal subpopulation as the number of inhibition events divided by the total number of CAPs. A CAP was considered an inhibition event when the NIS for the given subpopulation was greater than 50%. To quantify the change in the inhibition probability as ΔT increased, the NIS data from all nerves were pooled and grouped into non-overlapping 1 °C ranges (e.g., [0 1) °C and [1 2)°C) based on their corresponding ΔT. The inhibition probability was calculated for each 1 °C range using the NIS data within that range.

To estimate and compare ΔT thresholds of inhibition between INI and RH, probit regression was applied to the inhibition probability data. Probit regression is suitable for assessing responses from experiments with binominal results. Previous studies on laser-tissue interactions have applied probit regression to characterize the response during laser ablation [254] and INS [169,188,255]. For the probit regression, we fit a normal cumulative distribution function (CDF) to the inhibition probability in response to an increase in ΔT. The probit regression function is:

$$Fitted\ inhibition\ probability(p) = \frac{1}{2}\left[1 + erf\left(\frac{\Delta T - T_{50}}{\delta \cdot \sqrt{2}}\right)\right],$$

where ΔT is the independent variable. The fitting process results in an estimate of the ΔT_{50} for inhibition, which is the ΔT threshold for a 50% probability of inhibition. It also estimates

δ, which is the standard deviation of ΔT. Probit regression was conducted separately for the fast- and slow-conducting subpopulation during the INI and RH tests, respectively. The ΔT_{50} parameters of the fitted models were compared to determine the ΔT threshold difference between the two heating methods.

To characterize the selectivity of inhibition in the slow-conducting subpopulation, we constructed the parameter inhibition selectivity index as follows:

$$Inhibition\ selectivity\ index = \frac{NIS\ of\ slow}{NIS\ of\ slow + NIS\ of\ fast},$$

where "NIS of slow" means the normalized inhibition strength of the slow-conducting subpopulation and "NIS of fast" means the normalized inhibition strength of the fast-conducting subpopulation. The inhibition selectivity index was only calculated for CAPs with an inhibition event (as previously defined), across the whole temperature range.

The inhibition selectivity index can be interpreted as the contribution of inhibition of the small-diameter axons to the overall inhibitory effect. When the NIS for both subpopulations is equal, the inhibition selectivity index will be 0.5. Any inhibition selectivity index higher than 0.5 indicates a selective inhibition of the slow-conducting subpopulation. Conversely, an inhibition selectivity index lower than 0.5 indicates a selective inhibition of the fast-conducting subpopulation. A paired t-test of the inhibition selectivity index was conducted to compare whether size-selectivity was statistically different between the two heating modalities.

Characterization of the power efficiency of the heating process

While it is important to explore the electrophysiological response for both heating modalities, the efficiency of the heating process is also important for the potential implantable design with those heating modalities. Here, we characterized the efficiency of

the power applied at the neural interface and the efficiency of total electrical power separately, to have a comprehensive understanding of the heating process.

The efficiency of the power applied at the neural interface can be evaluated as the final ΔT (the average ΔT during the last three seconds of each heating trial) when a given power was applied at the neural interface. This parameter indicates how effective the modality is for coupling power into the tissue for generating ΔT. For INI, the power applied at the neural interface is the optical power of IR light emitted from the optical fiber tip. For resistive heating, the power applied at the neural interface is the electrical power delivered to the heating wire. As we have two distinct heating processes here (volumetric energy deposition by INI and surface heat conduction by RH), it is necessary to evaluate the difference in the efficiency of the power applied at the neural interface between the two heating modalities. To compare the efficiency of power applied at the neural interface between the two heating modalities, we calculated the final ΔT as the average ΔT during the last three seconds of the heating period, when a given power was applied at the neural interface.

The efficiency of total electrical power can be calculated as the total electrical power (the electrical power consumed from the wall outlet) required for achieving a target final ΔT. Higher efficiency of total electrical power will permit a longer running time for a battery-powered implantable design. If the implant design is externally powered, a smaller electrical power requirement can also lower the difficulty of wireless power delivery. For INI, the total electrical power is calculated as the electrical power consumed by the laser diode. For resistive heating, the total electrical power is calculated as the power consumed by the entire heating circuit, including the cable connecting the heating wire to the temperature controller. The electrical power consumed by the controlling device (e.g., the temperature controller or laser diode driver) was not included in this study because it

involved irrelevant power consumption such as the power for the display. In addition to heating efficacy and overall energy efficiency, it is also important to examine the repeatability of the heating response across different nerves.

Simulation of the temperature elevation

Since it is difficult to measure the temperature distribution inside nerves with existing techniques, numerical simulations are often used to explore thermal effects under infrared laser irradiation [250,256,257]. We simulated the temperature elevation induced by INI and resistive heating using COMSOL Multiphysics® (COMSOL) software and a mesh-based Monte Carlo simulation in the MATLAB® environment (MMClab) [80,83,84] for light scattering and absorption. For INI and resistive heating, 3D models representing the experimental setup (e.g., the nerve and heating element) were recreated in Solidworks with the same dimensions as in the real world. The nerve's diameter was approximated as 600 μm based on our measurement (614 ± 70 μm). A saline object (10 mm × 5 mm × 10 mm) was created as the background object to bisect and surround all the other objects. The 3D objects representing each type of material were then imported into COMSOL for generating the corresponding tetrahedral mesh. The mesh density and quality were controlled to satisfy the requirement of heat transfer simulation and MMClab.

There are some common settings in the simulation for both INI and resistive heating. Most of the physical properties were assigned to each object domain using built-in materials in COMSOL: The saline domain was modeled using the water (liquid) material. The PDMS cuff was modeled using silicone material. The heating wire was modeled using the nichrome (solid, steady-state) material. The optical fiber was modeled using silica glass material. Some objects (e.g., nerve and heating wire) required the use of externally referenced physical properties, as shown in Table 4.1. The nerve's thermal property was approximated based on the nerve's water content as described in previous literature [256,258].

Laminar flow caused by the density change during heating was simulated in the *laminar flow* module for both INI and RH. Gravity was included in the *laminar flow* module as the negative direction along the z-axis. Heat dissipation caused by laminar flow was simulated using COMSOL's multiphysics module: *nonisothermal flow.* The top surface of the saline was defined as the interface between ambient air and saline, where heat loss due to radiation was included in the simulation. All other outer surfaces of the saline were defined as symmetric boundaries where heat transfer and flow rate were both negligible. All objects and the ambient air were set to have an initial temperature of 22 °C. The reference air pressure was 1 atm and the top surface of the saline object was defined as an open boundary with no stress in the laminar flow module. The model was simulated with a time-dependent solver for 0 to 60 s (the same heating period as in the heating protocol), with a 0.1 s output interval and physics-limited dynamic time steps. To validate the models, we simulated the temperature elevation distribution at the thermocouple location with several power levels applied at the neural interface. The simulated temperature elevation was then compared with the experimental result to validate the model. After validation, we simulated the required power to be applied at the neural interface for achieving the 50% probability of inhibition in the slow-conducting subpopulation, by each heating modality separately.

Table 4.1. Externally referenced physical material properties

Object	Property	Value	Unit
Heating Wire *	Thermal conductivity	15	W/(m·K)
	Heat capacity at constant pressure	465	J/(kg·K)

	Relative permittivity	800	a.u.
Nerve [256,258]	Thermal conductivity	0.49	W/(m·K)
	Heat capacity at constant pressure	3581	J/(kg·K)
	Density	1106	kg/m^3

** Directly from the supplier: A-M Systems, WA, USA*

For resistive heating, we simulated *the heat transfer in solids and fluids* (in nerve, saline, PDMS, and heating wire), *laminar flow* (in saline), and *electric currents* (in heating wire) using existing COMSOL modules by those names. The heat source for the heater transfer was from the multiphysics module: *electromagnetic heating*. The power levels simulated for heating response validation were from 25 mW to 150 mW with a 25 mW step. A simulation of 103.1 mW power applied at the neural interface by resistive heating was performed to evaluate the temperature elevation across the nerve when a 50% probability of inhibition of the slow-conducting subpopulation was achieved experimentally.

For INI, we simulated *the heat transfer in solids and fluids* (in nerve, saline, and PDMS) and *laminar flow* (in saline), using existing COMSOL modules by those names. The heat source for the heat transfer module was generated using MMClab. We used LiveLink™ for MATLAB® to import the generated tetrahedral mesh from COMSOL as the mesh data for MMClab. Using the same mesh as the COMSOL model can help reduce the computational load when the MMClab result was imported back into COMSOL and mapped to the mesh nodes. In MMClab, optical properties for each type of material (nerve, saline, PDMS, and optical fiber) were assigned to the corresponding mesh element, as shown in Table 4.2. The nerve's optical properties were approximated using the average values from other species [256,258,259] as there is no measurement available for a nerve in

Aplysia. The optical property of *Aplysia* saline was approximated by the values for water. A cone-shaped light source was used to mimic the light output profile from the optical fiber tip in an aqueous medium. Since the simulation's goal was to estimate the temperature distribution at the end of the heating period, the temporal fluctuations of temperature caused by each laser pulse were not investigated. Instead, we simulated the energy deposition of the laser pulse train using a continuous (CW) laser source with equivalent average optical power as the pulsed laser. The MMClab generated the normalized impulse response as energy deposition at each mesh node over time. We then converted it to the step response for a unitary CW source by convolution, which means integrating over time and multiplying by the time step in the discrete domain. This energy deposition caused by the unitary CW source was then imported back into COMSOL. We then scaled the unitary response by the optical power to be simulated and used it as the heat source for the *heat transfer in solids and fluids* module. The power levels simulated for heating response validation were from 15 mW to 75 mW with a 15 mW step. A simulation of 52.4 mW power applied at the neural interface by INI was performed to evaluate the temperature elevation across the nerve when a 50% probability of inhibition of the slow-conducting subpopulation was achieved experimentally.

Table 4.2. Optical parameters of the materials

Material	μ_a (1/cm)	μ_s (1/cm)	Anisotropy (a.u.)	Refractive Index (a.u.)
Saline [69,260]	30.0	0	N/A	1.36
Nerve [256,258,259]	24.0	2.0	0.9	1.36
PDMS [261]	1.4	0.1	1	1.43

Optical Fiber Core	0**	0**	N/A	1.47
Optical Fiber Cladding	0**	0**	N/A	1.42

** Directly from the supplier: Ocean Insight FL, USA*

*** Approximated to be zero to simplify the calculation*

To validate the simulation models, we simulated the temperature elevation at the thermocouple location as different powers were applied at the neural interface by each heating modality. The simulated results shown in Figure 4.7 (a) (INI - with the semitransparent yellow line; resistive heating – blue line) were similar to experimental measurements. This suggests that the models were a good approximation to the real-world experimental setup.

We simulated the two heating modalities by applying the power at the neural interface (INI: 39.8 mW, RH: 80.7 mW) required to reach their respective T_{50} temperatures. The simulated average temperature elevation of the axon-containing region in the nerve was similar: 7.45 °C for INI and 7.53 °C for resistive heating, see Figure 4.7 (a to d). To evaluate the impact of the uncertainty on the estimated physical parameters of the nerve, a parametric sweep was conducted; the maximum changes of simulated average temperature elevations for the axon-containing region were 0.57 °C for INI and 0.04 °C for RH. Since the heating process under the current heating protocols is dominated by heat diffusion, the changes due to the uncertainty of estimated physical parameters are evened out over space and do not cause a significant change in the simulated temperature elevation. In addition, the simulation allowed us to deduce the ΔT at the axon-containing region of the nerve using the thermocouple measured ΔT at the surface of the nerve,

which allowed us to estimate the relationship between the inhibition probability and the simulated axonal region temperature.

4.2.3 Results

Nerve's thermal exposure was similar between INI and RH

To compare the changes in the electrophysiological responses induced by the two heating modalities, it is necessary to examine if there is a systematic bias in the available data and thermal exposure between the two heating modalities. On average, we conducted 8 ± 2 trials for RH and 7 ± 1 trials for INI on each nerve and the average interval between heating trials was 3 minutes. From the quasi-steady period during heating, we collected 1927 CAPs during INI and 2260 CAPs during RH. The number of valid CAPs in each nerve between the two heating modalities did not show a significant difference ($p = 0.70$, paired t-test). The normalized RAUC after heating is on average 94.4% $\pm$ 5.9% of the RAUC before heating. The ΔT step from one heating trial to the next was 1.4 ± 0.9 °C for INI and 1.3 ± 0.8 °C for RH with no significant difference ($p = 0.55$, paired t-test). The total thermal dose of each heating modality was calculated for the six nerves. We applied an average thermal dose of 2405 °C· s during INI and 2945 °C· s during RH on each tested nerve, with no significant difference between the two heating modalities ($p = 0.17$ paired t-test). Overall, the data and thermal exposure of the nerves were similar for both INI and RH, allowing an unbiased comparison of the inhibitory effect between the two modalities.

Resistive heating can induce a selective inhibition effect similar to infrared neural inhibition

The representative data in Figure 4.4 shows that RH produced a selective inhibition effect, similar to INI. The ΔT for this representative data (INI: 9.5 °C, RH: 10.6 °C) was high enough to induce a block on the slow-conducting subpopulations (Figure 4.4, panel a, red),

while still too low to significantly inhibit the fast-conducting subpopulations (Figure 4.4, panel a, blue). Raw normalized RAUC data (Figure 4.4, panel b) confirmed that both heating modalities could induce a similar drop in the signal for the slow-conducting subpopulation. The control test conducted after the heating test (Figure 4.4, panel a, $Ctrl_2$) showed a response similar to that of the initial control test (Figure 4.4, panel a, $Ctrl_1$), suggesting that the health of the nerve was not acutely impacted. This can be also confirmed by the normalized RAUC after cooling for each trial conducted on the same nerve, as shown in Figure 4.4 (c).

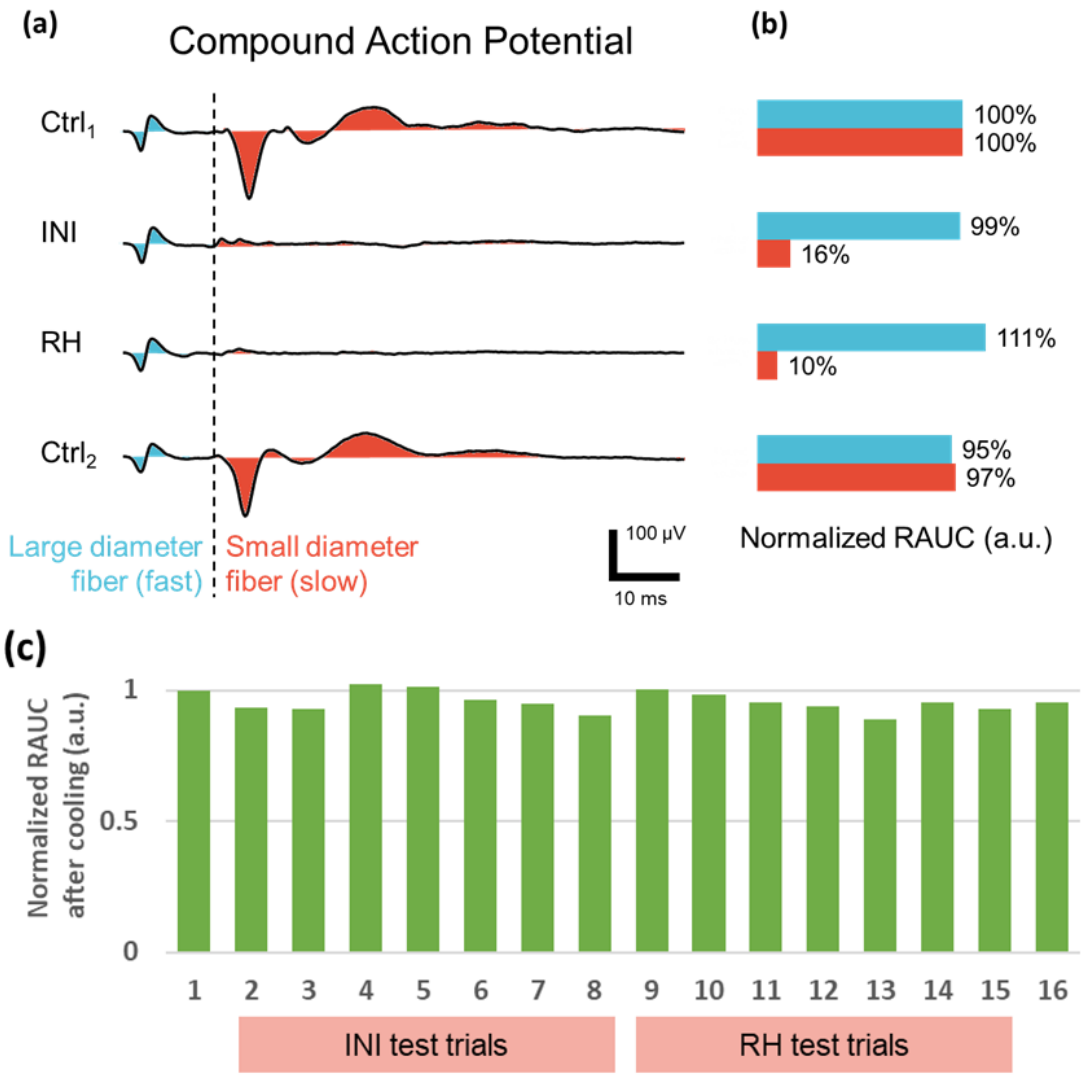

Figure 4.4. Representative compound action potential (CAP), the corresponding normalized RAUC, and the normalized RAUC after cooling for all trials conducted on a nerve.

(a) Representative compound action potentials show the selective INI on small-diameter axons can be reproduced by resistive heating (RH) via a heating cuff. Blue: the large diameter subpopulation with fast conducting velocity. Red: the small diameter subpopulation with slow conduction velocity. A dashed line indicates the segmentation point between the fast- and slow-conducting subpopulations. From top to bottom, $Ctrl_1$: the control test before heating application; INI: infrared neural inhibition application showed selective inhibition of the slow conducting subpopulation; RH: the heating cuff was able to induce a similar selective inhibition effect of the same CAP subpopulation; $Ctrl_2$: the control test after all heating tests after the temperature has returned to baseline. The response in $Ctrl_2$ was similar to $Ctrl_1$, suggesting that selective inhibition was reversible. The baseline temperature during the tests was 20.3 °C. The ΔT was 9.3 °C for the INI

trial and 10.2 °C for the RH trial. The conduction velocity for the fast and slow conducting groups in this nerve was 0.956 m/s and 0.239 m/s, respectively (estimated using the peak of each group). (b) The normalized RAUC for each trial in (a), was calculated for the fast (blue) and slow (red) subpopulation separately. IR application and RH were able to induce a similar level of RAUC reduction. When the heating was turned off, the RAUC recovered to the control test's level. (c) The normalized RAUC after cooling for each trial that was conducted on the same nerve. The red bars indicate trials for the INI test and RH test, respectively. A.U.: arbitrary units.

To further examine the selective inhibition effect on all tested nerves, we calculated the normalized inhibition strength (NIS) for the fast- and slow-conducting subpopulations of CAPs recorded during the quasi-steady state of the heating period (see Methods). For each 1 °C temperature range, the NIS data from each nerve were averaged to represent the response of a given nerve. The response of all six nerves is shown in Figure 4.5 (a) and (b). When comparing across different subpopulations, the NIS of the slow-conducting subpopulations was generally higher than the corresponding values for fast-conducting subpopulations from the same CAP. RH showed an overall trend similar to that of INI, but with a wider separation between the fast- and slow-conducting components.

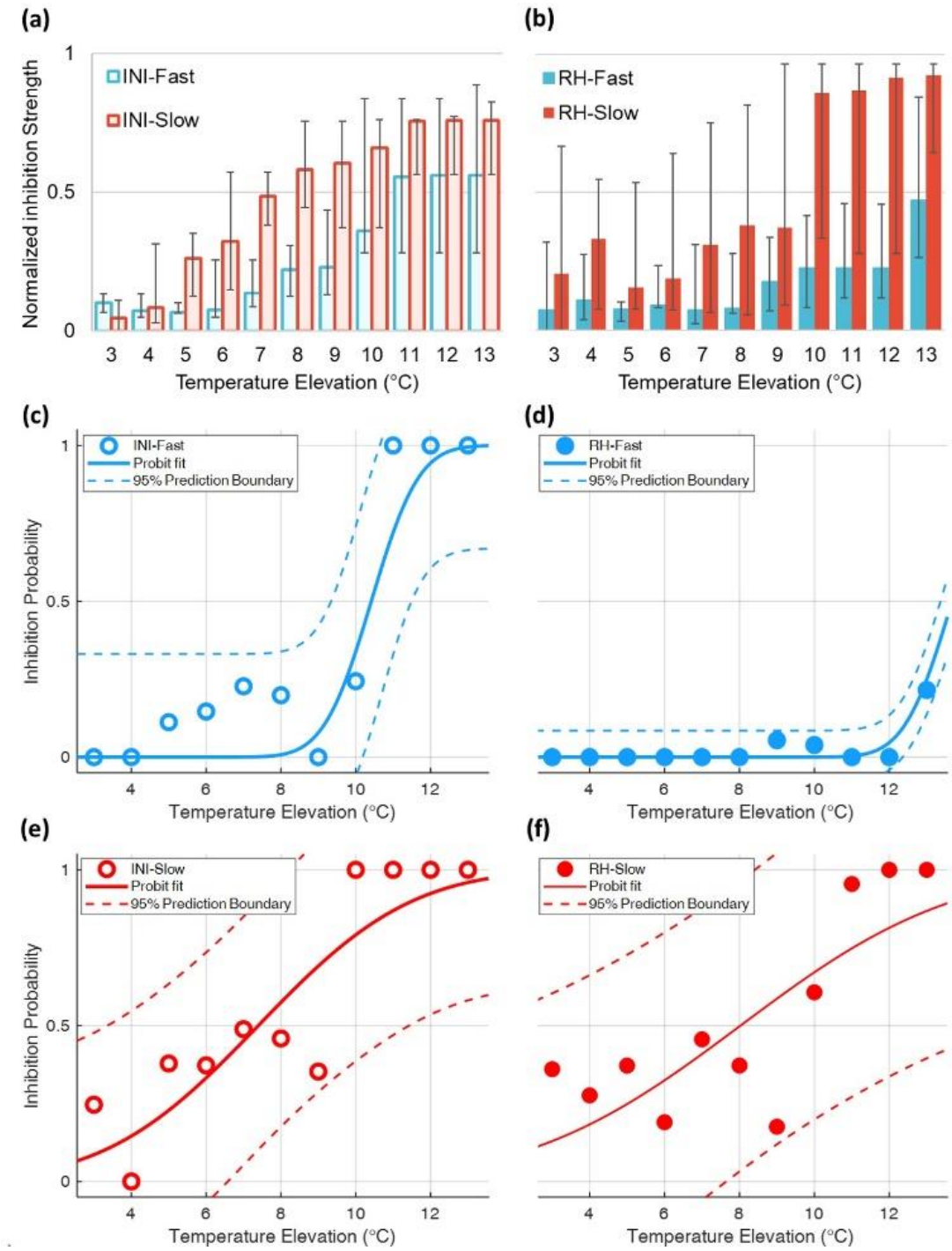

Figure 4.5. The normalized inhibition strength (NIS) and inhibition probability for fast- and slow-conducting subpopulations under infrared neural inhibition (INI) and resistive heating (RH).

The top row (panels a and b) shows the median (bars) and lower/upper quartiles (whiskers) of the NIS data from all six nerves. The NIS data increased as the temperature elevation increased and

the slow-conducting components showed a higher level of inhibition compared to the fast-conducting components (red bar vs. blue bars, respectively). The y-axis ticks are the same for panels a and b. The bottom row (panels c to f) shows that, for all groups, the inhibition probability increased as the temperature elevation increased. The y-axis ticks are the same for each horizontal row. The fitted line shows the probit regression result for each subpopulation, and the dashed lines show the 95% confidence interval. The threshold temperature elevation for 50% inhibition probability on the slow-conducting components was 7.40 °C for INI and 8.03 °C for resistive heating, noting the baseline temperature was 20.2 ± 0.3 °C for the six nerves. Although not all nerves showed full inhibition, the probit regression was applied to the fast-conducting subpopulation to compare it to the slow-conducting subpopulation. Blue circles: fast-conducting subpopulation. Red circles: slow-conducting subpopulation. Unfilled marker: INI. Filled marker: RH.

When we calculated and compared the inhibition probability (probability of inducing a NIS of > 50%) for each 1° C range using pooled data from all six nerves, the similarity of the trends was more obvious (see Figure 4.5, c to f). The inhibition probabilities were calculated using all NIS data rather than only the averaged data shown in Figure 4.5 (a and b). As ΔT increased, the inhibition probability for both heating modalities increased more rapidly for the slow-conducting subpopulation. To compare the inhibition probabilities of fast- and slow-conduction subpopulations across the whole ΔT range, we conducted a one-tailed paired t-test and confirmed that the inhibition probability in the slow-conducting subpopulation was higher ($p < 0.01$ for both INI and RH). This indicates that the inhibition probability was significantly higher for the slow-conducting subpopulations than for the fast subpopulations in response to the same temperature with both heating modalities. Probit regression was applied to the inhibition probabilities of both fast- and slow-conducting components for each heating modality. The fitted lines (probit regression) are shown in Figure 4.5, (c to f). Table 4.3 lists the optimal probit regression fitting parameters with the 95% confidence interval range indicated in brackets.

Table 4.3. Optimal fits for the probit regression of inhibition probabilities for each subpopulation

Heating Modality	Sub-population	ΔT_{50}	δ	Root mean squared error
IR Neural Inhibition	Fast	10.42 [9.79, 11.04]	0.35 [0.35, 0.35]	0.150
	Slow	7.40 [6.15, 8.64]	1.14 [0.49, 1.78]	0.165
Resistive Heating	Fast	13.68 [13.45, 13.91]	0.35 [0.35, 0.35]	0.0386
	Slow	8.03 [6.23,9.83]	1.58 [0.51, 2.64]	0.081

Comparing the fitted parameters, we can see that the ΔT threshold for inhibiting the slow-conducting subpopulation with RH (8.03 °C) was slightly higher than the threshold with INI (7.40 °C). The ΔT_{50} for fast-conducting components is higher than the ones for the slow-conducting components under both conditions, confirming the size-selective inhibition effect on the small-diameter slow-conducting components. Although the probit regression was performed for the fast-conducting subpopulation, the study was not designed to induce a full block of the fast-conducting subpopulation, since this might subject the nerves to excess thermal stimulation when the same nerve is tested under both conditions. In the six nerves tested, full inhibition was only observed in three nerves during the INI test and in the other three nerves during the RH test. Only one nerve showed a full inhibition response during the test of both heating modalities. The limited raw data

for the inhibition probability of fast-conducting components caused the optimal estimate of δ to be limited at the theoretical boundary of 0.35.

We compared the inhibition selectivity index when an inhibition event was present for either or both subpopulations. The calculation was conducted for each nerve separately, across the whole tested temperature range. As shown in Figure 4.6, RH had a higher average inhibition selectivity index (0.86) than INI (0.76), although the difference was not significant according to a paired t-test ($p = 0.37$). The average inhibition selectivity indexes for both methods were higher than 0.5 demonstrating that RH reproduced the size-selective inhibitory effect of INI. From Figure 4.6, we also see that the variance in the inhibition selectivity index for each nerve was smaller for RH in general. This suggests that RH can induce selective inhibition more reliably when the nerve's geometry and fascicle orientation vary from one nerve to another.

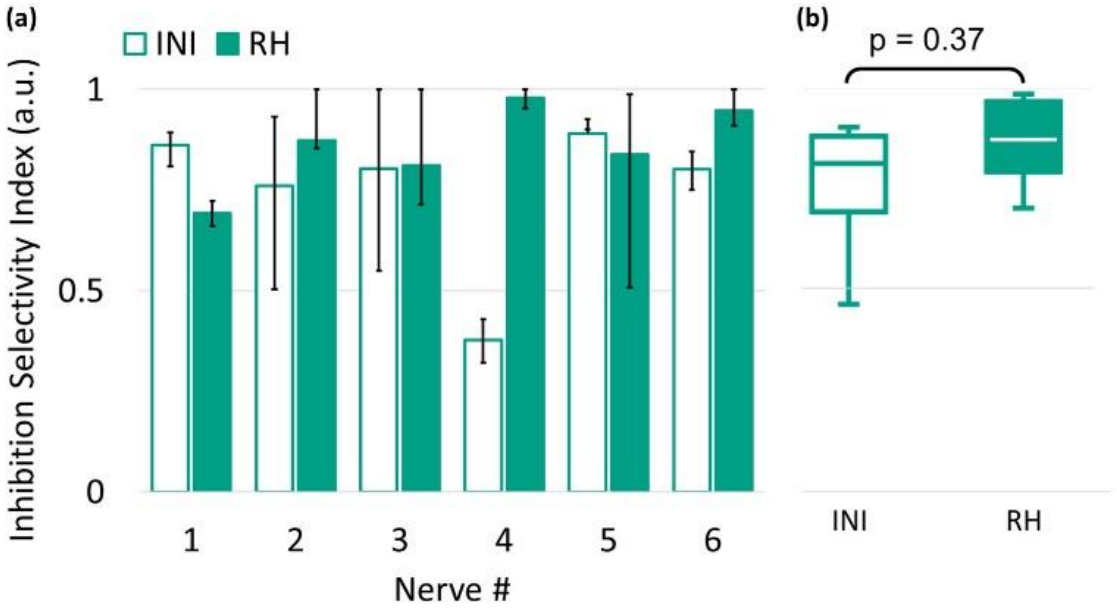

Figure 4.6. The inhibition selectivity index on the slow-conducting subpopulation for IR neural inhibition (INI) and resistive heating (RH).

(a): The inhibition selectivity index (see Methods) for each nerve with each heating modality. The index was calculated for all inhibition events (a normalized inhibition strength larger than 50% for

either fast- or slow-conducting subpopulation), regardless of the temperature. An inhibition selectivity index closer to 1 indicates a more selective inhibition of the slow-conducting small-diameter axons. The error bars indicate the upper and lower quartiles. (b): Box plot of the average inhibition selectivity index for INI (0.76) and RH (0.86). The difference was not significant according to a paired t-test (p = 0.37). A.U. arbitrary unit.

In summary, the results show that RH can reproduce INI's selective inhibition effect on a slow-conducting small-diameter subpopulation with a similar temperature threshold.

4.2.4 Discussion

The current study demonstrated that selective inhibition of small-diameter axons induced by INI can be reproduced by another heating modality such as RH (Figure 4.4). RH relies solely on the induced temperature elevation for inducing size-selective inhibition (Figure 4.6). As selective INI has been demonstrated using *Aplysia* and then successfully migrated to vertebrates with substantially lower ΔT thresholds [8], we expect that the selective inhibitory effects of RH will also translate to vertebrates with a future *in vivo* chronic implantable design. RH may also be used in future studies to investigate non-blocking neuromodulation effects (e.g., the change of neurons' excitability and neural plasticity) induced by chronic localized heat application on neurons. Here are some aspects of this potential application that are worth discussing.

Size selectivity as an inherent property of heat-induced neural block

Previous studies have suggested that INI relies on thermally accelerated ion channel kinetics, particularly voltage-gated potassium channels [9,10]. Hence, we tested the hypothesis that a pure heating process could induce the same size-selective inhibition. Unlike INI, RH does not involve optical processes. We used the direct current, which only generated a static electromagnetic field that did not stimulate the nerve. The RH test results showed a similar size-selective inhibition as compared to INI, although with a slightly different ΔT (7.40 °C for INI and 8.03 °C for RH).

This difference in the ΔT_{50} (Table 4.3) and dose-response curve (Figure 4.5) can likely be attributed to the difference in heat conduction direction between the heating modalities. An experimental limitation of our approach was that only the temperature at the nerve surface can be measured, as shown in Figure 4.1 (a), which can be different from the temperature at the core of the nerve where the axons are located. Due to the difference in where the heat was generated (INI: in the nerve, RH: around the nerve), the temperature at the nerve's core can have a different relationship to the measurable temperature at the nerve surface (INI: core temperature higher than surface temperature; RH: core temperature lower than surface temperature). From our previous measurements of the *Aplysia's* pleural-abdominal connective, the average diameter of the region that axons occupy is 242.9 ± 76.8 μm, which is less than half of the nerve's total diameter at 611.7 ± 85.0 μm (n = 48). The gap between the nerve surface and the core region where the axons are located can allow a temperature gradient to exist. Therefore, the difference in the measured ΔT threshold for selective inhibition between the two heating modalities may be attributed to the difference in the heat generation locations rather than a difference in biological processes.

Since it is difficult to measure the temperature distribution inside nerves with existing techniques, numerical simulations are often used to explore thermal effects under infrared laser irradiation [250,256,257]. We simulated the scenario that INI and RH were applied with appropriate power (INI: 39.8 mW, RH: 80.7 mW) to achieve their respective ΔT_{50} (INI: 7.40 °C, RH: 8.03 °C) at the nerve surface. The simulation was conducted on a 3D finite element model (FEM) that duplicates the geometry and physical properties of the RH and INI setup, using COMSOL Multiphysics® (COMSOL) software and a mesh-based Monte Carlo simulation in the MATLAB® environment (MMClab) [80,83,84] for light scattering and absorption (see supplemental materials for details). Using the simulated temperature

distribution, we calculated the average ΔT_{50} at the axonal area of the nerve (as shown in Figure 4.7 (a to d) by the dashed circles, dia. = 0.243 mm). The simulated average ΔT_{50} of the axon-containing region in the nerve was similar: 7.45 °C for INI and 7.53 °C for RH, see Figure 4.7, (a to d). We also used the simulation to estimate the dose-response curve of inhibition probability as ΔT increases at the axon-containing region of the nerve. The thermal dose-response curves based on the ΔT at the core region of the nerve were not significantly different between the two heating modalities ($p = 0.43$, paired t-test), see Figure 4.7 (e). This similarity of the simulated thermal dose-response curves again was consistent with our hypothesis that both heating modalities, INI, and RH, induce neural inhibition by the same thermal effects.

Further research (e.g., parameter optimization functional tests) will be required to translate selective block by RH to vertebrates and explore the feasibility of size-selective inhibition (primarily on the unmyelinated fibers) *in vivo*.

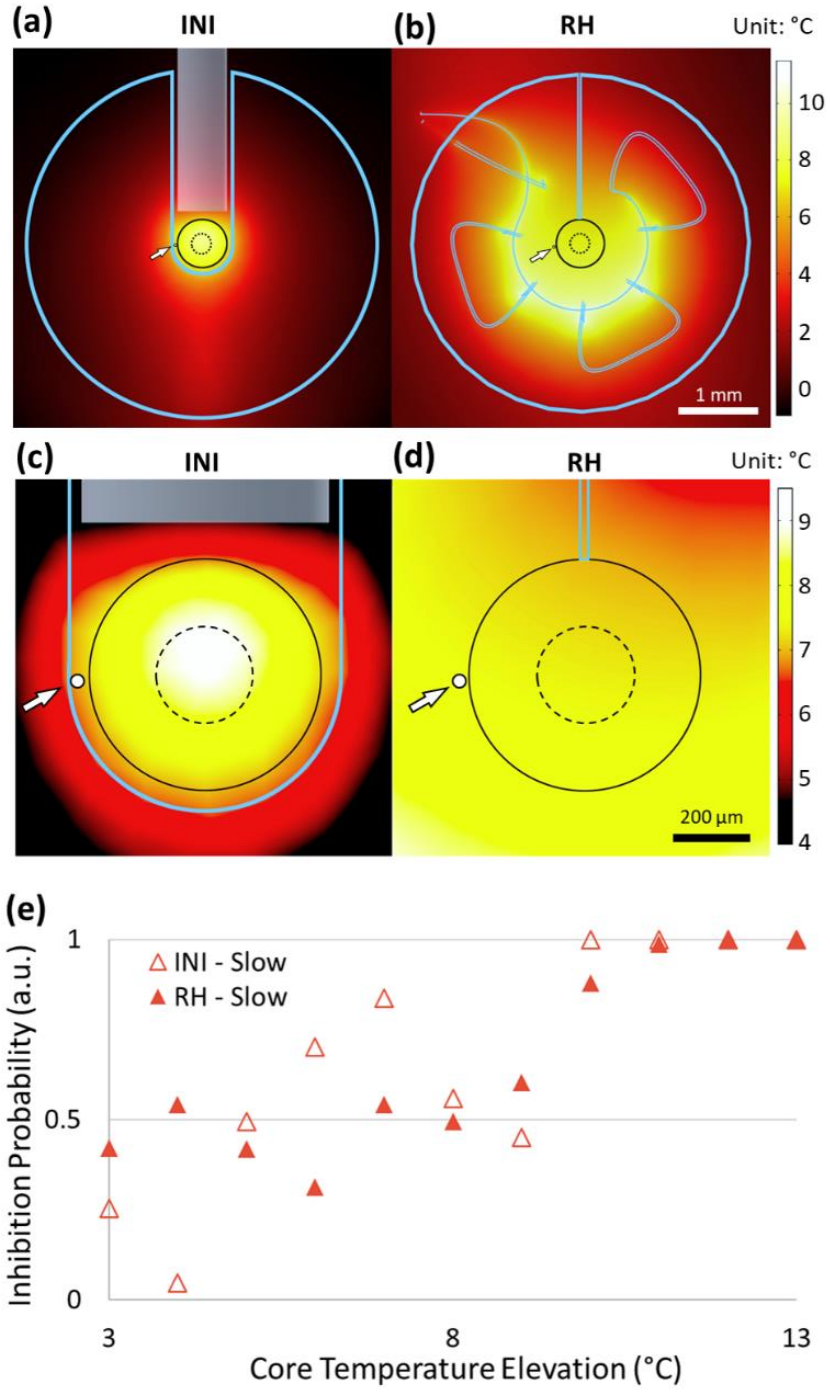

Figure 4.7. The simulated radial temperature elevation distribution over the cross-section of the nerve and the inhibition probability based on the core temperature elevation of the nerve.

INI: infrared neural inhibition, RH: resistive heating. Panel (a) to (d): The radial cross-section view of the simulated temperature distribution for each heating modality. Panel (a) and (b) are the overall

views while panels (c) and (d) are the zoomed-in views of the same simulated temperature distributions (respectively). The geometry in the light blue line indicates the geometry of the nerve cuff, including the heating wire. The solid black circles indicate the location of the nerves. The dashed black circles indicate the axon-containing region. The simulated powers applied at the neural interface correspond to the amount required to induce an inhibition probability of 50% on the slow-conducting subpopulation (INI: 39.8 mW, RH: 80.7 mW). The colormap for panels (c) and (d) was adjusted to show the temperature gradient more clearly. The arrows and dots (white filled with a black border) indicate where the thermocouple was located in the real-world setup. The scale bar is 1 mm for panels (a) and (b), and 200 µm for panels (c) and (d). Panel (e): The inhibition probability of the slow-conducting subpopulation as a function of temperature elevation in the axon-containing region was not statistically different between INI and RH (p = 0.40, paired t-test). Red-filled triangle: slow-conducting subpopulation with RH. Red unfilled triangle: slow-conducting subpopulation with INI. A.U.: Arbitrary unit.

Therefore, based on the experimental and simulation results, we can expect that any heating modality (e.g., RH and INI) that can generate a homogeneous temperature elevation across the nerve cross-section will selectively inhibit small-diameter, slow-conducting subpopulations preferentially. Furthermore, the application of RH to vertebrates for selective inhibition is a promising next step, as selective INI has been explored in *Aplysia* and successfully translated to vertebrates with similar protocols but much lower ΔT [8,189]. Future research on the effects of RH on vertebrates can build upon the paradigms established in *Aplysia* and investigate the feasibility of size-selective inhibition (primarily on the unmyelinated fibers) *in vivo*. In addition, other heating modalities could be explored for their size selectivity during neural inhibition, including current neuromodulation modalities such as HFAC and ultrasound whose mechanism(s) may be related to heating (as mentioned in the Introduction).

RH showed less size selective variability than INI because of less spatial selectivity

In the present study, RH showed reliable size-selective inhibition when different nerves were tested, as shown in Figure 4.6. This was expected as the current design (a heating wire wrapping around the nerve) was selected to create a uniform temperature elevation

across the cross-section of the nerve. The simulated temperature distribution shown in Figure 4.7 (a and b) demonstrated the uniformity of the heating. Should the heating cuff be adopted for a chronic study, this spatial uniformity would minimize the likelihood that a shift in the orientation of the heating cuff after implantation would lead to a loss of size selectivity. Of course, if spatial selectivity is needed, a heating cuff could be designed to have multiple heating elements arranged around the nerve such that some control over the spatial thermal distribution could be achieved, especially in large-diameter nerves. Nevertheless, thermal conduction limits the spatial thermal gradient that can be created in this way.

In contrast, spatial selectivity may have adversely contributed to the variability in size selectivity for INI, as shown in Figure 4.6. Due to anatomic variability across different nerves, there are differences in the spatial arrangement of each axonal subpopulation within the nerve. Since IR light is incident on one side of the nerve, there is a spatial thermal gradient across the cross-section of the nerve, as can be seen in Figure 4.7 (a). The nerve region distal to the optical fiber tip has a lower ΔT because the light is strongly absorbed in the proximal region. Therefore, when the ΔT in the proximal region is high enough to induce inhibition (“hot side”), the subpopulation located distally may not reach the ΔT threshold yet (“cold side”). If the large-diameter subpopulation is predominantly located at the proximal end (“hot side”) and the small-diameter subpopulation is predominantly located at the distal end (“cold side”), the large-diameter subpopulation may be inhibited first. In other words, the variance in size selectivity observed in the INI experimental results is possibly a manifestation of spatial specificity. A previous study has shown that the high spatial specificity of IR light delivery can cause variance in the results of IR neuromodulation [188].

In short, RH showed a stronger and more robust size selectivity than INI (although not statistically significant) because of two reasons: 1) RH can generate a more even temperature distribution that is less prone to anatomical variability and changes of cuff orientation; 2) INI's spatial selectivity adversely affected its size-selectivity.

Resistive heating for implantable neural interface design

In this study, RH efficiently induced selective inhibition, making it a good candidate for an implantable neural interface design. Several additional aspects of implantable designs are therefore worth addressing.

Thermal safety

Although the ΔT requirement for RH of the *Aplysia* nerve is high (e.g., the ΔT_{50} shown in Table 4.3), a lower threshold can be expected when migrating to a vertebrate animal. When the INI protocol was migrated from *Aplysia* to musk shrews, the threshold ΔT for selective inhibition dropped from 9.7 ± 3.7 °C to 2.9 ± 0.8 °C [8]. Both the experimental and modeling results in the current study demonstrate that resistive heating and infrared neural inhibition rely on the same heat-based thermal block mechanism and the threshold temperature was very close. Therefore, a similar reduction in the temperature elevation threshold can be expected if resistive heating were transferred from *Aplysia* to vertebrates, as previous INI work demonstrated [8]. In addition, our modeling suggests that RH generated a spatially homogeneous temperature elevation across the nerve, as shown in Figure 4.7 (d), minimizing the danger of local overheating [188] due to spatial thermal gradient during INI as shown in Figure 4.7 (c).

The temperature threshold and safety margin of localized heating for neural block still need to be determined and can be effectively explored using resistive heating. From our experiments, a slight accumulative trend (not statistically significant) of RAUC after

repeated heating tests can be observed in Figure 4.4 (c). As the nerve in our current *in vitro* preparation is limited in its capability to respond to accumulated thermal stress, further *in vivo* experiments are needed to explore the accumulative effect of repeated localized heating on the nerve. It has been reported in humans that when core body temperature was elevated to about 40 °C, the reflex response mediated by the small-diameter afferent fibers was suppressed [116,117]. On the other hand, previous studies have shown that local heating higher than 45 °C on the peripheral nerve can cause irreversible neural block [144,252,262,263]. Recent studies have partially explored the safety margin of localized heating in neural tissue either with optogenetics in rats [166,264] or by resistive heating directly in mice [265]. Other recent studies have used a combination of cooling and heating to reduce temperature changes needed to induce block [120,123]. This new advance in thermal nerve block can use the heating cuff design in the current study to provide safe brief heating to lower the amount of cooling needed for block.

In short, the current study was not designed to directly address the safety of the potential *in vivo* application. Further tests are needed to assess if selective inhibition of small-diameter axons can safely be implemented via resistive heating. Resistive heating also provides a simple design for future experiments exploring the chronic safety of localized nerve heating, which could benefit the translation of other heating modalities.

The efficiency of the power applied at the neural interface and total electrical power

One major advantage of RH is that electrical power can be converted to heat very efficiently, but the heat has to be conducted through layers of materials until reaching the axons. While INI suffers from low conversion efficiency from electricity to light at the laser diode, the heat can be generated directly inside the nerve and does not rely on thermal conduction as RH did. As each modality has its advantages and disadvantages, we characterized the efficiency of the power applied at the neural interface and the efficiency

of total electrical power, to identify which modality is more feasible to be adopted as an implantable design in the future.

We first characterized how efficiently the power at the neural interface was converted into heat by comparing the power requirement at the interface (INI: optical power emitted from the optical fiber tip; RH: electrical power applied by the heating wire) for achieving the respective ΔT_{50} for a 50% inhibition probability of the small-diameter axons. INI required 39.8 mW of optical power emitted from the optical fiber tip to achieve its ΔT_{50} at 7.40 °C (the corresponding irradiance at the optical fiber tip is 14.1 W/cm^2). RH required 80.7 mW electrical power on the nerve surface to achieve its ΔT_{50} at 8.03 °C. The detailed data and linear regression of the power applied at the neural interface vs. ΔT for each heating modality across different nerves can be seen in Figure 4.8(a). INI was more effective in inducing ΔT compared with the current resistive heating cuff design when a given power was applied at the neural interface.

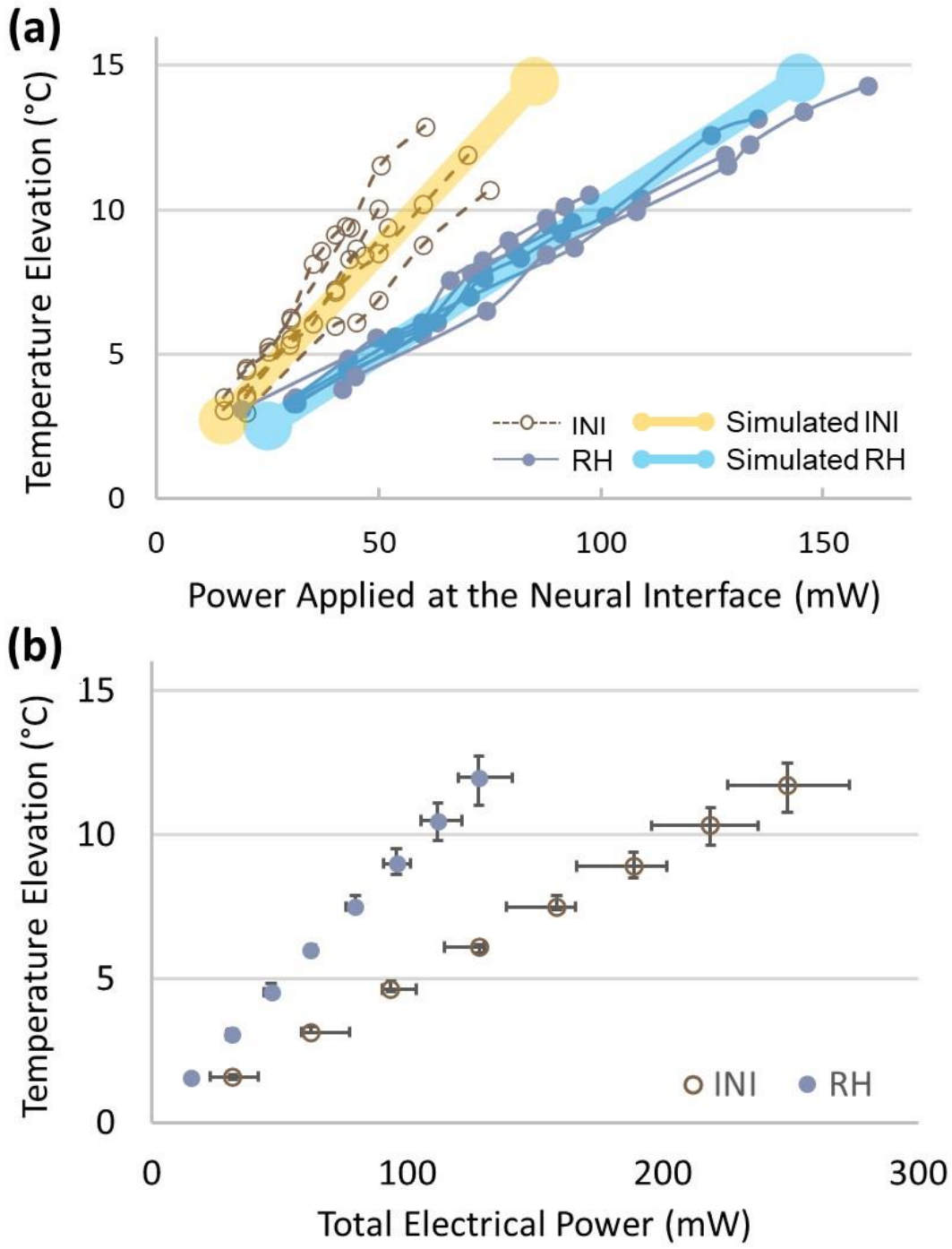

Figure 4.8. The power efficiency at the neural interface and the total electrical power were compared between infrared Inhibition (INI) and resistive heating (RH).

Brown dashed lines: INI. Blue: RH. (a): The efficiency of the power applied at the neural interface was evaluated by the temperature elevation (ΔT) when a given power was applied at the neural interface by INI or RH, across six tested nerves. The brown dashed lines with open circles are for

INI and the blue solid lines with filled circles are for RH. The results showed that the same power applied at the neural interface by INI can induce a higher temperature elevation, which means INI has higher efficiency for the power applied at the neural interface than RH. But the ΔT induced by RH is more repeatable across the six nerves. The semitransparent yellow line (for INI) and the blue line (for RH) are the simulated temperature elevation with given powers applied at the neural interface. The simulated heating response was consistent with the experimental measurement, showing that the model was a good approximation of the experimental setup (see Discussion). (b): The efficiency of total electrical power was evaluated as the total electrical power required for a given target ΔT. We conducted linear regression of the data to get the predicted values (the circles) and predicted intervals (the error bars). The results showed that RH only needs about half of the total electrical power required by INI to achieve the same temperature elevation.

The higher power requirement at the neural interface for RH can be attributed to the heating element size difference (INI: an optical fiber with a 0.6 mm diameter; RH: a heating wire surrounding 4.5 mm of length along the nerve). A larger heated volume would inevitably require more heating power. For the *Aplysia* nerve we tested here, the optimum length would be approximately 1 mm according to our previous study [191,192]; a heat block length beyond that does not improve the efficacy of the thermally induced neural inhibition. The current 4.5 mm length was selected due to the limitations of the manual fabrication process and to ensure that effective neural inhibition can be observed. Another factor of the power requirement difference can be attributed to the location of heat generation (INI: inside of nerve, RH: outside of nerve). Future studies can explore the feasibility of safely inducing heat inside the nerve for the heat-based neural block. In addition, with a given amount of power applied at the neural interface, the ΔT induced by RH was more repeatable across the six tested nerves, compared with INI. The 360° wrapping design of the heating cuff is less sensitive to variability in the nerve anatomy and the nerve's relative position in the heating cuff. Because of this repeatable heating response, an RH-based heating cuff is expected to be less prone to movement following chronic implantation.

We then characterized the total electrical power consumption of the two modalities for achieving the given final ΔT values. For example, to achieve an inhibition probability of

50% on the small-diameter axons, INI needs 155.9 mW total electrical power for its ΔT_{50} at 7.40 °C whereas RH only needs 85.2 mW total electrical power for its ΔT_{50} at 8.03 °C. Due to the difference in the efficiency of total electrical power, the current resistance-heating nerve cuff could have a 55% longer runtime than the INI laser used in this study. Indeed, for the current heating cuff design, 93% of the total electrical power can be converted to the power applied at the neural interface, whereas the laser diode can only convert 24-27% of the total electrical power into the optical power of infrared light applied to the nerve.

The current cuff design was only a proof-of-concept and could be further optimized for improving its efficiency in future studies. For example, the inner PDMS tube of the heating cuff could be thinner or altered to achieve better thermal conductivity [266–268]. This could promote better thermal conduction from the heating wire to the nerve and increase the efficiency of the power applied at the neural interface. Second, with a finer manufacturing process, the length of the axial heated region of the heating cuff could be shortened to the optimal length requirement. A microfabrication process could achieve much better control of the heating element morphology and integrate the thermal sensor in a smaller dimension, as demonstrated in previous studies [265,269,270]. In addition, a customized temperature controller could be made with parameters optimized for RH to help reach the target temperature quicker and avoid fluctuation/overshooting. It is worth noting that the *in vivo* thermal condition will be different from the *ex vivo* experimental setup (e.g., intraneural blood flow can cause additional heat dissipation), which may lead to changes in the heating power requirement. A recent study has observed an inhibitory effect on neural activity by resistive heating in the cortical tissue of mice *in vivo* [265]. More future experiments will be needed for characterizing the effect of *in vivo* thermal conditions

(e.g., intraneural blood flow) during the heat-based neural block, both acutely and chronically.

Biocompatibility

RH has the potential to meet the biocompatibility requirements for an implantable neural interface. The current heating cuff design can be made of inert and biocompatible materials to match the mechanical compliance of tissue, thereby minimizing deleterious mechanical effects and associated foreign body response [271,272]. In addition, the RH cuff does not inject charge into the tissue, as standard electrical stimulation and block methods do, and therefore will not induce charge-injection-related tissue damage [106,273,274]. The heating circuit was driven by direct current and was fully insulated, thus reducing the likelihood of interfering with other electrophysiological electrodes (recording/stimulation) that may be present in the surrounding tissue.

4.2.5 Conclusions

In this study, we explored the possibility of using RH to reproduce INI's size-selective inhibitory effect on small-diameter axons. The dose-response curves of both modalities showed a similar trend of increased inhibition probability when ΔT was increased. RH reproduced the selective inhibition of slow-conducting small-diameter axons. The measured nerve surface ΔT for a 50% probability of inhibition on the slow-conducting small-diameter axons was 7.40 °C for INI and 8.03 °C for RH. Simulation of the heating process revealed that the average ΔT in the axon-containing region of the nerve was similar (9.39 °C for INI, and 9.40 °C for RH). While INI showed a higher heating efficacy by depositing energy directly inside the nerve, RH showed a higher overall energy efficiency because the heating wire can efficiently convert electricity to heat. These results demonstrate that the selective neural inhibition effect of INI can be reproduced by another

heating modality such as RH. Furthermore, the high overall energy efficiency of RH can facilitate further development of battery-powered implantable devices, increasing the availability of selective inhibition of small-diameter axons in basic research and translational applications.

Chapter 5. Conclusion and future directions

The research in this dissertation showed that combining size-selective infrared neural inhibition with extracellular ion replacement can lower power thresholds and that the size selectivity of small-diameter axons can be replicated using other heating methods such as resistive heating. It is important to note that the size selectivity of small-diameter axons was preserved either by combining with ion replacement or by reproducing the effect using resistive heating. The numerical simulation results of the temperature distribution across the nerve also confirm and strengthen the experimental finding that both resistive heating and infrared neural inhibition induce selective inhibition by raising the baseline temperature of the nerve. Overall, the findings support the previous hypothesis in the 2017 Lothet et al. paper that modalities that primarily affect the axon membrane will have a size selectivity preference for small-diameter axons, which is different from the spatial selectivity that has been studied previously. This provides researchers and doctors with a more comprehensive set of tools to study the role of small-diameter axons and identify potential treatments for conditions caused by the dysfunction of small-diameter axons.

Other than being used as an inhibition modality, the thermal inhibition threshold of nerves can be used to assess the nerve's underline health condition. Even with the pathological disruption (e.g., diabetic peripheral neuropathy) to extracellular ion composition, neural conduction velocity may not show a significant change [275,276], and neurons can still integrate inputs and generate an all-or-nothing response as if there is no pathological process happening. From a macroscopic view, a patient may not experience any significant functional difference until the pathological process is severe enough to block neural conduction, making the early detection of neuropathy difficult. This is also supported by the experimental results that sub-threshold ion-replaced saline cannot block

neural conduction but lowered the power threshold of infrared neural inhibition. One potential way to interpret the result in chapter 3 with isotonic ion replacement is that the nerve's sensitivity to infrared neural inhibition depends on the homeostasis of normal extracellular ion composition in the nerve. Therefore, when a pathological process (e.g., diabetes) in a patient's body induces an alternation to the extracellular ion composition in the nerve, we can expect a lowered threshold of infrared neural inhibition. In another word, the threshold test of infrared neural inhibition (or other thermally-mediated neural inhibition) can be used as an early identification method of the pathological alteration to the extracellular ion composition in the nerve.

The results in chapter 4 have demonstrated that resistive heating is a viable alternative to infrared neural inhibition in *ex vivo* experimental setups. To further understand its potential for *in vivo* use, future experiments consisting of electrophysiological, behavioral, and histological tests are needed to examine the effects of localized heat application on nerves both acutely and chronically. It is important to explore how the *in vivo* condition affects the temperature threshold, size selectivity, and safe operating margin. The numerical simulation in chapter 4 revealed that both resistive heating and infrared neural inhibition can create a temperature gradient within the nerve. However, in order to reach the desired temperature increase, there is a risk of overheating other areas of the nerve. It is not a significant issue as the current study was conducted on *Aplysia* nerves with a diameter of around 600 μm. When resistive heating is used on larger nerves in vertebrates and humans, it may be difficult to generate sufficient heat penetration due to the heat being produced outside of the target nerve. While resistive heating is highly efficient at converting electricity to heat, the limited depth of heat penetration may restrict its use in larger nerves, particularly when intraneural blood flow can dissipate heat within the nerve.

Besides size-selective inhibition, future studies can also explore the feasibility of spatial selectivity with thermally-mediated neural inhibition modalities. The numerical simulation results in chapter 4 showed that both resistive heating and infrared neural inhibition have limited heat penetration depth. By using a multi-heating-element design or a multi-optical-source design, desired spatial heat distribution may be achieved, which can be beneficial for targeting a specific fascicle in the nerve, especially for larger-diameter nerves with multiple fascicles.

Future neural interface designs for thermally mediated neural inhibition, especially resistive heating, can be derived from many existing designs of electrode-based neural interfaces. Also, it could be useful to combine electrode-based neural inhibition with thermally-mediated neural inhibition on the same nerve to determine if there is any potential synergistic effect between the two inhibitory modalities. For example, infrared neural inhibition has been demonstrated to block the onset response of high-frequency alternating current (HFAC) neural inhibition [209]. As an electrical method, it will be easier to combine resistive heating with HFAC for achieving similar onset-free neural inhibition.

To apply size-selective neural inhibition in a clinical setting, the requirements of the intended use should be taken into account in the development of future thermally-mediated neural inhibition solutions. Determining the appropriate clinical scenario is essential because it will influence the geometry and anatomical features of the target nerve, which will subsequently determine the most suitable heating method for achieving optimal size-selective inhibition. Size-selective neural inhibition has potential clinical applications beyond the current neural inhibition scenarios and can also be used in scenarios involving denervation. As current clinical approaches lack size-selectivity, denervation processes such as surgical cutting or ablation are used as a last resort for

conditions caused by the dysfunction of small-diameter axons, but this comes at the cost of losing all neural connections and causing unwanted side effects.

In summary, the present research explores more modalities for size-selective inhibition of small-diameter axons. The experimental modeling results suggested that various thermally-mediated modalities (e.g., infrared neural inhibition and resistive heating) can achieve size-selectivity on small-diameter axons. Further studies in this direction can help researchers and physicians explore the functionalities of small-diameter axons and develop future therapeutic options.

Appendix A. Exploration of the parameter space of infrared neural inhibition

A.1 Background

This appendix includes the preliminary parameter exploration for infrared neural inhibition. The conventional infrared neural inhibition protocol uses pulsed infrared light at 1470 nm or 1860 nm, 200 Hz, 200 μs (i.e., 4% duty cycle), and the average power of the infrared light is adjusted for the desired inhibitory effect. There are several reasons for exploring the parameter space of infrared neural inhibition. First, applying too much infrared light can be unsafe due to the risk of tissue overheating and it would be advantageous to have a greater margin between the inhibition threshold and the damage threshold. Second, the current infrared neural inhibition protocol was identified within the hardware limit of the laser available during the initial research. By expanding the choice of lasers and laser drivers, it is feasible to explore a bigger range of parameter space to identify the optimal parameter combination. Third, the current infrared neural inhibition protocol has a very low duty cycle (4%), which requires expensive and dangerous class IV laser diodes due to the peak power requirement. It will be helpful if a higher duty cycle can be used for infrared neural inhibition. Fourth, lowering the peak power requirement may allow us to use cheaper and safer laser diodes. This could also lead to implantable systems that could last longer. Last, the current infrared neural inhibition system uses the 1470 nm and 1860 nm laser wavelength, which has a strong water absorption coefficient. It can be helpful to use a wavelength (1330 nm or 1550 nm) with a lower water absorption coefficient for penetrating deeper into the tissue. Laser diodes at those wavelengths, owing to their wide

application in the optical communication and automotive industry, are massively produced and much cheaper and more optimized.

A.2 Experiment Protocol and control tests

Infrared light was tested with different temporal parameters. The baseline protocol is 200 Hz and 200 μs. The IR power was varied to find the IR power threshold for the desired inhibitory effect.

To identify the threshold IR power of each IR protocol, here are the steps.

- Pick an IR power level based on previous experiments that can induce selective inhibition on small-diameter axons.
- Apply IR light and look for inhibition of CAP
- Vary the IR power level to confirm it is the threshold
- When the threshold is found under one protocol, the compound action potential under inhibition is saved as a template for the threshold-finding process of other protocols with different parameters.
- Apply the IR light with other protocols and vary the IR power to match the inhibitory effect on the CAP.

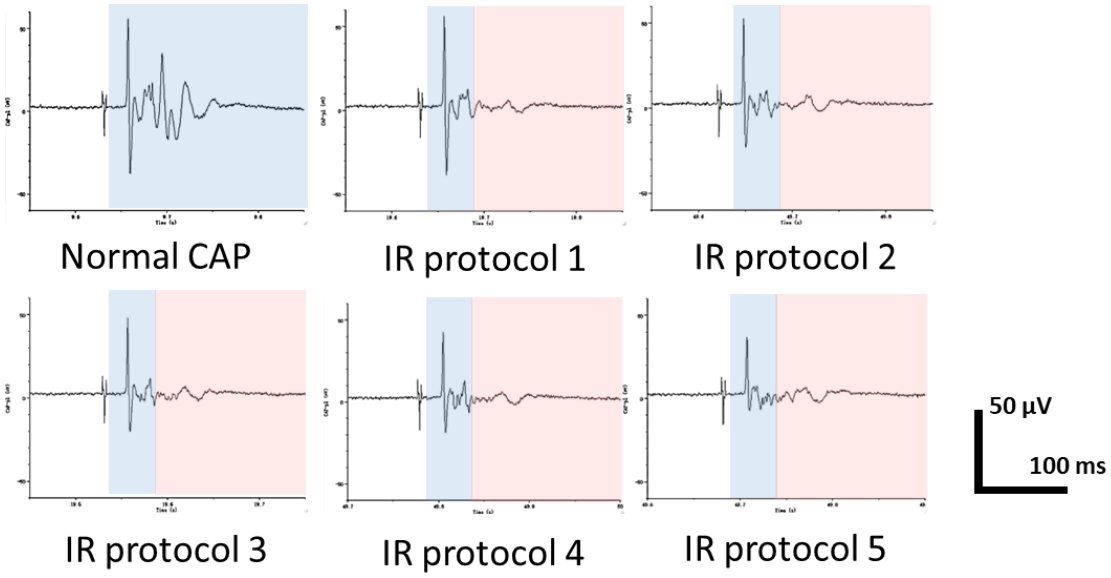

Figure A.1. Examples of different IR protocols tested on the same nerve to identify similar inhibitory effects on the compound action potentials.

An appropriate control test was conducted between IR applications to assess the nerve's health. If the CAP showed a significant difference compared with the control CAP, the experiment would be terminated.

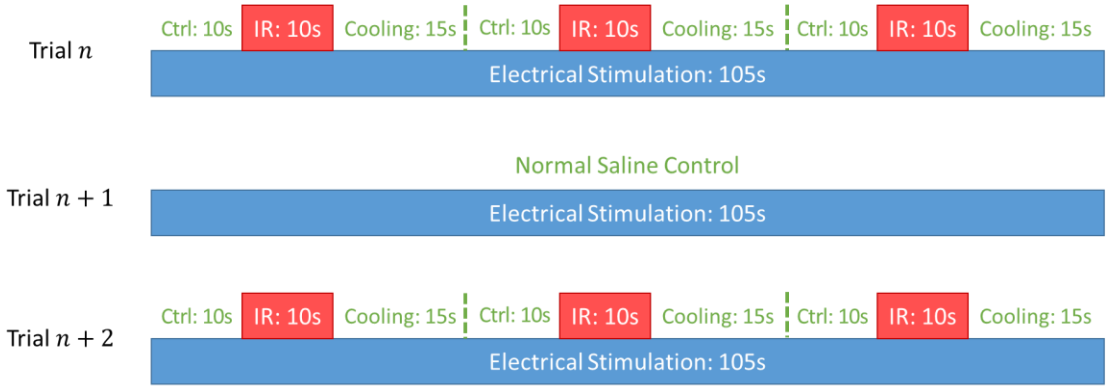

Figure A.2. Schematic of the experimental protocol.

In each IR testing trial (e.g., trial n and n+2), the infrared light application was repeated 3 times, with control and the cooling period before and after each infrared light application. Electrical stimulation was conducted throughout the testing trials to test the status of neural conduction. Normal saline control trials (e.g., trial n+1) were also done between IR testing trials for assessing the nerve's health.

The parameter space exploration requires repeated tests on the same nerve. It is necessary to know how long a stable CAP can be evoked on the same nerve. We conducted repeated electrical stimulation on two halves of the same nerve (N = 4). Overall, the two halves of the same nerve showed similar CAPs in the 2 experiments. Variability during the surgical process and the application of suction electrodes can cause differences between the CAPs recorded from the two halves of the same nerve. But mainly, it was the difference in amplitude, the location of peaks and troughs were similar. Because of those variabilities, the rectified area under the curve (RAUC) was not always at a similar level.

Finally, the two halves of the same nerve showed similar surviving times and a run-down trend.

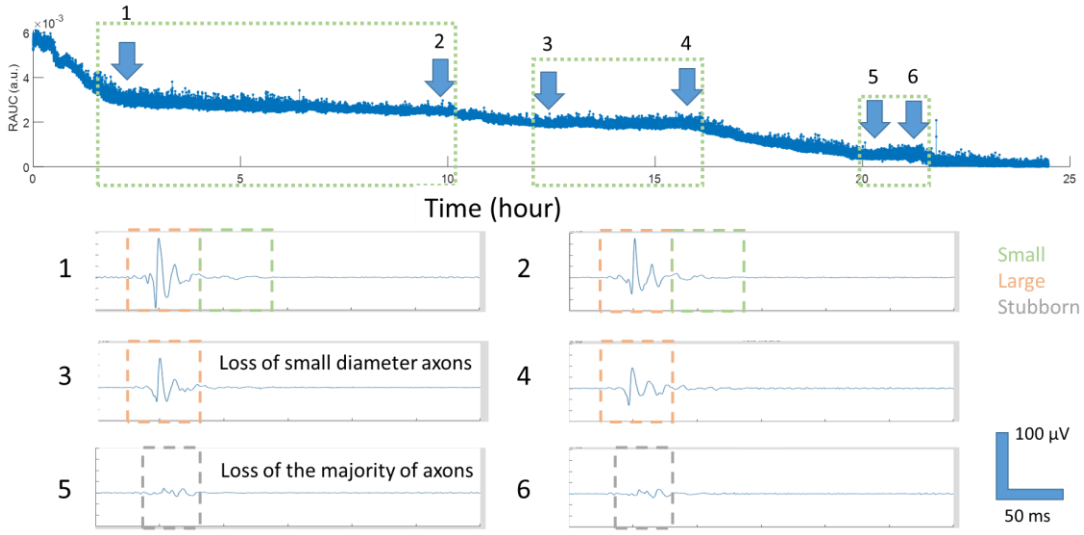

Figure A.3. The rundown tests showing CAP deterioration between different stages of rundown.

The top panel shows the rectified area under the curve of the same nerve during repeated electrical stimulation for 24+ hours. A box with a dashed green line indicates where the CAP remains relatively stable. Blue arrows indicate the time points where representative CAPs are shown in the lower panels (1 to 6). The CAPs between different stages showed that the response from small-diameter axons (Green) is diminished first before the large-diameter axons (Orange). Panels 5 and

6 show the "stubborn" component that was in the middle conduction velocity range and the last component diminished.

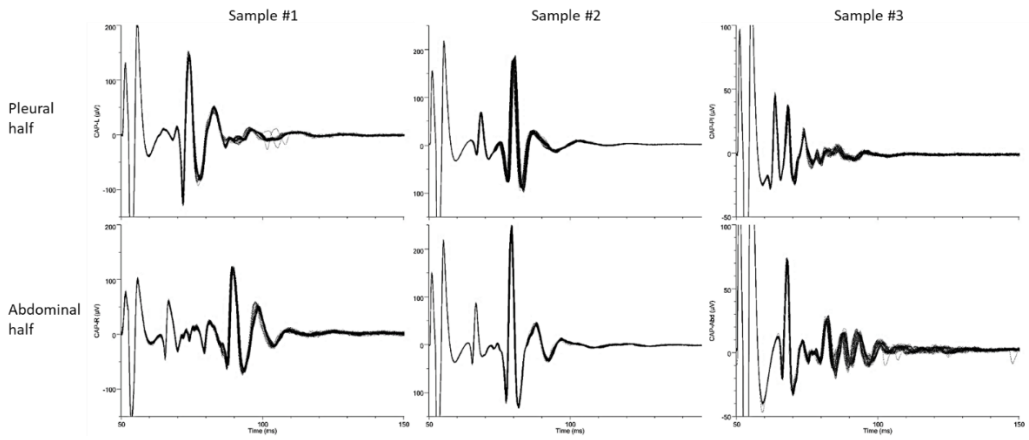

Figure A.4. Compound action potentials from two halves of the same nerve.

The figure shows the representative compound action potentials from two halves of the same pleural-abdominal connective from Aplysia. The top row is the response from the pleural half and the bottom row is the response from the abdominal half. Each column is the response from one sample. In each panel, CAPs of repeated tests on the same nerve were overlayed to show the variability of CAPs over time.

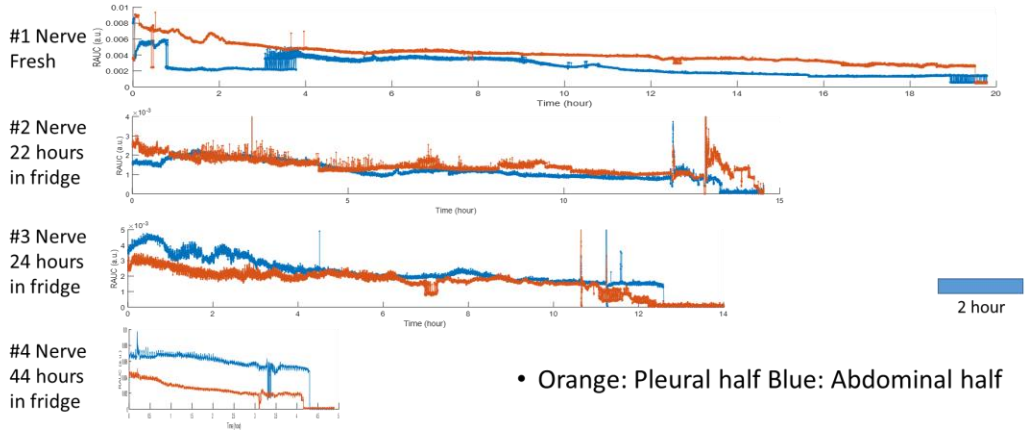

Figure A.5. Rectified area under the curve of the CAPs recorded from two halves of the same nerve with repeated electrical stimulation.

The rectified area under the curve (RAUC) from the two halves of the same nerve showed similar trends of rundown when electrical stimulation was repeated for a long period. Nerves were tested with different storing times in the fridge before the test. It can be observed that fresh nerves can last longer during a repeated electrical test. Storing the nerve in the fridge longer than 24 hours can diminish the nerve's survival time.

Compare of IR inhibition threshold on 3 positions

IR inhibition threshold was tested 3 times on the same nerve at different positions (n=1). This can help us evaluate the error margin of the threshold-finding process and if we can compare the threshold from one nerve to another

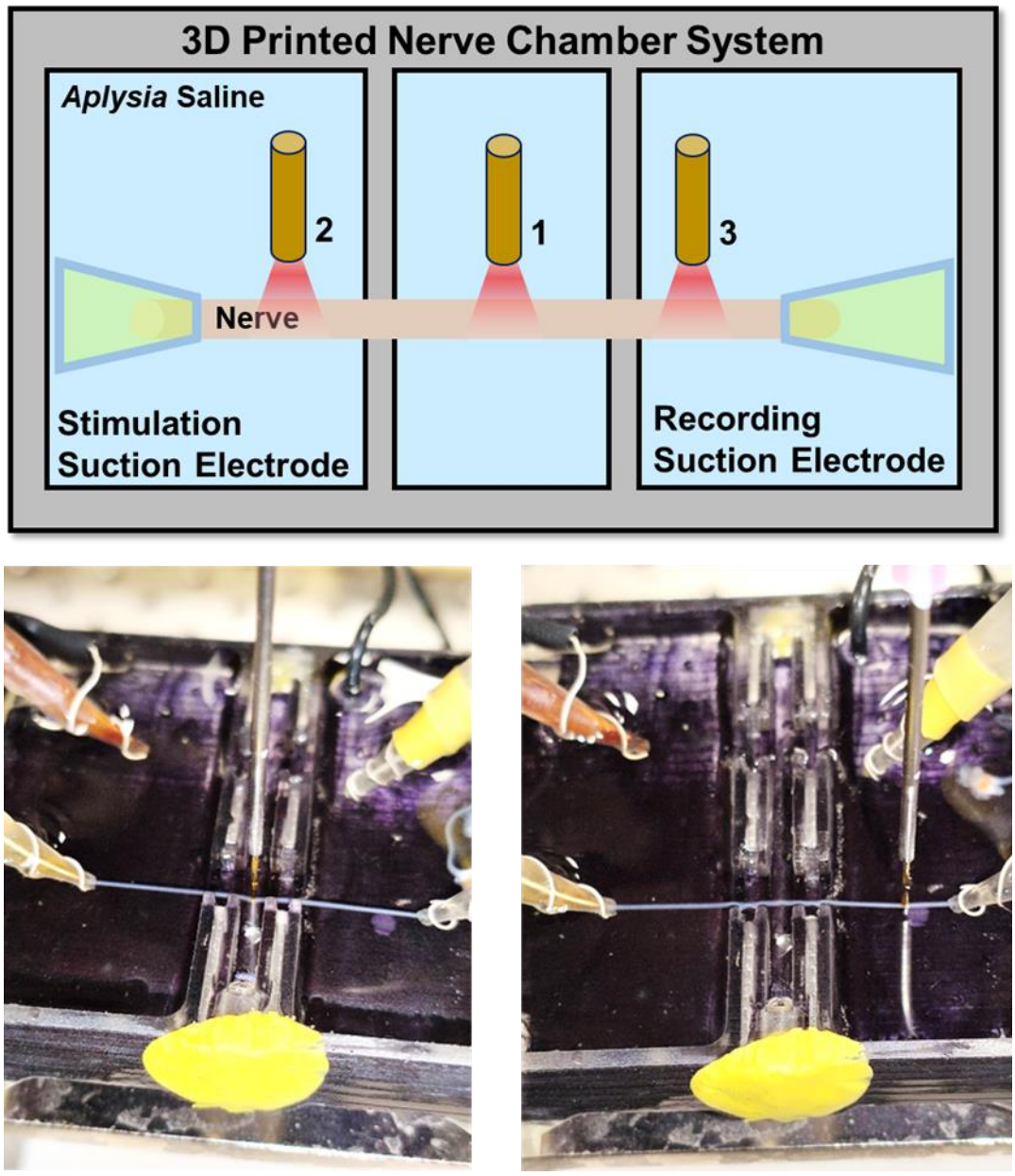

Figure A.6. Experimental schematic (top) and representative photos (bottom) of the infrared neural inhibition threshold test on 3 different positions of the same nerve.

The top panel is the schematic diagram of the repeated test on different points of the same nerve. The lower two panels show the representative optical fiber positions during the test.

We recorded the CAPs under different infrared light power levels. The RAUC was calculated and normalized to the control test with infrared light application. A sigmoid fit was conducted to identify the average IR power threshold. The test results from the three positions on the same nerve were similar as shown in Figure A.7, with an average value of 27.6 mW $\pm$ 2.0 mW. The potential reasons for the variance include fiber aiming difference, axon orientation difference, and carry-on effect from the previous test. Further development of the test method and more experiments are needed.

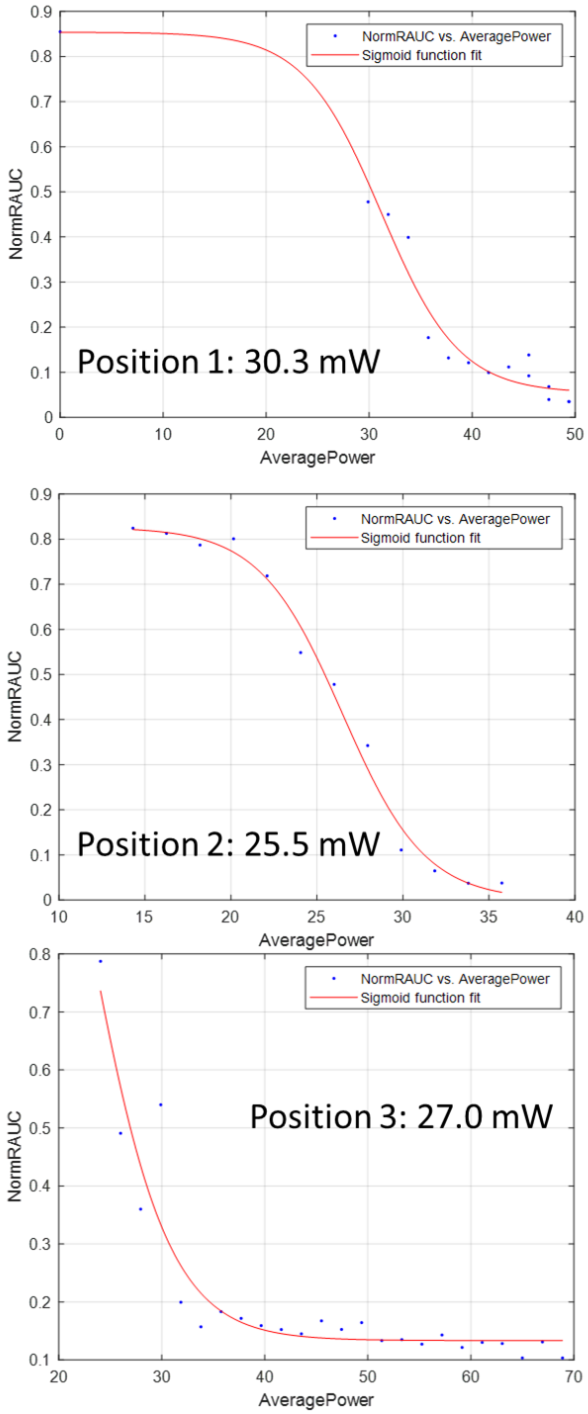

Figure A.7. Normalized RAUC response vs. average IR power.

The blue dots marked the raw RAUC data points. The threshold average power for achieving a normalized RACU lower than 0.5 was identified for each position via sigmoid fitting as marked by the red lines.

A.3 Comparison of kHz frequencies

For the test, a QPhotonics 1480nm 500 mW single mode (SM) laser diode was coupled to an ocean optics multimode optical fiber with a core diameter of 600 µm. Frequency was increased while the same duty cycle (~50%) was maintained. The preliminary test (n=2, showed that the average IR power thresholds required with different frequencies (1250 Hz, 5000 Hz, 15000 Hz) were not significantly different from the threshold at the continuous wave (CW) mode, which showed that the peak IR power was not the critical factor for the inhibitory effect. The axonal region diameters of the two nerves tested were 251 µm for nerve 1 and 393 µm for nerve 2, which may contribute to the higher average power threshold compared with nerve 1 (52.9 mW for nerve 1 and 76.4 mW for nerve 2). In another representative data set, different combinations of IR pulsing frequency and duty cycle, including the CW mode, were tested on the same nerve with increasing IR power. Each IR session was 10 seconds long with a 10-second interval. The testing results showed that with a frequency higher than 625 Hz, the response with various IR pulsing protocols is similar to the response to CW mode.

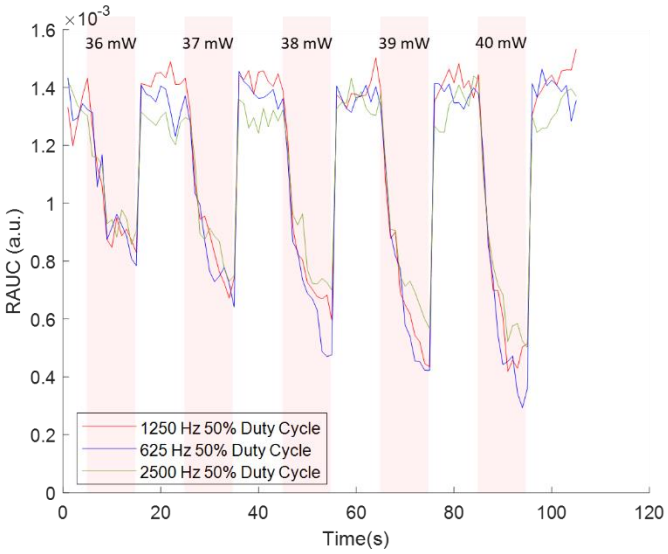

Figure A.8. The RAUC response when the same IR power steps were tested on the same nerve with different IR pulsing frequencies and the same duty cycle.

The light red blocks indicate when the IR light was applied during the test. The RAUC responses under different IR pulsing frequencies are overlayed to compare the response. Different colors represent the responses from different IR protocols. The responses from different IR pulsing protocols were very similar when the same average IR power was applied, suggesting that IR pulsing frequency is not critical for the response.

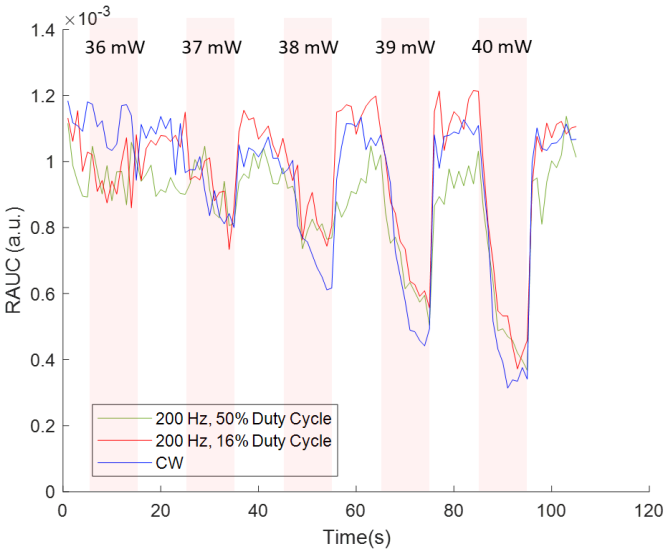

Figure A.9. The RAUC response when the same IR power steps were tested on the same nerve with different IR pulsing duty cycles at 200 Hz and the CW mode.

The light red blocks indicate when the IR light was applied during the test. The RAUC responses under different IR pulsing duty cycles and the CW mode are overlayed to compare the response. Different colors represent the responses from different IR protocols. The responses from different IR pulsing duty cycles and the CW mode were very similar when the same average IR power was applied, suggesting that IR pulsing duty cycle is not critical for the response.

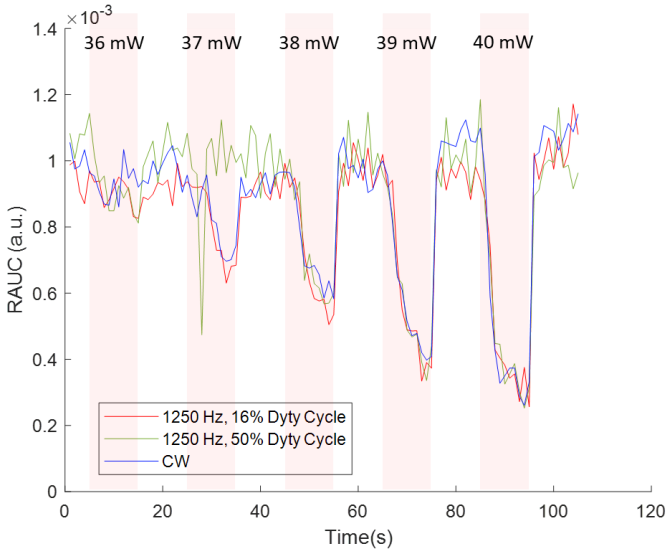

Figure A.10. The RAUC response when the same IR power steps were tested on the same nerve with different IR pulsing duty cycles at 1250 Hz and the CW mode.

The light red blocks indicate when the IR light was applied during the test. The RAUC responses under different IR pulsing duty cycles and the CW mode are overlayed to compare the response. Different colors represent the responses from different IR protocols. The responses from different IR pulsing duty cycles and the CW mode were very similar when the same average IR power was applied, suggesting that IR pulsing duty cycle is not critical for the response.

A.4 An extended comparison of various frequency and pulse width combinations

Various IR pulsing frequency and pulse width combinations were tested with SemiNex MCM-102 laser diode at 1443 nm on *Aplysia* pleural-abdominal nerve (n = 3) to identify the IR average power threshold of the same inhibitory effect. We tested various combinations of IR pulsing frequencies (10, 20, 25, 50, 100, and 200 Hz) and pulse width

(0.5, 0.7, 1, 2, and 4 ms) as the IR pulsing protocol. From the results, keeping the frequency the same and changing the pulse width did not cause significant changes in the average IR power threshold. The only exception was for one nerve at 20 Hz and 0.5 ms pulse width, which showed a 40% higher IR power threshold level than the thresholds with longer pulse widths. The combination of low duty cycle and low frequency may likely lead to significant cooling of tissue between IR pulses and a higher power threshold.

Overall, the results implied that the IR average power threshold does not depend on the IR pulse frequency or pulse width when the frequency is higher than 50 Hz.

A.5 Comparison between MHz fs-laser and kHz ms-laser

The same nerve was tested with either MHz fs-laser or kHz ms-laser, both at 1443 nm center wavelength. Both lasers were coupled alternatively into the same optical fiber for light delivery onto the nerve. The Fs laser was selected to run at 1443 nm (central wavelength).

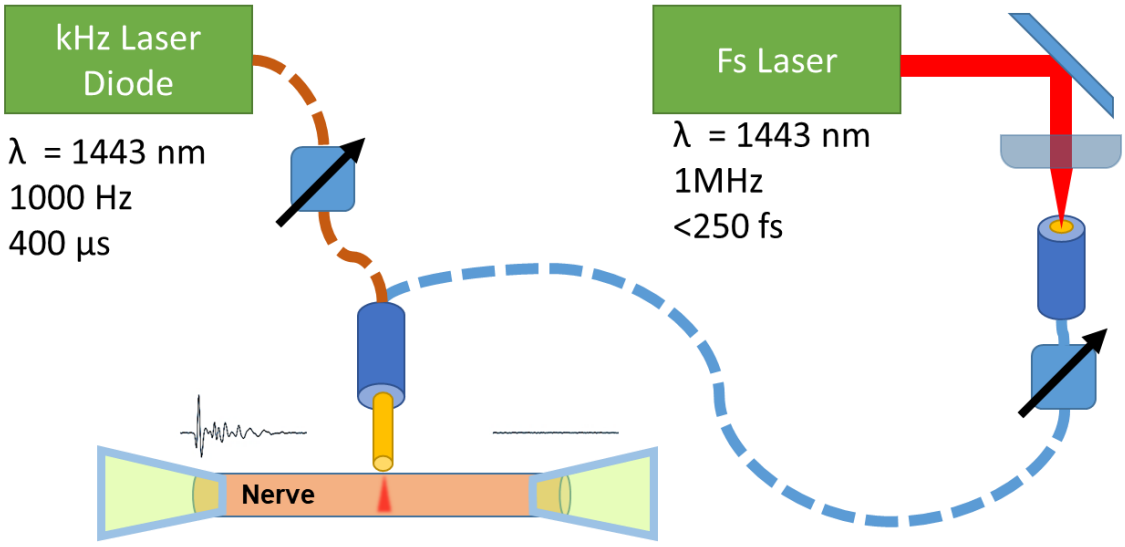

Figure A.11. The experimental schematic of the MHz vs kHz laser comparison test.

An Aplysia pleural-abdominal connective nerve was electrically stimulated and recorded with suction electrodes on each side to assess the status of neural conduction. An optical fiber was

pointed at the middle point of the nerve for light delivery. The MHz and kHz lasers were connected to the light delivery optical fiber alternatively for the test. Attenuators were connected in each light path to adjust the optical power.

From the testing results (n = 3), the threshold for the MHz fs-laser (56.7 $\pm$ 1.2 mW) was not significantly different from the kHz ms-laser (55.7 $\pm$ 3.9 mW). This suggests that the average power threshold does not depend on the IR pulsing frequency when the IR pulsing frequency is higher than 1000 Hz

A.6 Comparison between 1443 nm and 1550 nm for infrared neural inhibition

The 1470 and 1860 nm wavelengths that are commonly used in the previous infrared neural inhibition research are located at the peaks of the water absorption coefficient curve. The strong water absorption induced the thermal effect that is critical for the inhibitory effect, but also limited the penetration depth of the light. We conducted the wavelength comparison test to explore if using an IR wavelength that has a weaker water absorption coefficient can allow a deeper light penetration depth and lower the IR inhibition threshold. We conducted the test using the same femtosecond laser at different wavelengths (1443 nm vs 1550 nm) and compare the average power threshold for inducing a similar inhibitory effect on the same nerve. The experiment setup is similar to Figure A.11, except the kHz laser diode was not used.

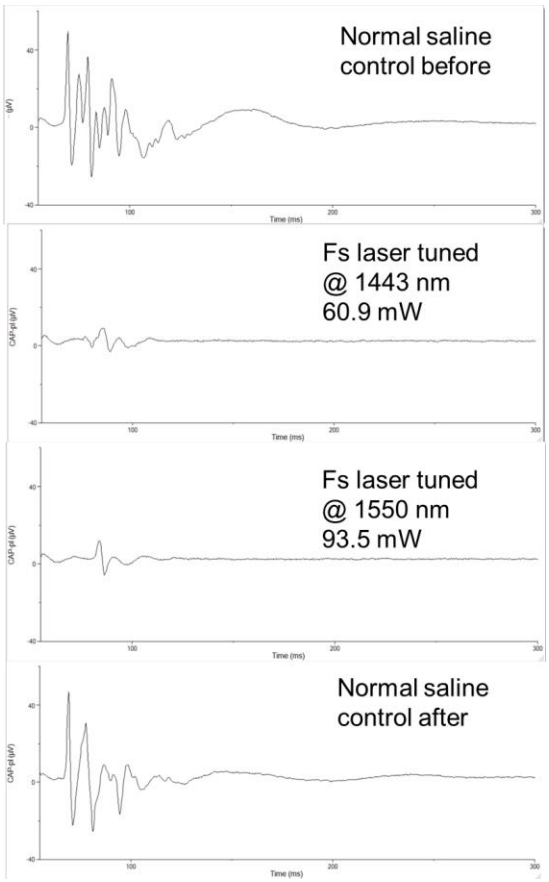

Figure A.12. Representative CAPs during the application of two different IR wavelengths and the control tests before and after the infrared neural inhibition.

The representative CAPs during the IR application test with different wavelengths showed a similar inhibitory effect of the majority of the CAP components. The control test before and after the IR applications did not show any significant difference, suggesting that the inhibitory effect is transient and reversible.

We conducted the tests on four different segments of the nerve, including a pair of two halves from the same nerve. Each segment was either the pleural half or the abdominal half of the pleural-abdominal connective from *Aplysia*. With the experiment data, the average IR power threshold at 1550 nm is 78.3 ± 14.8% higher than the threshold at 1443 nm, as shown in Figure A.13. The water absorption coefficient is 32 [1/cm] and 12 [1/cm] for 1443 nm and 1550 nm respectively. Correspondingly, the 1/e penetration depth for 1443 nm and 1550 nm IR light is about 312.5 μm and 833.3 μm. The higher IR power

threshold of 1550 nm may be attributed to the escaping of IR light from the nerve region since the 1/e penetration depth of 1550 nm is larger than the average diameter of the *Aplysia* pleural-abdominal connective. Future tests with larger-diameter nerves may be able to reveal the benefits of having an IR light wavelength that can penetrate deeper into tissue.

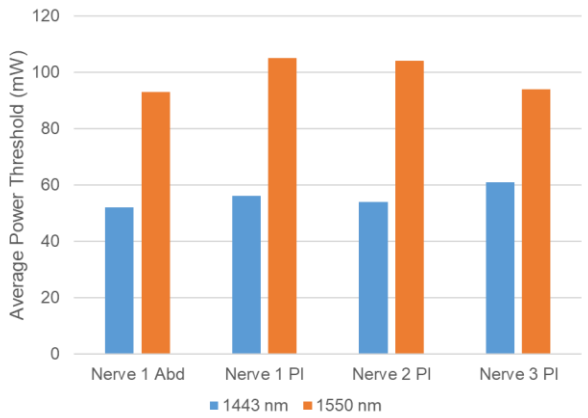

Figure A.13. The comparison of the average IR power threshold between 1443 and 1550 nm.

For achieving a similar full inhibition effect on the same nerve, the average IR power threshold at 1550nm is 78.3±14.8% higher than the threshold at 1443 nm.

A.7 Summary of comparisons with different IR protocols

The test results from different comparisons, including different frequencies higher than 1 kHz, different pulse widths and frequency combinations under 200 Hz, and the MHz laser vs kHz laser, all showed that the average power thresholds were similar on the same nerve when different IR protocols were tested. This suggested that the average power is the critical factor for the inhibitory effect as infrared neural inhibition relies on the thermal effect induced by the absorption of IR light. The previous study has shown that thermal relaxation time in *ex vivo* neural tissues is about 1 second [189]. Since most of the IR protocols tested have a pulsing period much shorter than this, the temporal fluctuation caused by each IR pulse was evened out when the fluctuations overlapped with each

other as shown in Figure A.14 by the thermocouple measurement of water temperature under IR radiation.

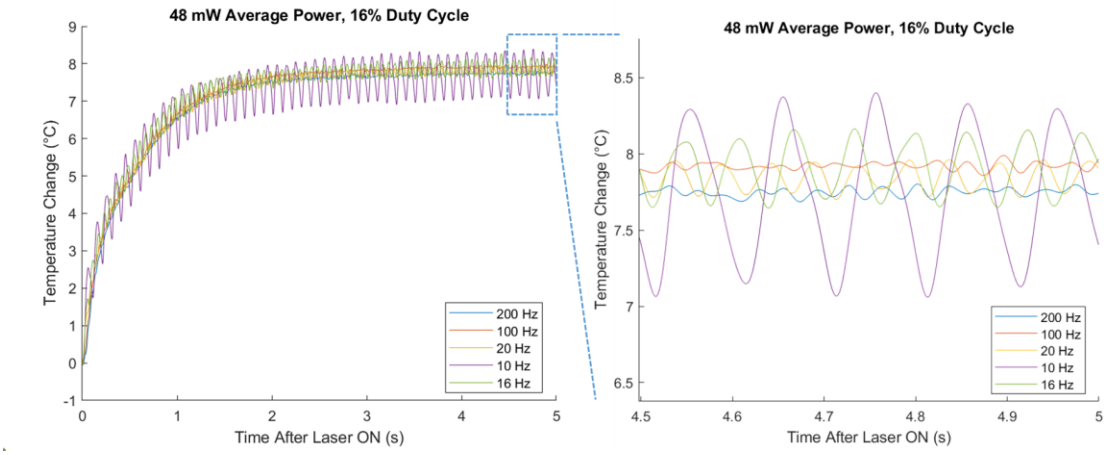

Figure A.14. The temperature change in water induced by IR radiation at the same duty cycle but at different frequencies.

A thermocouple with a diameter of 200 µm was immersed in the water right beneath an optical fiber with a core diameter of 600 µm to measure the temperature change induced by the IR radiation. Different IR pulsing frequency was applied while the average IR power and duty cycle were maintained. The measurement results showed that with a frequency higher than 100 Hz, the temperature fluctuation caused by IR pulsing was very small (about 2% of the stable temperature). The right panel is the zoomed-in view of the region marked in the blue square of the left panel.

In short, for infrared neural inhibition, average IR power and tissue absorption of the IR light wavelength are the primary factors and pulsing may not be necessary.

A.8 Preliminary data of prolonged IR inhibition

At the end of the previously described IR parameter tests, average IR power was set to 2 times higher than the identified full inhibition threshold to explore if we can observe a prolonged IR inhibitory effect after the IR laser is turned off. The testing target was *Aplysia* pleural-abdominal connective. IR protocol: 1250 Hz, 400 µs, each session is 5 seconds long with a 5-second interval and repeated 8 times. The IR test was designed to be acute with short intervals since the IR power to be tested may cause a carry-on effect on the

nerve. From the preliminary test on three nerves, the IR power threshold for irreversible inhibitory effect (96.7 mW on average) was about 2 times higher than the IR power threshold for reversible full inhibition (51.7 mW on average).

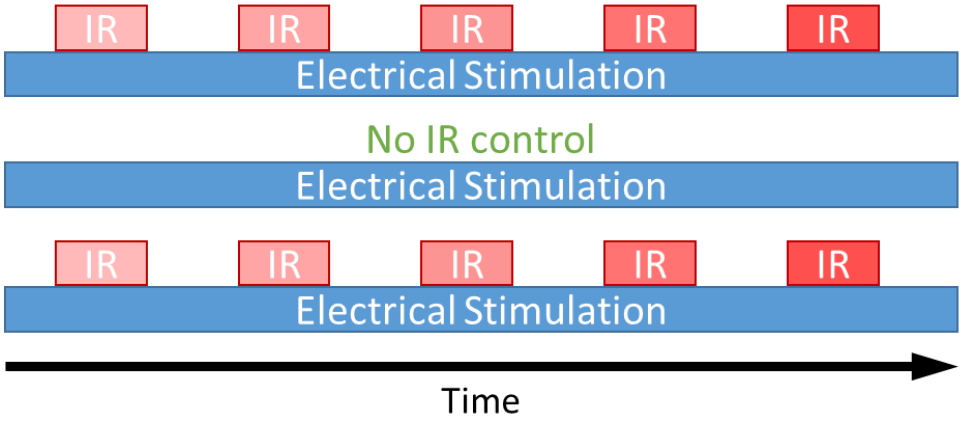

Figure A.15. The schematic diagram of the testing protocols used for prolonged infrared neural inhibition.

The infrared neural inhibition testing protocol was 1250 Hz, 400 µs, each session is 10s long with 10s intervals and repeated 8 times in each testing trial. The IR power was gradually increased in each IR session to achieve the desired inhibitory effect. Pure electrical stimulation testing trials were conducted between testing trials for assessing the nerve's health.

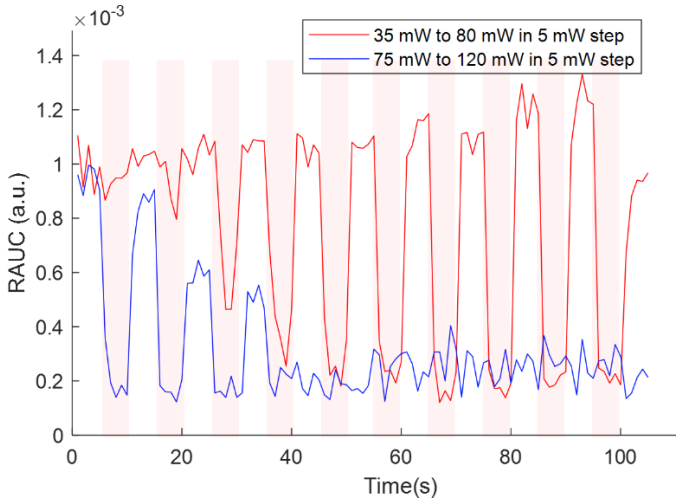

Figure A.16. The acute response to increasing IR average power on the same nerve.

Two IR testing trials of RAUC when increasing IR average power was tested on the same nerve are overlayed. The light red blocks indicate when the IR light was applied. The repeated IR application test showed a full inhibition threshold at 55 mW average power and an acute irreversible inhibition threshold at 90 mW average power.

Here are the testing steps:

1) Normal Saline Control Test: The normal saline control test was repeated until the CAPs are stable between tests.

2) Partial and full inhibition threshold test: Different levels of IR power were tested to identify the partial and full inhibition threshold test. The IR power threshold for full inhibition is referred to as I_full in the following steps. During the threshold finding process, normal saline control tests were conducted between IR applications to assess the nerve's health.

3) Exploration of prolonged inhibition effect: Test of different levels of IR power (I_test = K * I_full) to explore the potential prolonged inhibition effect. Our preliminary test has indicated that irreversible inhibition was happening with IR power about one time higher than the full inhibition threshold (i.e., K ≈ 2). Therefore, we tested the following IR protocols based on the ratio above the full inhibition threshold.

    a) IR protocol 1: Burst 10s and off 5s, repeat 6 times per test. Repeat the test for a total of 2 trials or less if partial prolonged inhibition was observed (K = 1 ~2)

    b) IR protocol 2: Burst 1s and off 5s. Repeat the test for a total of 2 trials or less if partial prolonged inhibition was observed (K >2)

    Whenever there was a prolonged inhibition, the test is terminated and switched to the next step.

4) Nerve rundown test: We repeated the normal saline control test every 3 minutes to observe if there is any recovery of the neural conduction. The test was repeated until the CAP disappeared or the experimenter has to take bio-breaks.

The representative raw signal in Figure A.17 showed delayed recovery of axons with different sizes. For the representative data, we have identified the thresholds for partial and full inhibition:

Partial inhibition: Radiant exposure 0.013 J/cm^2 Average power 46.0 mW

Full inhibition: Radiant exposure 0.018 J/cm^2 Average power 63.1 mW

For the prolonged inhibitory effect test, we tested the following parameters:

Prolonged inhibition: Radiant exposure 0.034 J/cm^2 Average power 119.6 mW

From the raw data shown in Figure A.17, we can see that the small-diameter axons showed a delayed recovery that is about 4 seconds after the recovery of the large-diameter axons. The normalized rectified area under the curve also confirmed the observation, see Figure A.18.

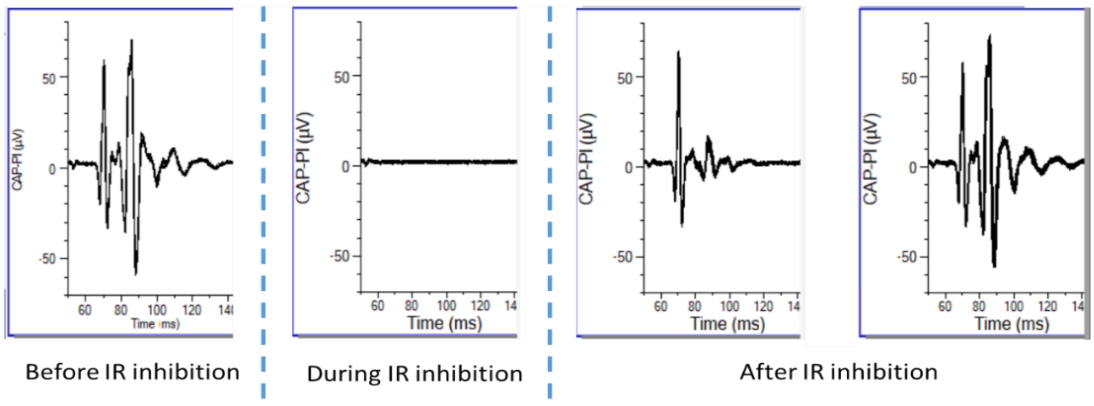

Figure A.17. Raw compound action potential recordings of prolonged inhibition of small-diameter axons.

The panels from left to right show the raw CAP signals before, during, and after the IR application. When the IR was applied, the CAP was fully inhibited.

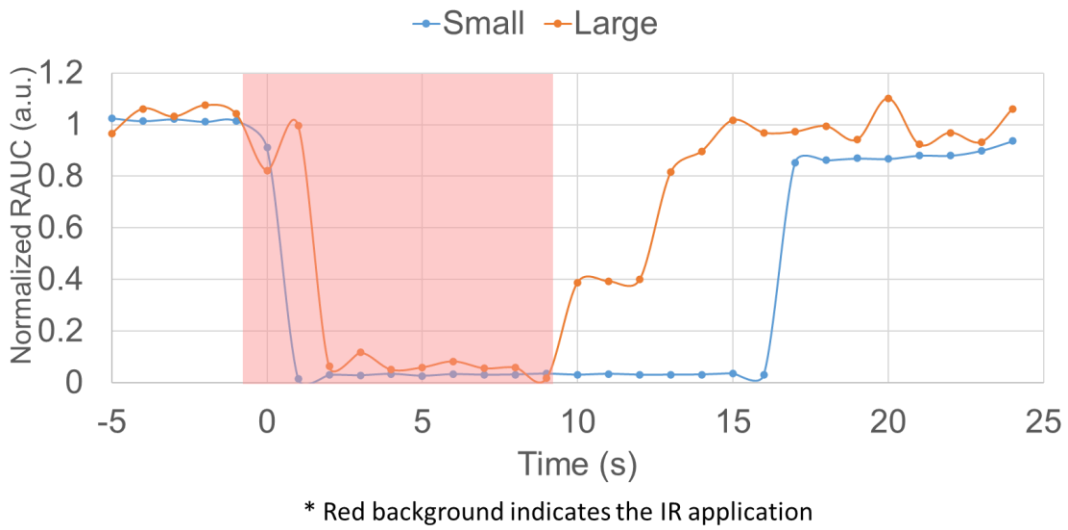

Figure A.18. The normalized RAUC showed that the small-diameter axons recovered 3 seconds after the recovery of large-diameter axons.

The normalized RAUC was calculated for the response of small- and large-diameter axons respectively. The light red background indicates the IR application period. We can see that the response from large-diameter axons recovered faster than the small-diameter axons when the laser was turned off.

Appendix B. Fabrication protocol for a spiral heating cuff

B.1 Twist two heating wires

- Twist two heating wires together to make a twisted heating wire bundle.
- The twisted wire bundle will be used as the basic heating element in the following steps.
- Wrap the heating wire around a small piece of paper tape to make holding points of the heating wire.
- Lay the two wires in parallel with about ½ inch gap, and tape one end of both wires down.
- Hand twisting the two wires together by loosely holding up the wires and making a clockwise rotation.
- Don't hold the wire by pinching. As the wires are rotating during the twisting process, pinching will limit the rotation and cause breakage of the wire
- One can make a long piece of the twisted heating wire bundle for future use.
    - The twisted wire bundle can be wrapped into a spool for storage

B.2 Wrapping the wire around the tube

- Make a very small stitch at one end of the inner tube with the suture wire.
    - Pull it through to close to the end; cut & save the remainder (including the needle) for later use.

- Get a small piece of the twisted heating wire; tape it at the ends.
- Tie a knot with the suture wire at the midpoint of the twisted heating wire.
    - Make a loose knot, then adjust & tape down the heating wire to stabilize, then tighten the suture knot.
- Release the heating wire from the table.
- Twist the 2 ends of twisted heating wires together.
    - Twist under tension to make the wire bundle stable.
    - The twisted length should be slightly longer (~1/8 inch longer) than the planned wrapping distance.
    - Wrapping distance can be calculated as:

$$\text{Wrapping Distance} = \text{k} \times \sqrt{\pi \times \left(\frac{OD}{2}\right)^2 + pitch^2}$$

Where k is the number of turns for the wrapping, OD is the outer diameter of the inner heating tube, and Pitch is the distance between adjacent wrapped wires.

- Wrap the twisted heating wire around the silicone tube 3x
    - Hold the heating wire steady at an angle & twist the tube towards you.
    - Try to keep a steady tension; ~2 mm pitch.
- Anchor the other side of the heating wire with a suture at the other end of the tube.
    - Make another small stitch going against/perpendicular to the heating wire.
    - Tie a suture knot around the heating wire.
- Adjust the heating wire turns with tweezers.

- Tie another knot to tighten the suture.

B.3 Connecting the heating wire with the regular wires

- Untwist the two ends of the twisted heating wire bundle.
    - Untwist the wire bundle part that is not wrapped around the inner tube.
- Scratch the insulative coating off the heating wire.
    - Not too close to the splitting point; ~5 mm away.
    - The scratch can be done with a surgical blade, a razor blade, or a sharp tweezer.
    - The wire should be put on a glass slide or other firm surface that can stand scratching.
    - No additional tension on the wire as the scratching is applying tension.
    - Once the scratch is done correctly, the shiny silver metal color of the bare heating wire will be exposed in contrast with the yellow insulated wire.
- Cut ~1 foot each of 36 AWG regular wire.
    - Peel off the silicone jacket (~1 inch) at one end.
    - Split the bare strands of wires into two halves.
    - Twist each half of the bare wire strands together.
- (Optional) Crimping the connection point.
    - Cut a 4 mm long crimping tube and slide it onto the regular wire.
    - Use a Dremel cutting disc to cut the tube.

    - Use a large plastic bag to collect the cut short piece of the tube so it does not fly away.
    - Wear an N95 face mask during the cutting process as metal debris can be a hazard. The large plastic bag also helps contain the debris.
    - Check under the microscope to examine/remove any debris at the crimping tube edge.
    - Slide it on the end with exposed bare wire stands.
    - First slide through the bare wire stands.
    - Then try to pull the silicone jacket through the crimping tube.
- Join the twisted heating wire end with regular wire.
    - Position one end of the twisted wire bundle pointing in parallel to one-half of the bare wire strands, in opposite direction.
    - Use the tape holding point to wrap the twisted heating wire end on the parallel half of the bare wire strands.
    - Bring the other half of the bare wire strands in parallel with the one wrapped with heating wire.
    - Use a tweezer to hold the bare wire strands and the heating wire together
        - 5 mm away from the anchored splitting point.
    - While holding the tweezer, use the other hand to rotate the regular wire and twist the two bare wire strands together, including the wrapped heating wire end.

- (Optional crimping) Crimping the twisted junction between the regular wire and heating wire end.
    - Slide the crimping tube over the twisted junction of wires.
    - Keep about 1 mm of jacket remain the crimping tube to help anchor the crimping tube.
    - Use a piler with a small tip for applying maximum force on the crimping tube.
    - Crimping the jacket end first, then the opposite end, and finally the middle region.
- Trim off wire ends that are not needed anymore
- Use a silicone heat shrink tube to insulate the junction between the heating wire and the regular wire.
    - Slide a piece of heat shrink tube over the junction region.
    - Use a hot air gun to shrink the tube.

B.4 Covering the cuff

- Get the outer tube ready to slide on.
    - Pull the suture threads through the outer tube.
- Mix silicone adhesive and apply it to the cuff.
- Slide the tube on, making sure to get rid of any air bubbles.
    - Make sure when sliding the bigger tube on, there is a good amount of silicone adhesive on the inner tube.

    - Add more silicone adhesive onto the inner tube while sliding the outer tube on.

- Heat (about 75 ℃) to speed up the curing process.
    - Cure time is based on the silicone adhesive’s specification.
- Make spiral cuts & trim off excess silicone
    - Stay in between adjacent heating wires for an even cut.

Appendix C. Considerations for the *ex vivo* electrophysiological test with *Aplysia* nerve

This appendix addresses the considerations for the dissection of the *Aplysia* pleural-abdominal connective nerve and conducting *ex vivo* electrophysiological tests. The test has been used in various experiments that use the evoked CAPs for assessing the status of neural conduction when applying a given neuromodulation modality [10,193,194]. The experimenter should plan ahead of time to determine if the unique *Aplysia* nerve, which consists of only unmyelinated axons with various diameters, is suitable for their research goal. The experimenter should also plan the endpoint measurement of the experiment ahead of time. At the exploration phase of the research, if possible, different experiment plans should be predetermined for both positive and negative experimental results to help examine the hypothesis thoroughly within a limited number of attempts to avoid variability between animals.

The *Aplysia* nerve can be tested acutely (within 2 hours) or in a prolonged test where the nerve is sustained for a much longer period (no longer than 24 hours) can be done. The type of experiment will affect the materials and configurations in the experimental setup. Overall, there are four steps involved in the testing process: 1) experimental setup configuration, 2) nerve dissection, 3) electrophysiological test, and 4) final cleaning up. In general, the experiment should be conducted as the steps mentioned. But there are tasks (e.g., temperature change and pumping fluid throughout the tubing) that can take a long time and should be planned ahead of time and run in parallel with other steps to save time.

The experimental setup of the test with *Aplysia* nerve includes surgical tools, *Aplysia* saline, and superfusion system, an electrophysiological test system, and the

supporting system that includes microscopes and lighting. They need to be prepared and maintained before conducting the experiments. Please refer to the owner's manual for related details. Here I will discuss several aspects that are specific to the experiment.

The surgical tools should be maintained correctly to keep the sharpness. When trying to make the initial incision on the *Aplysia* skin, a pair of sharp scissors can help accelerate the process. It is also critical to have a clean cut when transecting the nerve for achieving the optimal signal-to-noise (SNR) ratio in the following electrophysiological test. Sharp tools can increase the success rate of surgical operations; therefore, minimizing the manipulation of the nerve which can damage it. Since we are dealing with marine animals, it is critical to rinse the surgical tools with di-ionized water and dry them after use to slow down the rusting process.

Several properties of the *Aplysia* saline need to be maintained for the neural tissue to function normally in the *ex vivo* experimental setup. First is the temperature of the saline. It is recommended to remove the saline from the refrigerator and allow it to come to room temperature before using it in the experiment. Second is the pH level of the saline. All the saline was made to have a pH level between 7.2 to 7.4 initially. After storing in the fridge, the dissolvable CO_2 may escape from the solution due to a lowered solubility at a lower temperature. Also with a longer period of storing the saline in the fridge, bacteria can grow in the saline and generally lower the pH level. pH level is also affected by the temperature of saline. It is recommended to test the pH level before the experiment to make sure the saline's pH level is within the limit.

The structure of the saline circulation system is shown in Figure 3.1. There are several difficulties in keeping the circulation running correctly. The first is about configuring the flow rate of the two pump heads that are responsible for the liquid in-flow and out-flow of the nerve chamber. The chamber was designed so that the liquid output port is higher

than the liquid input port. By setting the out-flow rate to be slightly higher than the in-flow rate, it can be ensured that the liquid level remains within the height limit of the chamber. The absolute value of the flow rate should be limited so that the oscillation caused by the pneumatic pump head does not cause strong shaking of the nerve suspended in the saline. The second is to have the circulation up and running before dissecting the nerve out of the animal. The system can take 15 minutes or longer to circulate all air bubbles out of the tubing. The third is to clean up the circulation system after each experiment. The process includes: a) removing all saline from the circulation system; b) rinsing the circulation system with di-ionized water; c) removing all liquid from the circulation system. The b and c steps should be repeated if necessary. It is very time-consuming (about 30 mins to 1 hour) for the cleaning process, but it is necessary as leaving saline in the system can cause mold and bacteria to grow in the system.

For the electrophysiological test system, the main issue is to de-noise the system. Several aspects need to be paid attention to. First, the AC impedance at 1 kHz of the electrode can be used to indicate the status of the electrodes and related connections. An impedance of around 1 to 10 kΩ is typical for the suction electrodes used in the present study. A much higher impedance may indicate the electrode is strongly oxidized or there is a weakened point in the wire connection. A much lower impedance may indicate there is shunting in the circuit. Second, all the connected components in the electrophysiological system should be grounded to a single point. This includes the saline bath, the amplifier, the power line noise suppressor, the digitizer, and the Faraday cage. The output stage of the electrical stimulation current source should remain floating as grounding may cause a strong artifact in the recording. Third, the filter range of the amplifier should be configured to the minimal range that is wide enough to cover the spectrum of the desired signal. And

the digitizing frequency should be set to about 5-10 times higher than the upper bound of the signal range.

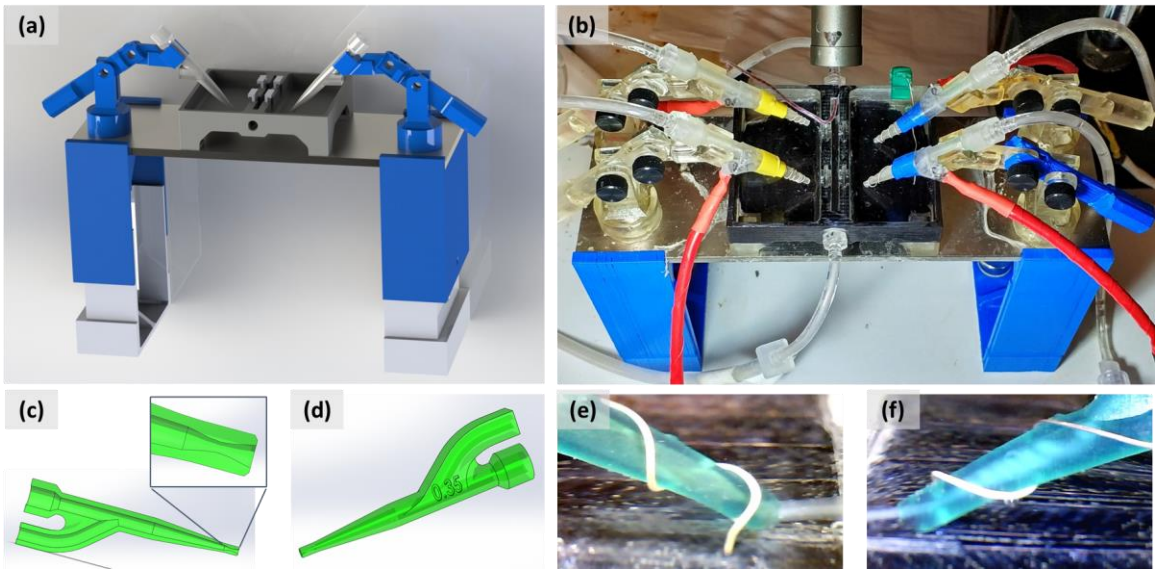

Figure C.1. The design of the experimental setup and the actual setup.

(a) This panel shows the experimental setup design. The suction electrodes are held by adjustable mini holders. The nerve chamber in the middle and the suction electrode holders are attached to the base plate by magnets. The base plate is mounted on a height-adjustable stand to allow the ergonomically comfortable operation of the experiment. (b) The actual experimental setup demonstrates the dual nerve testing configuration. Two independent stimulators are required for this configuration. (c) A cross-sectional view of the suction electrode design. The insert shows the bottleneck design at the suction electrode. (d) The overall geometry of the suction electrode. (e) and (f) The suction electrodes with nerves that have been suctioned into the electrodes.

Another critical aspect of the electrophysiological test is to synchronize with the device for the modality to be tested, such as the laser source for infrared neural inhibition. Generally, this can be done using the analog/digital output on the digitizer to send out a triggering signal toward the external device. I have developed a set of LabVIEW and Matlab software for this purpose, which can be found in the lab's code base. Here are some figures for the user interface:

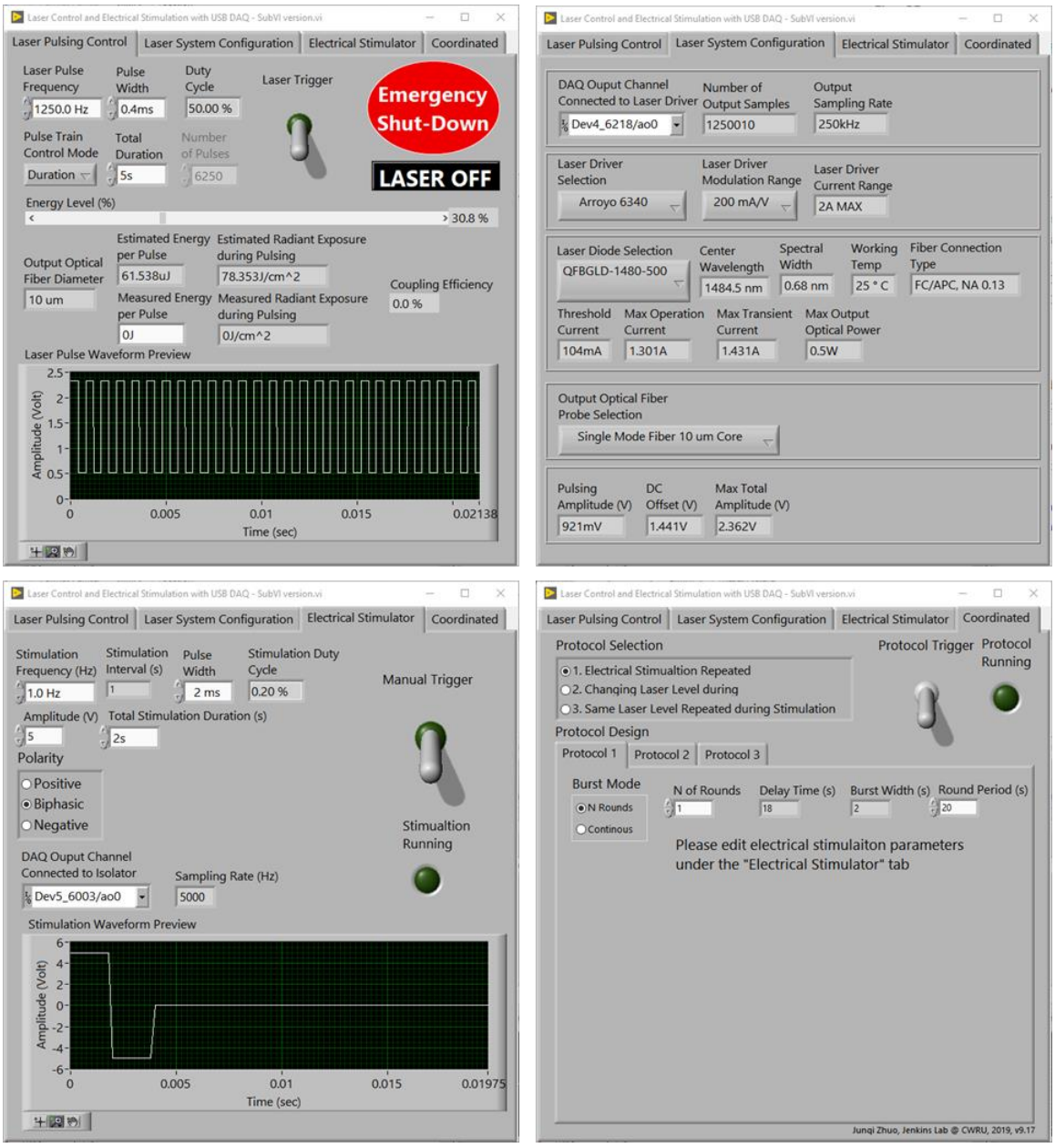

Figure C.2. The user interface of the LabVIEW software for the coordinated electrophysiological test with infrared laser application.

The panels in the top row are the control panel for the laser system. The panels in the bottom row are the control panel for the electrophysiological testing.

Appendix D. Protocol for sciatic nerve dissection and *ex vivo* electrophysiology test

This is the protocol for conducting the electrophysiological test on the sciatic nerve in an *ex-vivo* configuration. The test outcome is the change of the compound action potential (CAP) evoked by electrical stimulation. The CAPs are hypothesized to be inhibited by the application of photobiomodulation (PBM) using infrared light around 800 nm, especially on the small-diameter axons first. This protocol is adapted from the experimental procedures described in:

Bala, Usman, et al. "Harvesting the maximum length of the sciatic nerve from adult mice: a step-by-step approach." BMC research notes 7.1 (2014): 1-5.

Gonzalez, Sergio, et al. "*In vivo* introduction of transgenes into mouse sciatic nerve cells in situ using viral vectors." Nature protocols 9.5 (2014): 1160-1169.

D.1 Sciatic nerve dissection procedure for rat

1) Expose the animal to 4% isoflurane by inhalation until unconscious. Put the animal in a supine position, see Figure D.1a. Use 2.0 % isoflurane to maintain deep anesthesia. Apply eye lubrication to prevent the drying of the tear film. Toe pinch to ensure no response. Tape extremities to fix the animal's position.

2) Remove skin hairs using a trimmer and vacuum. Disinfect the skin with 70% ethanol. Make an incision along the line along the thigh using scissors and retract the skin to expose the splitting line between the gluteal muscle and femoral biceps muscle. Split the muscles along the line between two muscles to expose the sciatic nerve, see Figure D.1b.

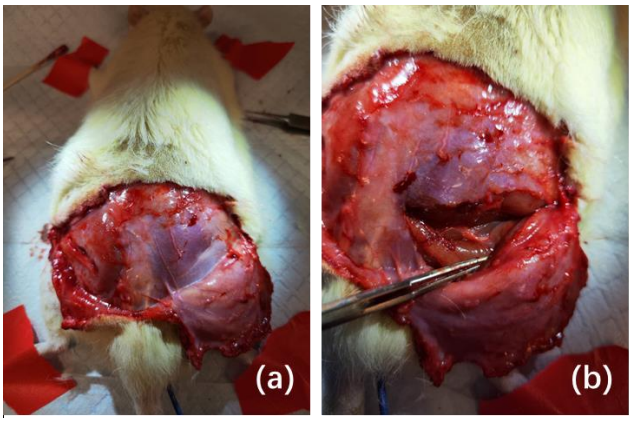

Figure D.1. The skin incision and separating of muscles for exposing the sciatic nerve at the thigh level.

(a*) The skin is retracted to show the splitting line between the gluteal muscle and femoral biceps muscle. (b) The muscles are separated to expose the sciatic nerve.*

3) Further, split the muscles to expose the sciatic nerve in the thigh region. If necessary, trim muscles at its tendon to provide access to the nerve and minimize bleeding.

4) Measure and record the lengths of the target nerve segment. This can be done either before or after the dissection. As the nerve can contract after the transaction, measuring length before the transaction is preferred. But drifting from the designated transecting location can happen and causes significant errors.

5) Gently lift the nerve using forceps (preferably only pinching on the connective tissue) and separate it from the surrounding tissue using sharp tweezer tips.

6) With minimum tension, transect the sciatic nerve. Cutting at the distal end first as the surrounding tissue is relatively more complex. The cut point of the distal end can be either before or after the branching point, depending on the experiment requirement. When cutting the proximal end closing to the pelvic bone, pay special attention to avoid cutting the common iliac artery and vein, which can

cause major bleeding. Adequate tension is needed for a clean cut. But it is preferred to keep tension minimum and avoid excessive tension.

7) Clear the nerve of the protective sheath and other connective tissues in the ice-cold saline bath. Avoid tugging, pulling, or poking the nerve.

8) The nerve should remain in the oxygenated cold saline for 1 h before the electrophysiological test.

D.2 Electrophysiology test preparation

1) Turn on the electrophysiology amplifier and stimulator to warm up the device.

2) Fill the reservoir bottle with synthetic interstitial fluid and turn on the pump of the superfusion system.

3) Put the reservoir bottle into the preheating water bath. Fill the water bath with an adequate level of water and turn it on. Set the temperature to 40 °C. Turn on the in-line heater to set the temperature in the chamber to 37 °C.

4) After the system has been running for a while (3min +), adjust the liquid level in the testing chamber to the maximum depth but not overflowing. Tap the tubes to move any gas out of the system.

5) Set the amplifier and electrical stimulator to the adequate configuration, and check all connections are correctly connected.

6) Turn on the recording software on the computer and set the hardware acquisition configurations (e.g., channel name, gain, terminal type).

7) Temporarily turn off the superfusion system to avoid the nerve being washed away. Move the nerve into the testing chamber.

8) Mount the nerve onto the suction electrodes: Aim the nerve end with the suction electrode tip. Apply suction force through the syringe to bring the nerve end into the suction electrode. Once both sides are sucked in, release the negative pressure using the 3-way valve.

9) Make sure the nerve, electrodes, and grounding wire are all immersed in the saline. Flush away visible bubbles on any of these objects. Make sure the nerve is not shaking vigorously because of the flow induced by the superfusion system.

10) Turn on the superfusion system again and check if everything is still immersed correctly during pumping.

11) Conduct an electrical stimulation test to verify if the system can stimulate the nerve and record the compound action potential response.

12) Adjust the electrical stimulation parameters (current level, pulse duration, pulse type) to ensure that all components of the compound action potential are evoked.

D.3 Laser system preparation

1) Check the wire connections: from the laser source port to the laser mount then to the laser diode, and from the TEC source port to the laser mount. Make sure the laser diode is correctly mounted on the laser mount.

2) Check the optical fiber probe's condition: there should be no obvious damage to the bare fiber tip and no obvious dirt on the SMA fiber connector. Clean the optical fiber probe if necessary. Use a visible light source to check the exit light pattern to be round and sharp.

3) Connect the SMA connector to the laser diode's pigtail fiber by the SMA-SMA connector. Use index-matching gel if necessary. Make sure the whole optical fiber

is secured and not bent beyond its minimum bending radius. Use tape to secure the optical fiber if necessary and also avoid obstruction to the operation of other devices.

4) Mount the bare fiber tip end of the optical fiber probe onto the micromanipulator. Put the power meter detector in the aim of the bare optical fiber tip. Allow sufficient distance (e.g., ½ inch or 10 mm, which should be calculated based on the optical fiber's NA and planned maximum optical power) so the power density is not beyond the detector's limit.

5) Wear the safety goggle with a correct optical density of the currently used wavelength. Turn on the laser-on sign. Check to make sure the opening of the working space is correctly blacked-out so no laser light can leak out.

6) Turn on the laser and TEC controller. Check and ensure the laser diode current level and the TEC set temperature is correctly configured. If necessary, check other parameters too.

7) Turn on the TEC output. Wait for the temperature to stabilize. Setting the TEC target temperature to be slightly lower than the room temperature can ensure the TEC system is actively working and only working in cooling mode.

8) Turn on the power meter and set the parameters (e.g., wavelength, power level, pulse width, threshold).

9) Turn on the laser diode current output, adjust the current level and record the corresponding optical power output measured by the power meter. Turn off the laser diode current output after the test.

10) Compare the data with previously measured laser performance to verify the laser system is operating correctly. It is normal to see a slight decay of the laser's output after repeated use.

11) According to the planned optical power level, calculate the corresponding laser diode current. If wanted, one can conduct the test with a calculated current level and adjust the number based on the measured power level.

12) Reposition and adjust the micromanipulator to allow enough travel distance for the probe tip to make contact with the nerve. To do that, one can put the micromanipulator to the mid-place of each axis, use the magnetic base to coarsely adjust the x-y position, and use the T mount of the horizontal beam to coarsely adjust the z position. This will allow maximum travel distance.

D.4 PBM test

1) Conduct an electrical stimulation test to establish the baseline response. Repeat the test several times to go through the initial run-down of the nerve's response. The test duration should be the same length as the planned electrical stimulation test during laser application. This is because the nerve's response can run-down within one round of the test, especially if it is long (>30 seconds).

2) Position the bare optical fiber tip to be perpendicular to the nerve see Figure D.2. Lower the optical fiber tip to make contact with the nerve. Back off the laser tip to achieve the desired illumination area size. See Figure D.2.

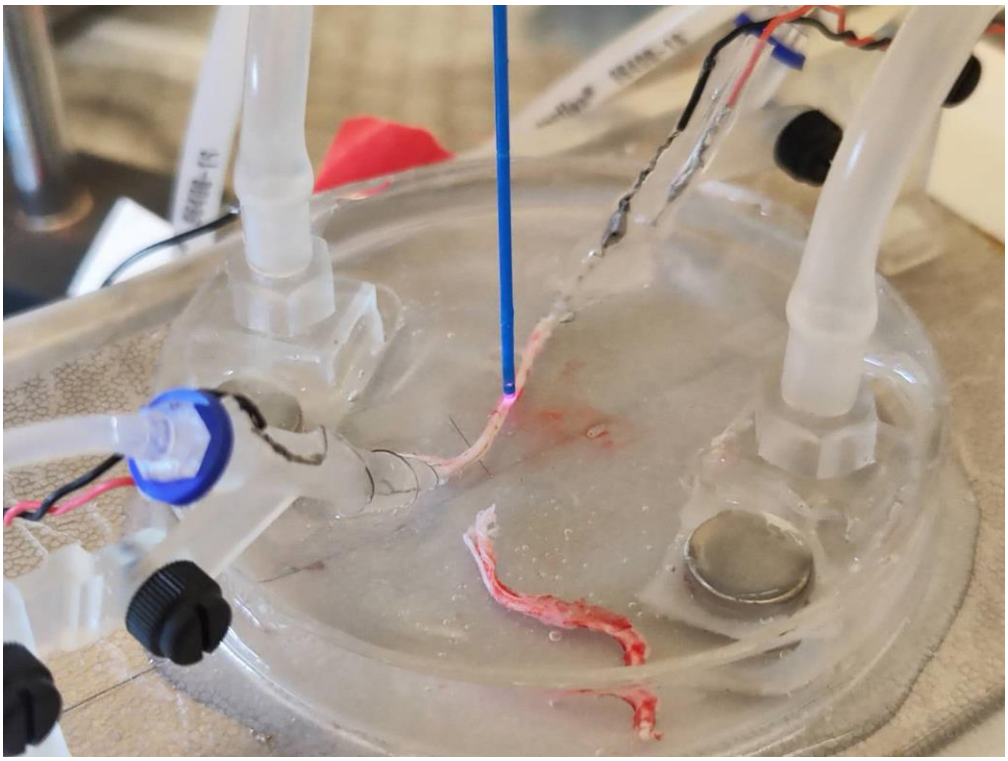

Figure D.2. Experimental setup of the PBM test.

The figure shows the experimental setup of the PBM test. The sciatic nerve was stimulated and recorded using suction electrodes. An optical fiber was positioned to be in contact with the nerve for the delivery of PBM light. The visible aiming beam was turned on to indicate the position of the optical fiber. The dish is mounted on a temperature-controlled plate for maintaining desired saline temperature. Two 3D-printed ports are connected to a circulation system for circulating the oxygenated saline solution.

3) Set the laser diode current to the desired value based on the planned optical power level. Turn on the laser diode current output for the planned duration. The electrical stimulation can be turned on simultaneously to examine the response during the laser application.

4) Turn off the laser diode current output after the planned duration. Double-check to make sure the laser diode is not left on accidentally.

5) The electrical stimulation test can be conducted after the laser application to examine the response after the laser is turned off.

6) Repeat steps 2 to 5 according to the experimental plan. It can be changing different IR parameters (e.g., illumination area, power level, duration of laser application) until an endpoint condition is met.

7) Allowing appropriate laser-off time between tests may be necessary since the laser's effect on the biology system may be accumulating. It will be wise to record the timestamp of each testing session.

8) Record all tested laser diode current levels for the optical power measurement later. Sometimes the tested laser diode current can be different from the planned numbers. So, a power measurement after the experiment with the tested number would be necessary to report the real laser dose applied to the tissue.

9) After conducting tests, move the optical fiber tip up and check for any protein clustering on the optical fiber tip. Re-conduct the laser output test as instructed in steps 4, 8-11 of Laser System Preparation.

10) Compare the results with the number acquired before the PBM test to determine if there was anything accumulated on the optical fiber tip during the test. If yes, clear the bare fiber tip with a clean tissue and isopropyl alcohol. Re-conduct the laser output test to see if the light output can be restored.

D.5 Cleaning up after experiments

1) Turn off the laser diode output. Turn off the TEC output. Remove the optical fiber from the set up and clean the optical fiber tip. Store the optical fiber.

2) Temporarily turn off the superfusion system. Using the syringe, apply positive pressure to push the nerve end out of the suction electrodes. Store or discard the nerve adequately.

3) Turn on the pump and drain the superfusion system.

4) Use the syringe to flush the inside of the suction electrode with DI water. Dry the suction electrode thoroughly.

5) Flush the superfusion system with DI water. Drain it and dry the system as much as possible.

6) Turn off other remaining devices (e.g., amplifiers, stimulators)

D.6 Potential hazards

1) Animal Handling Hazards (bite, scratch, etc.)

2) Biohazard with blood and internal tissues

3) Anesthesia (e.g., isoflurane, sevoflurane) hazard

4) Sharps Hazards (scalpels, needles, etc.)

5) Laser Hazards (unplanned reflection, accidentally left the laser on, etc.)

6) Electrical Shock Hazards (electrical shock)

7) Heat Hazards (get burned by hot water)

8) Mechanical Hazards by the superfusion pump

D.7 Troubleshooting

No recording from the electrophysiological test

1) Check to ensure the artifact is present in the recording. The artifact is the response that happens at the same time as the electrical stimulation. No delay is the key parameter of the artifact.

2) If the artifact is present but no CAP, this means the electrical stimulation is present and the electrodes and amplifier are working:

3) Check the electrical stimulation level, increase the level if necessary

4) Check to make sure the recording electrode is not sucking on the side of the nerve. Redo the suction if necessary

5) Check the filter configuration on the amplifier to make sure it is adequate.

6) If the artifact is not present in the recording: the electrical stimulation half of the electrophysiology system may not be working correctly. Check the connections and make sure there is an electrical stimulation output applied on the stimulation electrode when the nerve is connected.

7) If there is electrical stimulation applied but still no artifact or CAP, try touching the recording electrode during recording to see if there is a disruption presented. If not, this means the recording half of the electrophysiology system is not working correctly:

8) Check all the wire connections. Make sure all connections are correctly connected and water-free.

9) Check to make sure the amplifier is set to Rec mode, not STIM mode.

10) Check that the selected analog input channel in the recording software is correct.

11) Check that the gain and unit set in the recording software are correct.

No laser output from the bare optical fiber tip.

1) Check to make sure the optical fiber is connected to the pig-tail fiber of the laser diode.

2) Check to make sure the electrical connection from the laser diode driver port to the laser diode is correct.

3) Measure with a power meter to see if there is any output. Sometimes when the IR power is low, the IR card can not indicate the output correctly.

4) The IR card needs to be charged by visible light before responding to an IR input. If the card is being illuminated too long or stays in dark too long, it will not respond to IR illumination.

5) Use an IR card to check if there is light output from the pigtail fiber.

    a) If yes, this means the laser is working correctly. Then check to make sure there are no foreign objects in the SMA-SMA connector. Use a light source to check if the optical fiber probe is broken

    b) If not, this means the laser diode is not working or the pig-tail fiber is broken.

6) Check to make sure there is a voltage applied on the laser diode when the laser diode current output is enabled and no zero.

    a) If there is no laser output even with current passing through the laser diode, this means the laser diode is not working correctly. Send the laser diode back to the manufacturer for further examination and/or repair.

    b) If the laser diode passing through the laser diode does not match the display on the laser diode driver, this means the laser diode driver is not working correctly. Check for any wire disconnection with a multimeter first. If necessary, contact the manufacturer for technical support.

Bibliography

1. Basantsova NY, Starshinova AA, Dori A, Zinchenko YS, Yablonskiy PK, Shoenfeld Y. Small-fiber neuropathy definition, diagnosis, and treatment. *Neurol Sci*. 2019;40(7):1343-1350. doi:10.1007/s10072-019-03871-x

2. Horn CC, Ardell JL, Fisher LE. Electroceutical Targeting of the Autonomic Nervous System. *Physiology*. 2019;34(2):150-162. doi:10.1152/physiol.00030.2018

3. Themistocleous AC, Ramirez JD, Serra J, Bennett DLH. The clinical approach to small fibre neuropathy and painful channelopathy. *Pract Neurol*. 2014;14(6):368-379. doi:10.1136/practneurol-2013-000758

4. Papademetriou V, Doumas M, Tsioufis K. Renal sympathetic denervation for the treatment of difficult-to-control or resistant hypertension. *Int J Hypertens*. 2011;2011.

5. Sopacua M, Hoeijmakers JGJ, Merkies ISJ, Lauria G, Waxman SG, Faber CG. Small-fiber neuropathy: Expanding the clinical pain universe. *J Peripher Nerv Syst*. 2019;24(1):19-33. doi:10.1111/jns.12298

6. Jinesh S, Kullgren J, Shankar GS, Radhakrishnan R. Pharmaceutical perspective of neuropathic pain management for primary care providers. *Inflammopharmacology*. 2022;30(3):713-723. doi:10.1007/s10787-022-00963-7

7. McNicol E, Horowicz-Mehler N, Fisk RA, et al. Management of opioid side effects in cancer-related and chronic noncancer pain: a systematic review. *J Pain*. 2003;4(5):231-256. doi:10.1016/S1526-5900(03)00556-X

8. Lothet EH, Shaw KM, Lu H, et al. Selective inhibition of small-diameter axons using infrared light. *Sci Rep*. 2017;7(1):3275. doi:10.1038/s41598-017-03374-9

9. Ganguly M, Jenkins MW, Jansen ED, Chiel HJ. Thermal block of action potentials is primarily due to voltage-dependent potassium currents: a modeling study. *J Neural Eng*. 2019;16(3):036020. doi:10.1088/1741-2552/ab131b

10. Ganguly M, Ford JB, Zhuo J, et al. Voltage-gated potassium channels are critical for infrared inhibition of action potentials: an experimental study. *Neurophotonics*. 2019;6(4):040501. doi:10.1117/1.NPh.6.4.040501

11. Kandel ER, Koester JD, Mack SH, Siegelbaum SA. *Principles of Neural Science, Sixth Edition*. McGraw Hill Professional; 2021.

12. Hille B. Ionic Basis of Resting and Action Potentials. In: Terjung R, ed. *Comprehensive Physiology*. 1st ed. Wiley; 1977:99-136. doi:10.1002/cphy.cp010104

13. Cochet-Bissuel M, Lory P, Monteil A. The sodium leak channel, NALCN, in health and disease. *Front Cell Neurosci*. 2014;8. doi:10.3389/fncel.2014.00132

14. Enyedi P, Czirják G. Molecular Background of Leak K+ Currents: Two-Pore Domain Potassium Channels. *Physiol Rev*. 2010;90(2):559-605. doi:10.1152/physrev.00029.2009

15. Goldstein SAN, Bockenhauer D, O'Kelly I, Zilberberg N. Potassium leak channels and the KCNK family of two-p-domain subunits. *Nat Rev Neurosci*. 2001;2(3):175-184. doi:10.1038/35058574

16. Morth JP, Pedersen BP, Buch-Pedersen MJ, et al. A structural overview of the plasma membrane Na+,K+-ATPase and H+-ATPase ion pumps. *Nat Rev Mol Cell Biol*. 2011;12(1):60-70. doi:10.1038/nrm3031

17. Gadsby DC. Ion channels versus ion pumps: the principal difference, in principle. *Nat Rev Mol Cell Biol*. 2009;10(5):344-352. doi:10.1038/nrm2668

18. Spanswick RM. Electrogenic Ion Pumps. *Annu Rev Plant Physiol*. 1981;32(1):267-289. doi:10.1146/annurev.pp.32.060181.001411

19. Armstrong CM. The Na/K pump, Cl ion, and osmotic stabilization of cells. *Proc Natl Acad Sci*. 2003;100(10):6257-6262. doi:10.1073/pnas.0931278100

20. Terzis JK, Smith KL, Orgel MG. The Peripheral Nerve: Structure, Function, Reconstruction. *Plast Reconstr Surg*. 1991;87(6):1138-1139.

21. Garbay B, Heape AM, Sargueil F, Cassagne C. Myelin synthesis in the peripheral nervous system. *Prog Neurobiol*. 2000;61(3):267-304. doi:10.1016/s0301-0082(99)00049-0

22. Huxley AF, Stämpfli R. Evidence for saltatory conduction in peripheral myelinated nerve fibres. *J Physiol*. 1949;108(3):315-339.

23. Reina MA, López A, De Andrés JA. [Adipose tissue within peripheral nerves. Study of the human sciatic nerve]. *Rev Esp Anestesiol Reanim*. 2002;49(8):397-402.

24. Gao Y, Weng C, Wang X. Changes in nerve microcirculation following peripheral nerve compression. *Neural Regen Res*. 2013;8(11):1041-1047. doi:10.3969/j.issn.1673-5374.2013.11.010

25. Rydevik B, Lundborg G, Bagge U. Effects of graded compression on intraneural blood flow: An in vivo study on rabbit tibial nerve. *J Hand Surg*. 1981;6(1):3-12. doi:10.1016/S0363-5023(81)80003-2

26. Naples GG, Mortimer JT, Scheiner A, Sweeney JD. A spiral nerve cuff electrode for peripheral nerve stimulation. *IEEE Trans Biomed Eng*. 1988;35(11):905-916.

27. Besson JM, Chaouch A. Peripheral and spinal mechanisms of nociception. *Physiol Rev*. 1987;67(1):67-186. doi:10.1152/physrev.1987.67.1.67

28. Gabella G. *Structure of the Autonomic Nervous System*. Springer Netherlands; 1976. doi:10.1007/978-94-009-5745-9

29. Phillips JK. Pathogenesis of hypertension in renal failure: role of the sympathetic nervous system and renal afferents. *Clin Exp Pharmacol Physiol*. 2005;32(5-6):415-418. doi:10.1111/j.1440-1681.2005.04204.x

30. Kishi T. Heart failure as an autonomic nervous system dysfunction. *J Cardiol*. 2012;59(2):117-122. doi:10.1016/j.jjcc.2011.12.006

31. Nickel FT, Seifert F, Lanz S, Maihöfner C. Mechanisms of neuropathic pain. *Eur Neuropsychopharmacol*. 2012;22(2):81-91. doi:10.1016/j.euroneuro.2011.05.005

32. Obata K, Yamanaka H, Kobayashi K, et al. Role of mitogen-activated protein kinase activation in injured and intact primary afferent neurons for mechanical and heat hypersensitivity after spinal nerve ligation. *J Neurosci*. 2004;24(45):10211-10222.

33. Keating C, Beyak M, Foley S, et al. Afferent hypersensitivity in a mouse model of post‐inflammatory gut dysfunction: role of altered serotonin metabolism. *J Physiol*. 2008;586(18):4517-4530.

34. Amir R, Argoff CE, Bennett GJ, et al. The Role of Sodium Channels in Chronic Inflammatory and Neuropathic Pain. *J Pain*. 2006;7(5, Supplement):S1-S29. doi:10.1016/j.jpain.2006.01.444

35. Lauria G, Ziegler D, Malik R, et al. The Role of Sodium Channels in Painful Diabetic and Idiopathic Neuropathy. *Curr Diab Rep*. 2014;14(10):538. doi:10.1007/s11892-014-0538-5

36. Devor M. Sodium Channels and Mechanisms of Neuropathic Pain. *J Pain*. 2006;7(1, Supplement):S3-S12. doi:10.1016/j.jpain.2005.09.006

37. Mendell LM. Physiological properties of unmyelinated fiber projection to the spinal cord. *Exp Neurol*. 1966;16(3):316-332. doi:10.1016/0014-4886(66)90068-9

38. Li J, Simone DA, Larson AA. Windup leads to characteristics of central sensitization. *Pain*. 1999;79(1):75-82. doi:10.1016/S0304-3959(98)00154-7

39. Baron R, Binder A, Wasner G. Neuropathic pain: diagnosis, pathophysiological mechanisms, and treatment. *Lancet Neurol*. 2010;9(8):807-819.

40. Devor M, Amir R, Rappaport ZH. Pathophysiology of trigeminal neuralgia: the ignition hypothesis. *Clin J Pain*. 2002;18(1):4-13.

41. Van Hecke O, Austin SK, Khan RA, Smith BH, Torrance N. Neuropathic pain in the general population: a systematic review of epidemiological studies. *PAIN*®. 2014;155(4):654-662.

42. Bouhassira D, Lantéri-Minet M, Attal N, Laurent B, Touboul C. Prevalence of chronic pain with neuropathic characteristics in the general population. *Pain*. 2008;136(3):380-387.

43. Colloca L, Ludman T, Bouhassira D, et al. Neuropathic pain. *Nat Rev Dis Primer*. 2017;3(1):1-19. doi:10.1038/nrdp.2017.2

44. Haanpää ML, Treede RD. Diagnosis and classification of neuropathic pain. *Pain Clin Update*. 2010;18(7):1-6.

45. Schaefer C, Sadosky A, Mann R, et al. Pain severity and the economic burden of neuropathic pain in the United States: BEAT Neuropathic Pain Observational Study. *Clin Outcomes Res CEOR*. 2014;6:483-496. doi:10.2147/CEOR.S63323

46. Dworkin RH, Malone DC, Panarites CJ, Armstrong EP, Pham SV. Impact of postherpetic neuralgia and painful diabetic peripheral neuropathy on health care costs. *J Pain*. 2010;11(4):360-368.

47. DiBonaventura M daCosta, Cappelleri JC, Joshi AV. Association between Pain Severity and Health Care Resource Use, Health Status, Productivity and Related Costs in Painful Diabetic Peripheral Neuropathy Patients. *Pain Med*. 2011;12(5):799-807. doi:10.1111/j.1526-4637.2011.01103.x

48. Yong RJ, Mullins PM, Bhattacharyya N. Prevalence of chronic pain among adults in the United States. *PAIN*. 2022;163(2):e328. doi:10.1097/j.pain.0000000000002291

49. Ziegler D. Painful diabetic neuropathy: treatment and future aspects. *Diabetes Metab Res Rev*. 2008;24 Suppl 1:S52-7. doi:10.1002/dmrr.817

50. Gutierrez-Gutierrez G, Sereno M, Miralles A, Casado-Saenz E, Gutierrez-Rivas E. Chemotherapy-induced peripheral neuropathy: clinical features, diagnosis, prevention and treatment strategies. *Clin Transl Oncol*. 2010;12(2):81-91. doi:10.1007/S12094-010-0474-z

51. Yilmaz-Rastoder E, Gold MS, Hough KA, Gebhart GF, Williams BA. Effect of Adjuvant Drugs on the Action of Local Anesthetics in Isolated Rat Sciatic Nerves. *Reg Anesth Pain Med*. 2012;37(4):403-409. doi:10.1097/AAP.0b013e3182485965

52. Gerner P, Binshtok AM, Wang CF, et al. Capsaicin Combined with Local Anesthetics Preferentially Prolongs Sensory/Nociceptive Block in Rat Sciatic Nerve. *Anesthesiol J Am Soc Anesthesiol*. 2008;109(5):872-878. doi:10.1097/ALN.0b013e31818958f7

53. Moore PA, Hersh EV. Local Anesthetics: Pharmacology and Toxicity. *Dent Clin North Am*. 2010;54(4):587-599. doi:10.1016/j.cden.2010.06.015

54. Chou R, Turner JA, Devine EB, et al. The effectiveness and risks of long-term opioid therapy for chronic pain: a systematic review for a National Institutes of Health Pathways to Prevention Workshop. *Ann Intern Med*. 2015;162(4):276-286. doi:10.7326/M14-2559

55. Morrone L, Scuteri D, Rombola L, Mizoguchi H, Bagetta G. Opioids Resistance in Chronic Pain Management. *Curr Neuropharmacol*. 2017;15(3):444-456. doi:10.2174/1570159X14666161101092822

56. Vadivelu N, Kai AM, Kodumudi V, Sramcik J, Kaye AD. The Opioid Crisis: a Comprehensive Overview. *Curr Pain Headache Rep*. 2018;22(3):16. doi:10.1007/s11916-018-0670-z

57. Khan GM, Chen SR, Pan HL. Role of primary afferent nerves in allodynia caused by diabetic neuropathy in rats. *Neuroscience*. 2002;114(2):291-299.

58. Campese VM, Kogosov E. Renal afferent denervation prevents hypertension in rats with chronic renal failure. *Hypertension*. 1995;25(4):878-882.

59. Khan M, Nishi SE, Hassan SN, Islam MdA, Gan SH. Trigeminal Neuralgia, Glossopharyngeal Neuralgia, and Myofascial Pain Dysfunction Syndrome: An Update. *Pain Res Manag*. 2017;2017:7438326. doi:10.1155/2017/7438326

60. Webster G, Monge MC. Left Cardiac Sympathetic Denervation: Should We Sweat the Side Effects? *Circ Arrhythm Electrophysiol*. 2015;8(5):1007-1009. doi:10.1161/CIRCEP.115.003413

61. Dhople AA, Adams JR, Maggio WW, Naqvi SA, Regine WF, Kwok Y. Long-term outcomes of Gamma Knife radiosurgery for classic trigeminal neuralgia: implications of treatment and critical review of the literature: Clinical article. *J Neurosurg*. 2009;111(2):351-358. doi:10.3171/2009.2.JNS08977

62. Henschke N, Kuijpers T, Rubinstein SM, et al. Injection therapy and denervation procedures for chronic low-back pain: a systematic review. *Eur Spine J*. 2010;19(9):1425-1449. doi:10.1007/s00586-010-1411-0

63. Maas ET, Ostelo RW, Niemisto L, et al. Radiofrequency denervation for chronic low back pain. *Cochrane Database Syst Rev*. 2015;(10). doi:10.1002/14651858.CD008572.pub2

64. Larsen A, Piepgras D, Chyatte D, Rizzolo D. Trigeminal neuralgia: Diagnosis and medical and surgical management. *JAAPA*. 2011;24(7):20.

65. Rozen TD. Trigeminal neuralgia and glossopharyngeal neuralgia. *Neurol Clin*. 2004;22(1):185-206. doi:10.1016/S0733-8619(03)00094-X

66. Wang D, Wu Y, Chen Y, et al. Focal selective chemo-ablation of spinal cardiac afferent nerve by resiniferatoxin protects the heart from pressure overload-induced hypertrophy. *Biomed Pharmacother*. 2019;109:377-385. doi:10.1016/j.biopha.2018.10.156

67. Waddell-Smith KE, Ertresvaag KN, Li J, et al. Physical and Psychological Consequences of Left Cardiac Sympathetic Denervation in Long-QT Syndrome and Catecholaminergic Polymorphic Ventricular Tachycardia. *Circ Arrhythm Electrophysiol*. 2015;8(5):1151-1158. doi:10.1161/CIRCEP.115.003159

68. Niemz MH. Introduction. In: Niemz MH, ed. *Laser-Tissue Interactions: Fundamentals and Applications*. Biological and Medical Physics, Biomedical Engineering. Springer; 2007:1-8. doi:10.1007/978-3-540-72192-5_1

69. Palmer KF, Williams D. Optical properties of water in the near infrared*. *JOSA*. 1974;64(8):1107-1110. doi:10.1364/JOSA.64.001107

70. Quirk BJ, Whelan HT. Effect of Red-to-Near Infrared Light on the Reaction of Isolated Cytochrome c Oxidase with Cytochrome c. *Photomed Laser Surg*. 2016;34(12):631-637. doi:10.1089/pho.2015.4042

71. Sommer AP. Mitochondrial cytochrome c oxidase is not the primary acceptor for near infrared light—it is mitochondrial bound water: the principles of low-level light therapy. *Ann Transl Med*. 2019;7(Suppl 1). doi:10.21037/atm.2019.01.43

72. Cheong WF, Prahl SA, Welch AJ. A review of the optical properties of biological tissues. *IEEE J Quantum Electron*. 1990;26(12):2166-2185. doi:10.1109/3.64354

73. Jacques SL. Optical properties of biological tissues: a review. *Phys Med Biol*. 2013;58(11):R37-R61. doi:10.1088/0031-9155/58/11/R37

74. Bevilacqua F, Piguet D, Marquet P, Gross JD, Tromberg BJ, Depeursinge C. In vivo local determination of tissue optical properties: applications to human brain. *Appl Opt*. 1999;38(22):4939-4950. doi:10.1364/ao.38.004939

75. Dunn AK. Optical Properties of Neural Tissue. In: *Optical Imaging of Neocortical Dynamics*. Springer; 2014:33-51.

76. Welch AJ, Yoon G, Van Gemert MJC. Practical models for light distribution in laser-irradiated tissue. *Lasers Surg Med*. 1987;6(6):488-493. doi:10.1002/lsm.1900060603

77. Wang LV, Wu HI. *Biomedical Optics: Principles and Imaging*. John Wiley & Sons, Inc.; 2009. doi:10.1002/9780470177013

78. Wisotzky EL, Uecker FC, Dommerich S, Hilsmann A, Eisert P, Arens P. Determination of optical properties of human tissues obtained from parotidectomy in the spectral range of 250 to 800 nm. *J Biomed Opt*. 2019;24(12). doi:10.1117/1.JBO.24.12.125001

79. Zee P van der, Essenpreis M, Delpy DT. Optical properties of brain tissue. In: *Photon Migration and Imaging in Random Media and Tissues*. Vol 1888. International Society for Optics and Photonics; 1993:454-465. doi:10.1117/12.154665

80. Fang Q, Yan S. Graphics processing unit-accelerated mesh-based Monte Carlo photon transport simulations. *J Biomed Opt*. 2019;24(11):115002. doi:10.1117/1.JBO.24.11.115002

81. Fang Q, Boas DA. Monte Carlo simulation of photon migration in 3D turbid media accelerated by graphics processing units. *Opt Express*. 2009;17(22):20178-20190.

82. Wang L, Jacques SL, Zheng L. MCML—Monte Carlo modeling of light transport in multi-layered tissues. *Comput Methods Programs Biomed*. 1995;47(2):131-146. doi:10.1016/0169-2607(95)01640-F

83. Fang Q. Mesh-based Monte Carlo method using fast ray-tracing in Plücker coordinates. *Biomed Opt Express*. 2010;1(1):165-175. doi:10.1364/BOE.1.000165

84. Fang Q, Kaeli DR. Accelerating mesh-based Monte Carlo method on modern CPU architectures. *Biomed Opt Express*. 2012;3(12):3223-3230. doi:10.1364/BOE.3.003223

85. Yao R, Intes X, Fang Q. Generalized mesh-based Monte Carlo for wide-field illumination and detection via mesh retessellation. *Biomed Opt Express*. 2016;7(1):171-184. doi:10.1364/BOE.7.000171

86. Ansari MA, Erfanzadeh M, Mohajerani E. Mechanisms of Laser-Tissue Interaction: II. Tissue Thermal Properties. *J Lasers Med Sci*. 2013;4(3):99-106.

87. Arridge SR. Optical tomography in medical imaging. *Inverse Probl*. 1999;15(2):R41. doi:10.1088/0266-5611/15/2/022

88. Welch AJ, van Gemert MJC, eds. *Optical-Thermal Response of Laser-Irradiated Tissue*. Springer Netherlands; 2011. doi:10.1007/978-90-481-8831-4

89. Lozano AM, Lipsman N, Bergman H, et al. Deep brain stimulation: current challenges and future directions. *Nat Rev Neurol*. 2019;15(3):148-160. doi:10.1038/s41582-018-0128-2

90. Verrills P, Sinclair C, Barnard A. A review of spinal cord stimulation systems for chronic pain. *J Pain Res*. 2016;9:481-492. doi:10.2147/JPR.S108884

91. Johnson RL, Wilson CG. A review of vagus nerve stimulation as a therapeutic intervention. *J Inflamm Res*. 2018;11:203-213. doi:10.2147/JIR.S163248

92. Kent AR, Grill WM. Model-based analysis and design of nerve cuff electrodes for restoring bladder function by selective stimulation of the pudendal nerve. *J Neural Eng*. 2013;10(3):036010.

93. Mouraux A, Iannetti GD, Plaghki L. Low intensity intra-epidermal electrical stimulation can activate Aδ-nociceptors selectively. *Pain*. 2010;150(1):199-207.

94. Bhadra N, Kilgore KL. Direct current electrical conduction block of peripheral nerve. *IEEE Trans Neural Syst Rehabil Eng*. 2004;12(3):313-324.

95. Bhadra N, Kilgore KL. High-frequency electrical conduction block of mammalian peripheral motor nerve. *Muscle Nerve*. 2005;32(6):782-790. doi:10.1002/mus.20428

96. Rattay F. Analysis of Models for External Stimulation of Axons. *IEEE Trans Biomed Eng*. 1986;BME-33(10):974-977. doi:10.1109/TBME.1986.325670

97. Tai C, Roppolo JR, de Groat WC. Analysis of nerve conduction block induced by direct current. *J Comput Neurosci*. 2009;27(2):201-210. doi:10.1007/s10827-009-0137-7

98. Tan DW, Schiefer MA, Keith MW, Anderson JR, Tyler DJ. Stability and selectivity of a chronic, multi-contact cuff electrode for sensory stimulation in human amputees. *J Neural Eng*. 2015;12(2):026002. doi:10.1088/1741-2560/12/2/026002

99. Rozman J, Sovinec B, Trlep M, Zorko B. Multielectrode spiral cuff for ordered and reversed activation of nerve fibres. *J Biomed Eng*. 1993;15(2):113-120. doi:10.1016/0141-5425(93)90039-2

100. Lertmanorat Z, Durand DM. A novel electrode array for diameter-dependent control of axonal excitability: a Simulation study. *IEEE Trans Biomed Eng*. 2004;51(7):1242-1250. doi:10.1109/TBME.2004.827347

101. Koga K, Furue H, Rashid MH, Takaki A, Katafuchi T, Yoshimura M. Selective activation of primary afferent fibers evaluated by sine-wave electrical stimulation. *Mol Pain*. 2005;1(1):13. doi:10.1186/1744-8069-1-13

102. Patel YA, Butera RJ. Differential fiber-specific block of nerve conduction in mammalian peripheral nerves using kilohertz electrical stimulation. *J Neurophysiol*. 2015;113(10):3923-3929. doi:10.1152/jn.00529.2014

103. Joseph L, Butera RJ. High-Frequency Stimulation Selectively Blocks Different Types of Fibers in Frog Sciatic Nerve. *IEEE Trans Neural Syst Rehabil Eng*. 2011;19(5):550-557. doi:10.1109/TNSRE.2011.2163082

104. Rutten WLC. Selective Electrical Interfaces with the Nervous System. *Annu Rev Biomed Eng*. 2002;4(1):407-452. doi:10.1146/annurev.bioeng.4.020702.153427

105. Joseph L, Butera RJ. Unmyelinated Aplysia nerves exhibit a nonmonotonic blocking response to high-frequency stimulation. *IEEE Trans Neural Syst Rehabil Eng Publ IEEE Eng Med Biol Soc*. 2009;17(6):537-544. doi:10.1109/TNSRE.2009.2029490

106. Onuki Y, Bhardwaj U, Papadimitrakopoulos F, Burgess DJ. A Review of the Biocompatibility of Implantable Devices: Current Challenges to Overcome Foreign Body Response. *J Diabetes Sci Technol*. 2008;2(6):1003-1015. doi:10.1177/193229680800200610

107. Patel YA, Butera RJ. Challenges associated with nerve conduction block using kilohertz electrical stimulation. *J Neural Eng*. 2018;15(3):031002. doi:10.1088/1741-2552/aaadc0

108. Deer TR, Mekhail N, Provenzano D, et al. The Appropriate Use of Neurostimulation: Avoidance and Treatment of Complications of Neurostimulation Therapies for the Treatment of Chronic Pain. *Neuromodulation Technol Neural Interface*. 2014;17(6):571-598. doi:10.1111/ner.12206

109. Poitras S, Brosseau L. Evidence-informed management of chronic low back pain with transcutaneous electrical nerve stimulation, interferential current, electrical muscle stimulation, ultrasound, and thermotherapy. *Spine J*. 2008;8(1):226-233. doi:10.1016/j.spinee.2007.10.022

110. Gabriel RA, Ilfeld BM. Peripheral nerve blocks for postoperative analgesia: From traditional unencapsulated local anesthetic to liposomes, cryoneurolysis and peripheral nerve stimulation. *Best Pract Res Clin Anaesthesiol*. 2019;33(3):293-302. doi:10.1016/j.bpa.2019.06.002

111. Hodgkin AL, Katz B. The effect of temperature on the electrical activity of the giant axon of the squid. *J Physiol*. 1949;109(1-2):240-249.

112. Fishman MA, Scherer AM, Katsarakes AM, Larson L, Kim PS. Temperature-Mediated Nerve Blocks in the Treatment of Pain. *Curr Pain Headache Rep*. 2021;25(9):60. doi:10.1007/s11916-021-00978-9

113. Shin HJ, Kim SH, Hahm SC, Cho HY. Thermotherapy Plus Neck Stabilization Exercise for Chronic Nonspecific Neck Pain in Elderly: A Single-Blinded Randomized Controlled Trial. *Int J Environ Res Public Health*. 2020;17(15):5572. doi:10.3390/ijerph17155572

114. Dehghan M, Farahbod F. The Efficacy of Thermotherapy and Cryotherapy on Pain Relief in Patients with Acute Low Back Pain, A Clinical Trial Study. *J Clin Diagn Res JCDR*. 2014;8(9):LC01-LC04. doi:10.7860/JCDR/2014/7404.4818

115. Okada K, Oshima M, Kawakit K. Examination of the afferent fiber responsible for the suppression of jaw-opening reflex in heat, cold, and manual acupuncture stimulation in rats. *Brain Res*. 1996;740(1):201-207. doi:10.1016/S0006-8993(96)00863-3

116. Mtibaa K, Thomson A, Nichols D, Hautier C, Racinais S. Hyperthermia-induced Neural Alterations Impair Proprioception and Balance. *Med Sci Sports Exerc*. 2018;50(1):46-53. doi:10.1249/MSS.0000000000001418

117. Dubois M, Coppola R, Buchsbaum MS, Lees DE. Somatosensory evoked potentials during whole body hyperthermia in humans. *Electroencephalogr Clin Neurophysiol*. 1981;52(2):157-162. doi:10.1016/0013-4694(81)90163-2

118. Wondergem J, Haveman J, Rusman V, Sminia P, Van Dijk JDP. Effects of Local Hyperthermia on the Motor Function of the Rat Sciatic Nerve. *Int J Radiat Biol*. 1988;53(3):429-438. doi:10.1080/09553008814552561

119. De Vrind HH, Wondergem J, Haveman J. Hyperthermia-induced damage to rat sciatic nerve assessed in vivo with functional methods and with electrophysiology. *J Neurosci Methods*. 1992;45(3):165-174. doi:10.1016/0165-0270(92)90073-M

120. Zhang Z, Lyon TD, Kadow BT, et al. Conduction block of mammalian myelinated nerve by local cooling to 15–30°C after a brief heating. *J Neurophysiol*. 2016;115(3):1436-1445. doi:10.1152/jn.00954.2015

121. Franssen H, Wieneke GH, Wokke JHJ. The influence of temperature on conduction block. *Muscle Nerve*. 1999;22(2):166-173. doi:10.1002/(SICI)1097-4598(199902)22:2<166::AID-MUS4>3.0.CO;2-Q

122. Nadler SF, Weingand K, Kruse RJ. The physiologic basis and clinical applications of cryotherapy and thermotherapy for the pain practitioner. *Pain Physician*. 2004;7(3):395-399.

123. Morgan T, Zhang Y, Pace N, et al. Thermal block of mammalian unmyelinated C fibers by local cooling to 15-25°C after a brief heating at 45°C. *J Neurophysiol*. 2020;123(6):2173-2179. doi:10.1152/jn.00133.2020

124. Wang J, Shen B, Roppolo JR, de Groat WC, Tai C. Influence of frequency and temperature on the mechanisms of nerve conduction block induced by high-frequency biphasic electrical current. *J Comput Neurosci*. 2008;24(2):195-206. doi:10.1007/s10827-007-0050-x

125. Tai C, Wang J, Chancellor MB, Roppolo JR, de Groat WC. Influence of Temperature on Pudendal Nerve Block Induced by High-Frequency Biphasic Electrical Current. *J Urol*. 2008;180(3):1173-1178. doi:10.1016/j.juro.2008.04.138

126. Chen J, Zhong Y, Wang J, et al. Temperature Effect on Nerve Conduction Block Induced by High-Frequency (kHz) Biphasic Stimulation. *Neuromodulation Technol Neural Interface*. Published online January 3, 2022. doi:10.1016/j.neurom.2021.10.017

127. Tai C, Wang J, Roppolo JR, de Groat WC. Relationship between temperature and stimulation frequency in conduction block of amphibian myelinated axon. *J Comput Neurosci*. 2009;26(3):331-338. doi:10.1007/s10827-008-0115-5

128. Elwassif MM, Kong Q, Vazquez M, Bikson M. Bio-Heat Transfer Model of Deep Brain Stimulation Induced Temperature changes. In: *2006 International Conference of the IEEE Engineering in Medicine and Biology Society*. ; 2006:3580-3583. doi:10.1109/IEMBS.2006.259425

129. Zannou AL, Khadka N, Truong DQ, et al. Temperature increases by kilohertz frequency spinal cord stimulation. *Brain Stimulat*. 2019;12(1):62-72. doi:10.1016/j.brs.2018.10.007

130. Khadka N, Harmsen IE, Lozano AM, Bikson M. Bio-Heat Model of Kilohertz-Frequency Deep Brain Stimulation Increases Brain Tissue Temperature. *Neuromodulation Technol Neural Interface*. 2020;23(4):489-495. doi:10.1111/ner.13120

131. Zannou AL, Khadka N, FallahRad M, Truong DQ, Kopell BH, Bikson M. Tissue Temperature Increases by a 10 kHz Spinal Cord Stimulation System: Phantom and Bioheat Model. *Neuromodulation Technol Neural Interface*. 2021;24(8):1327-1335. doi:10.1111/ner.12980

132. Constans C, Mateo P, Tanter M, Aubry JF. Potential impact of thermal effects during ultrasonic neurostimulation: retrospective numerical estimation of temperature elevation in seven rodent setups. *Phys Med Biol*. 2018;63(2):025003. doi:10.1088/1361-6560/aaa15c

133. Prieto ML, Firouzi K, Khuri-Yakub BT, Madison DV, Maduke M. Spike frequency–dependent inhibition and excitation of neural activity by high-frequency ultrasound. *J Gen Physiol*. 2020;152(11):e202012672. doi:10.1085/jgp.202012672

134. Guo H, Offutt SJ, Hamilton II M, et al. Ultrasound does not activate but can inhibit in vivo mammalian nerves across a wide range of parameters. *Sci Rep*. 2022;12(1):2182. doi:10.1038/s41598-022-05226-7

135. Abramson DI, Chu LSW, Tuck S Jr, Lee SW, Richardson G, Levin M. Effect of Tissue Temperatures and Blood Flow on Motor Nerve Conduction Velocity. *JAMA*. 1966;198(10):1082-1088. doi:10.1001/jama.1966.03110230098021

136. Letcher FS, Goldring S. The Effect of Radiofrequency Current and Heat on Peripheral Nerve Action Potential in the Cat. *J Neurosurg*. 1968;29(1):42-47. doi:10.3171/jns.1968.29.1.0042

137. Soloman M, Mekhail MN, Mekhail N. Radiofrequency treatment in chronic pain. *Expert Rev Neurother*. 2010;10(3):469-474. doi:10.1586/ern.09.153

138. Leggett LE, Soril LJ, Lorenzetti DL, et al. Radiofrequency Ablation for Chronic Low Back Pain: A Systematic Review of Randomized Controlled Trials. *Pain Res Manag*. 2014;19(5):e146-e153. doi:10.1155/2014/834369

139. Kapural L, Deering JP. A technological overview of cooled radiofrequency ablation and its effectiveness in the management of chronic knee pain. *Pain Manag*. 2020;10(3):133-140. doi:10.2217/pmt-2019-0066

140. Gennaro N, Sconfienza LM, Ambrogi F, Boveri S, Lanza E. Thermal ablation to relieve pain from metastatic bone disease: a systematic review. *Skeletal Radiol*. 2019;48(8):1161-1169. doi:10.1007/s00256-018-3140-0

141. Ilfeld BM, Preciado J, Trescot AM. Novel cryoneurolysis device for the treatment of sensory and motor peripheral nerves. *Expert Rev Med Devices*. 2016;13(8):713-725. doi:10.1080/17434440.2016.1204229

142. Graves CE, Moyer J, Zobel MJ, et al. Intraoperative intercostal nerve cryoablation During the Nuss procedure reduces length of stay and opioid requirement: A randomized clinical trial. *J Pediatr Surg*. 2019;54(11):2250-2256. doi:10.1016/j.jpedsurg.2019.02.057

143. Foss JD, Wainford RD, Engeland WC, Fink GD, Osborn JW. A novel method of selective ablation of afferent renal nerves by periaxonal application of capsaicin. *Am J Physiol Regul Integr Comp Physiol*. 2015;308(2):R112-22. doi:10.1152/ajpregu.00427.2014

144. Haveman J, Van Der Zee J, Wondergem J, Hoogeveen JF, Hulshof MCCM. Effects of hyperthermia on the peripheral nervous system: a review. *Int J Hyperthermia*. 2004;20(4):371-391. doi:10.1080/02656730310001637631

145. Hoogeveen JF, Troost D, van der Kracht AH, Wondergem J, Haveman J, Gonzalez Gonzalez D. Ultrastructural changes in the rat sciatic nerve after local hyperthermia. *Int J Hyperth Off J Eur Soc Hyperthermic Oncol North Am Hyperth Group*. 1993;9(5):723-730. doi:10.3109/02656739309032059

146. Chaudhry V, Glass JD, Griffin JW. Wallerian Degeneration in Peripheral Nerve Disease. *Neurol Clin*. 1992;10(3):613-627. doi:10.1016/S0733-8619(18)30200-7

147. White MG, Luca LE, Nonner D, et al. Cellular mechanisms of neuronal damage from hyperthermia. In: Sharma HS, ed. *Progress in Brain Research*. Vol 162.

Neurobiology of Hyperthermia. Elsevier; 2007:347-371. doi:10.1016/S0079-6123(06)62017-7

148. Burke S, Hanani M. The actions of hyperthermia on the autonomic nervous system: Central and peripheral mechanisms and clinical implications. *Auton Neurosci*. 2012;168(1):4-13. doi:10.1016/j.autneu.2012.02.003

149. Balaban P, Esenaliev R, Karu T, et al. He‐Ne laser irradiation of single identified neurons. *Lasers Surg Med*. 1992;12(3):329-337.

150. Mendez F, Penner R. Near-visible ultraviolet light induces a novel ubiquitous calcium-permeable cation current in mammalian cell lines. *J Physiol*. 1998;507(Pt 2):365-377. doi:10.1111/j.1469-7793.1998.365bt.x

151. Allègre G, Avrillier S, Albe-Fessard D. Stimulation in the rat of a nerve fiber bundle by a short UV pulse from an excimer laser. *Neurosci Lett*. 1994;180(2):261-264. doi:10.1016/0304-3940(94)90534-7

152. Karu T. Primary and secondary mechanisms of action of visible to near-IR radiation on cells. *J Photochem Photobiol B*. 1999;49(1):1-17.

153. Toya S, Motegi M, Inomata K, Ohshiro T, Maeda T. Report on a computer-randomized double blind clinical trial to determine the effectiveness of the GaAlAs (830 nm) diode laser for pain attenuation in selected pain groups. *Laser Ther*. 1994;6(3):143-148.

154. Walker J. Relief from chronic pain by low power laser irradiation. *Neurosci Lett*. 1983;43(2):339-344. doi:10.1016/0304-3940(83)90211-2

155. Avci P, Gupta A, Sadasivam M, et al. Low-level laser (light) therapy (LLLT) in skin: stimulating, healing, restoring. In: Vol 32. NIH Public Access; 2013:41.

156. de Almeida P, Lopes-Martins RÁB, De Marchi T, et al. Red (660 nm) and infrared (830 nm) low-level laser therapy in skeletal muscle fatigue in humans: what is better? *Lasers Med Sci*. 2012;27(2):453-458.

157. Iyer SM, Vesuna S, Ramakrishnan C, et al. Optogenetic and chemogenetic strategies for sustained inhibition of pain. *Sci Rep*. 2016;6(1):30570. doi:10.1038/srep30570

158. Daou I, Beaudry H, Ase AR, et al. Optogenetic Silencing of Nav1.8-Positive Afferents Alleviates Inflammatory and Neuropathic Pain. *eNeuro*. 2016;3(1):ENEURO.0140-15.2016. doi:10.1523/ENEURO.0140-15.2016

159. Samineni VK, Mickle AD, Yoon J, et al. Optogenetic silencing of nociceptive primary afferents reduces evoked and ongoing bladder pain. *Sci Rep*. 2017;7(1):15865. doi:10.1038/s41598-017-16129-3

160. Iyer SM, Montgomery KL, Towne C, et al. Virally mediated optogenetic excitation and inhibition of pain in freely moving nontransgenic mice. *Nat Biotechnol*. 2014;32(3):274-278.

161. Wells JD, Kao C, Jansen ED, Konrad PE, Mahadevan-Jansen A. Application of infrared light for in vivo neural stimulation. *J Biomed Opt*. 2005;10(6):064003.

162. Wells J, Kao C, Mariappan K, et al. Optical stimulation of neural tissue in vivo. *Opt Lett*. 2005;30(5):504-506. doi:10.1364/ol.30.000504

163. Cayce JM, Bouchard MB, Chernov MM, et al. Calcium imaging of infrared-stimulated activity in rodent brain. *Cell Calcium*. 2014;55(4):183-190. doi:10.1016/j.ceca.2014.01.004

164. Cayce JM, Friedman RM, Jansen ED, Mahavaden-Jansen A, Roe AW. Pulsed infrared light alters neural activity in rat somatosensory cortex in vivo. *Neuroimage*. 2011;57(1):155-166.

165. Cayce JM, Friedman RM, Chen G, Jansen ED, Mahadevan-Jansen A, Roe AW. Infrared neural stimulation of primary visual cortex in non-human primates. *NeuroImage*. 2014;84:181-190. doi:10.1016/j.neuroimage.2013.08.040

166. Horváth ÁC, Borbély S, Mihók F, Fürjes P, Barthó P, Fekete Z. Histological and electrophysiological evidence on the safe operation of a sharp-tip multimodal optrode during infrared neuromodulation of the rat cortex. *Sci Rep*. 2022;12(1):11434. doi:10.1038/s41598-022-15367-4

167. Shi S, Xu AG, Rui YY, et al. Infrared neural stimulation with 7T fMRI: A rapid in vivo method for mapping cortical connections of primate amygdala. *NeuroImage*. 2021;231:117818. doi:10.1016/j.neuroimage.2021.117818

168. Xu AG, Qian M, Tian F, et al. Focal infrared neural stimulation with high-field functional MRI: A rapid way to map mesoscale brain connectomes. *Sci Adv*. 2019;5(4):eaau7046. doi:10.1126/sciadv.aau7046

169. Jenkins MW, Duke AR, Gu S, et al. Optical pacing of the embryonic heart. *Nat Photonics*. 2010;4:623-626. doi:10.1038/nphoton.2010.166

170. Jenkins MW, Wang YT, Doughman YQ, Watanabe M, Cheng Y, Rollins AM. Optical pacing of the adult rabbit heart. *Biomed Opt Express*. 2013;4(9):1626-1635.

171. McPheeters MT, Wang YT, Werdich AA, Jenkins MW, Laurita KR. An infrared optical pacing system for screening cardiac electrophysiology in human cardiomyocytes. *PLoS One*. 2017;12(8):e0183761. doi:10.1371/journal.pone.0183761

172. Littlefield PD, Richter CP. Near-infrared stimulation of the auditory nerve: A decade of progress toward an optical cochlear implant. *Laryngoscope Investig Otolaryngol*. 2021;6(2):310-319. doi:10.1002/lio2.541

173. Izzo AD, Suh E, Pathria J, Jr JTW, Whitlon DS, Richter CP. Selectivity of neural stimulation in the auditory system: a comparison of optic and electric stimuli. *J Biomed Opt*. 2007;12(2):021008. doi:10.1117/1.2714296

174. Xu Y, Xia N, Lim M, et al. Multichannel optrodes for photonic stimulation. *Neurophotonics*. 2018;5(4):045002.

175. Littlefield PD, Richter CP. Near-infrared stimulation of the auditory nerve: A decade of progress toward an optical cochlear implant. *Laryngoscope Investig Otolaryngol*. 2021;6(2):310-319. doi:10.1002/lio2.541

176. Richter CP, Bayon R, Izzo AD, et al. Optical stimulation of auditory neurons: Effects of acute and chronic deafening. *Hear Res*. 2008;242(1):42-51. doi:10.1016/j.heares.2008.01.011

177. Rajguru SM, Matic AI, Robinson AM, et al. Optical cochlear implants: Evaluation of surgical approach and laser parameters in cats. *Hear Res*. 2010;269(1):102-111. doi:10.1016/j.heares.2010.06.021

178. Matic AI, Robinson AM, Young HK, et al. Behavioral and Electrophysiological Responses Evoked by Chronic Infrared Neural Stimulation of the Cochlea. *PLOS ONE*. 2013;8(3):e58189. doi:10.1371/journal.pone.0058189

179. Zhu X, Lin JW, Sander MY. Infrared block of Na+ and Ca2+ spikes in in crayfish neuromuscular junction. In: Vol 10866. International Society for Optics and Photonics; 2019:108660E.

180. Zhu X, Lin JW, Sander MY. Infrared inhibition impacts on locally initiated and propagating action potentials and the downstream synaptic transmission. *Neurophotonics*. 2020;7(4):045003. doi:10.1117/1.NPh.7.4.045003

181. Zhu X, Zhu X, Zhu X, et al. Single infrared light pulses induce excitatory and inhibitory neuromodulation. *Biomed Opt Express*. 2022;13(1):374-388. doi:10.1364/BOE.444577

182. Zhu X, Lin JW, Sander MY. Infrared inhibition and waveform modulation of action potentials in the crayfish motor axon. *Biomed Opt Express*. 2019;10(12):6580-6594. doi:10.1364/BOE.10.006580

183. Yoo S, Park JH, Nam Y. Single-Cell Photothermal Neuromodulation for Functional Mapping of Neural Networks. *ACS Nano*. 2019;13(1):544-551. doi:10.1021/acsnano.8b07277

184. Carvalho-de-Souza JL, Treger JS, Dang B, Kent SBH, Pepperberg DR, Bezanilla F. Photosensitivity of Neurons Enabled by Cell-Targeted Gold Nanoparticles. *Neuron*. 2015;86(1):207-217. doi:10.1016/j.neuron.2015.02.033

185. Rastogi SK, Garg R, Scopelliti MG, et al. Remote nongenetic optical modulation of neuronal activity using fuzzy graphene. *Proc Natl Acad Sci*. 2020;117(24):13339-13349. doi:10.1073/pnas.1919921117

186. Wu X, Jiang Y, Rommelfanger NJ, et al. Tether-free photothermal deep-brain stimulation in freely behaving mice via wide-field illumination in the near-infrared-II window. *Nat Biomed Eng*. 2022;6(6):754-770. doi:10.1038/s41551-022-00862-w

187. Yang C, Park S. Nanomaterials-assisted thermally induced neuromodulation. *Biomed Eng Lett*. 2021;11(3):163-170. doi:10.1007/s13534-021-00193-w

188. Duke AR, Lu H, Jenkins MW, Chiel HJ, Jansen ED. Spatial and temporal variability in response to hybrid electro-optical stimulation. *J Neural Eng*. 2012;9(3):036003. doi:10.1088/1741-2560/9/3/036003

189. Duke AR, Jenkins MW, Lu H, McManus JM, Chiel HJ, Jansen ED. Transient and selective suppression of neural activity with infrared light. *Sci Rep*. 2013;3:2600. doi:10.1038/srep02600

190. Jack JJB, Noble D, Tsien RW. *Electric Current Flow in Excitable Cells*. Clarendon Press; 1975.

191. Ford JB, Ganguly M, Poorman ME, et al. Identifying the Role of Block Length in Neural Heat Block to Reduce Temperatures During Infrared Neural Inhibition. *Lasers Surg Med*. 2020;52(3):259-275. doi:10.1002/lsm.23139

192. Ford JB, Ganguly M, Zhuo J, et al. Optimizing thermal block length during infrared neural inhibition to minimize temperature thresholds. *J Neural Eng*. 2021;18(5):056016. doi:10.1088/1741-2552/abf00d

193. Zhuo J, Ou Z, Zhang Y, et al. Isotonic ion replacement can lower the threshold for selective infrared neural inhibition. *Neurophotonics*. 2021;8(1):015005. doi:10.1117/1.NPh.8.1.015005

194. Zhuo J, Weidrick CE, Liu Y, et al. Selective IR inhibition can be reproduced by resistance heating. In: *Optogenetics and Optical Manipulation 2022*. Vol PC11947. SPIE; 2022:PC1194706. doi:10.1117/12.2610130

195. Frazier WT, Kandel ER, Kupfermann I, Waziri R, Coggeshall RE. Morphological and functional properties of identified neurons in the abdominal ganglion of aplysia californica. *J Neurophysiol*. 1967;30(6):1288-1351. doi:10.1152/jn.1967.30.6.1288

196. Kandel ER. *Cellular Basis of Behavior: An Introduction to Behavioral Neurobiology*. W.H. Freeman; 1976.

197. Shapiro E, Castellucci VF, Kandel ER. Presynaptic membrane potential affects transmitter release in an identified neuron in Aplysia by modulating the Ca2+ and K+ currents. *Proc Natl Acad Sci*. 1980;77(1):629-633. doi:10.1073/pnas.77.1.629

198. Connor JA, Kretz R, Shapiro E. Calcium levels measured in a presynaptic neurone of Aplysia under conditions that modulate transmitter release. *J Physiol*. 1986;375(1):625-642. doi:10.1113/jphysiol.1986.sp016137

199. Smarandache-Wellmann CR. Arthropod neurons and nervous system. *Curr Biol*. 2016;26(20):R960-R965. doi:10.1016/j.cub.2016.07.063

200. Mayford M, Siegelbaum SA, Kandel ER. Synapses and Memory Storage. *Cold Spring Harb Perspect Biol*. 2012;4(6):a005751. doi:10.1101/cshperspect.a005751

201. Tam S, Hurwitz I, Chiel HJ, Susswein AJ. Multiple Local Synaptic Modifications at Specific Sensorimotor Connections after Learning Are Associated with Behavioral

Adaptations That Are Components of a Global Response Change. *J Neurosci*. 2020;40(22):4363-4371. doi:10.1523/JNEUROSCI.2647-19.2020

202. Keene AC, Duboue ER. The origins and evolution of sleep. *J Exp Biol*. 2018;221(11):jeb159533. doi:10.1242/jeb.159533

203. Thiede KI, Born J, Vorster APA. Sleep and conditioning of the siphon withdrawal reflex in Aplysia. *J Exp Biol*. 2021;224(16):jeb242431. doi:10.1242/jeb.242431

204. Painter SD, Chong MG, Wong MA, Gray A, Cormier JG, Nagle GT. Relative Contributions of the Egg Layer and Egg Cordon to Pheromonal Attraction and the Induction of Mating and Egg-laying Behavior in Aplysia. *Biol Bull*. 1991;181(1):81-94. doi:10.2307/1542491

205. Kandel ER. *Behavioral Biology of Aplysia: A Contribution to the Comparative Study of Opisthobranch Molluscs*. W. H. Freeman; 1979.

206. Susswein AJ, Chiel HJ. Nitric oxide as a regulator of behavior: new ideas from Aplysia feeding. *Prog Neurobiol*. 2012;97(3):304-317. doi:10.1016/j.pneurobio.2012.03.004

207. Kilgore KL, Bhadra N. Nerve conduction block utilising high-frequency alternating current. *Med Biol Eng Comput*. 2004;42(3):394-406. doi:10.1007/BF02344716

208. Bhadra N, Bhadra N, Kilgore K, Gustafson KJ. High frequency electrical conduction block of the pudendal nerve. *J Neural Eng*. 2006;3(2):180-187. doi:10.1088/1741-2560/3/2/012

209. Lothet EH, Kilgore KL, Bhadra N, et al. Alternating current and infrared produce an onset-free reversible nerve block. *Neurophotonics*. 2014;1(1):011010. doi:10.1117/1.NPh.1.1.011010

210. Baek H, Pahk KJ, Kim H. A review of low-intensity focused ultrasound for neuromodulation. *Biomed Eng Lett*. 2017;7(2):135-142. doi:10.1007/s13534-016-0007-y

211. di Biase L, Falato E, Di Lazzaro V. Transcranial Focused Ultrasound (tFUS) and Transcranial Unfocused Ultrasound (tUS) Neuromodulation: From Theoretical Principles to Stimulation Practices. *Front Neurol*. 2019;10:549. doi:10.3389/fneur.2019.00549

212. Mori T, Sato T, Shigematsu Y, Yamada M, Nomura H. Can't Ultrasound Activate the Nervous System. *IEICE Trans 1976-1990*. 1987;E70-E(3):183-184.

213. Jordan T, Newcomb JM, Hoppa MB, Luke GP. Focused ultrasound stimulation of an ex-vivo Aplysia abdominal ganglion preparation. *J Neurosci Methods*. 2022;372:109536. doi:10.1016/j.jneumeth.2022.109536

214. Halpern JM, Xie S, Sutton GP, et al. Diamond electrodes for neurodynamic studies in Aplysia californica. *Diam Relat Mater*. 2006;15(2):183-187. doi:10.1016/j.diamond.2005.06.039

215. Huan Y, Gill JP, Fritzinger JB, et al. Carbon fiber electrodes for intracellular recording and stimulation. *J Neural Eng*. 2021;18(6):066033. doi:10.1088/1741-2552/ac3dd7

216. Chakravarthy K, Richter H, Christo PJ, Williams K, Guan Y. Spinal Cord Stimulation for Treating Chronic Pain: Reviewing Preclinical and Clinical Data on Paresthesia-Free High-Frequency Therapy. *Neuromodulation J Int Neuromodulation Soc*. 2018;21(1):10-18. doi:10.1111/ner.12721

217. Plachta DT, Gierthmuehlen M, Cota O, et al. Blood pressure control with selective vagal nerve stimulation and minimal side effects. *J Neural Eng*. 2014;11(3):036011.

218. Ikramuddin S, Blackstone RP, Brancatisano A, et al. Effect of Reversible Intermittent Intra-abdominal Vagal Nerve Blockade on Morbid Obesity: The ReCharge Randomized Clinical Trial. *JAMA*. 2014;312(9):915-922. doi:10.1001/jama.2014.10540

219. Wang YT, Rollins AM, Jenkins MW. Infrared inhibition of embryonic hearts. *J Biomed Opt*. 2016;21(6):060505.

220. Walsh AJ, Tolstykh GP, Martens S, Ibey BL, Beier HT. Action potential block in neurons by infrared light. *Neurophotonics*. 2016;3(4):040501. doi:10.1117/1.NPh.3.4.040501

221. Xia Q, Nyberg T. Inhibition of cortical neural networks using infrared laser. *J Biophotonics*. 2019;12(7):e201800403.

222. Hayashida Y, Sakata Y, Tanaka Y, Nomoto T, Yagi T. Local inhibition of microstimulation-induced neural excitations by near-infrared laser irradiation in mouse cerebral slices in vitro. In: IEEE; 2017:255-258.

223. Jiang B, Hou W, Xia N, et al. Inhibitory effect of 980-nm laser on neural activity of the rat's cochlear nucleus. *Neurophotonics*. 2019;6(3):035009.

224. Wells J, Kao C, Konrad P, et al. Biophysical mechanisms of transient optical stimulation of peripheral nerve. *Biophys J*. 2007;93(7):2567-2580.

225. Shapiro MG, Homma K, Villarreal S, Richter CP, Bezanilla F. Infrared light excites cells by changing their electrical capacitance. *Nat Commun*. 2012;3(1):1-11.

226. Duke AR, Peterson E, Mackanos MA, Atkinson J, Tyler D, Jansen ED. Hybrid electro-optical stimulation of the rat sciatic nerve induces force generation in the plantarflexor muscles. *J Neural Eng*. 2012;9(6):066006.

227. Plaksin M, Kimmel E, Shoham S. Correspondence: Revisiting the theoretical cell membrane thermal capacitance response. *Nat Commun*. 2017;8(1):1-2.

228. Mou Z, Triantis IF, Woods VM, Toumazou C, Nikolic K. A simulation study of the combined thermoelectric extracellular stimulation of the sciatic nerve of the Xenopus laevis: the localized transient heat block. *IEEE Trans Biomed Eng*. 2012;59(6):1758-1769.

229. Kato G. On the excitation, conduction, and narcotisation of single nerve fibres. In: Vol 4. Cold Spring Harbor Laboratory Press; 1936:202-213.

230. Stämpfli R. A new method for measuring membrane potentials with external electrodes. *Experientia*. 1954;10(12):508-509.

231. Julian FJ, Moore JW, Goldman DE. Membrane potentials of the lobster giant axon obtained by use of the sucrose-gap technique. *J Gen Physiol*. 1962;45(6):1195-1216.

232. Hajdu I, McDowall RJS. The dependence of neuromuscular transmission on glucose. *J Physiol*. 1949;108(4):502.

233. Matsumoto G, Tasaki I. A study of conduction velocity in nonmyelinated nerve fibers. *Biophys J*. 1977;20(1):1-13. doi:10.1016/S0006-3495(77)85532-X

234. De Col R, Messlinger K, Carr RW. Conduction velocity is regulated by sodium channel inactivation in unmyelinated axons innervating the rat cranial meninges. *J Physiol*. 2008;586(4):1089-1103. doi:10.1113/jphysiol.2007.145383

235. Stranders I, Diamant M, Gelder RE van, et al. Admission Blood Glucose Level as Risk Indicator of Death After Myocardial Infarction in Patients With and Without Diabetes Mellitus. *Arch Intern Med*. 2004;164(9):982-988. doi:10.1001/archinte.164.9.982

236. Yagihashi S, Mizukami H, Sugimoto K. Mechanism of diabetic neuropathy: where are we now and where to go? *J Diabetes Investig*. 2011;2(1):18-32.

237. Dobretsov M, Hastings SL, Stimers JR, Zhang JM. Mechanical hyperalgesia in rats with chronic perfusion of lumbar dorsal root ganglion with hyperglycemic solution. *J Neurosci Methods*. 2001;110(1-2):9-15. doi:10.1016/s0165-0270(01)00410-1

238. Jope RS, Domino EF, Mathews BN, Sitaram N, Jenden DJ, Ortez A. Free and bound choline blood levels after phosphatidylcholine. *Clin Pharmacol Ther*. 1982;31(4):483-487. doi:10.1038/clpt.1982.64

239. Institute of Medicine (US) Standing Committee on the Scientific Evaluation of Dietary Reference Intakes and its Panel on Folate, Other B Vitamins, and Choline. *Dietary Reference Intakes for Thiamin, Riboflavin, Niacin, Vitamin B6, Folate, Vitamin B12, Pantothenic Acid, Biotin, and Choline*. National Academies Press (US); 1998. Accessed December 14, 2022. http://www.ncbi.nlm.nih.gov/books/NBK114310/

240. Armstrong SA, Herr MJ. Physiology, Nociception. In: *StatPearls*. StatPearls Publishing; 2022. Accessed March 7, 2022. http://www.ncbi.nlm.nih.gov/books/NBK551562/

241. Gokin AP, Philip B, Strichartz GR. Preferential Block of Small Myelinated Sensory and Motor Fibers by Lidocaine: In VivoElectrophysiology in the Rat Sciatic Nerve. *Anesthesiology*. 2001;95(6):1441-1454. doi:10.1097/00000542-200112000-00025

242. Krumova EK, Zeller M, Westermann A, Maier C. Lidocaine patch (5%) produces a selective, but incomplete block of Aδ and C fibers. *PAIN*. 2012;153(2):273-280. doi:10.1016/j.pain.2011.08.020

243. McQuay H. Opioids in pain management. *The Lancet*. 1999;353(9171):2229-2232. doi:10.1016/S0140-6736(99)03528-X

244. Tanner JA. Reversible blocking of nerve conduction by alternating-current excitation. *Nature*. 1962;195(4842):712-713.

245. Avendaño-Coy J, Serrano-Muñoz D, Taylor J, Goicoechea-García C, Gómez-Soriano J. Peripheral Nerve Conduction Block by High-Frequency Alternating Currents: A Systematic Review. *IEEE Trans Neural Syst Rehabil Eng*. 2018;26(6):1131-1140. doi:10.1109/TNSRE.2018.2833141

246. Slavin KV. Technical Aspects of Peripheral Nerve Stimulation: Hardware and Complications. *Peripher Nerve Stimul*. 2011;24:189-202. doi:10.1159/000323275

247. Eldabe S, Buchser E, Duarte RV. Complications of Spinal Cord Stimulation and Peripheral Nerve Stimulation Techniques: A Review of the Literature. *Pain Med*. 2016;17(2):325-336. doi:10.1093/pm/pnv025

248. Wang M, Xia Q, Peng F, et al. Prolonged post-stimulation response induced by 980-nm infrared neural stimulation in the rat primary motor cortex. *Lasers Med Sci*. 2020;35(2):365-372. doi:10.1007/s10103-019-02826-0

249. Fekete Z, Horváth ÁC, Zátonyi A. Infrared neuromodulation:a neuroengineering perspective. *J Neural Eng*. 2020;17(5):051003. doi:10.1088/1741-2552/abb3b2

250. Horváth ÁC, Borbély S, Boros ÖC, et al. Infrared neural stimulation and inhibition using an implantable silicon photonic microdevice. *Microsyst Nanoeng*. 2020;6(1):1-12. doi:10.1038/s41378-020-0153-3

251. Sapareto SA, Dewey WC. Thermal dose determination in cancer therapy. *Int J Radiat Oncol Biol Phys*. 1984;10(6):787-800. doi:10.1016/0360-3016(84)90379-1

252. Dewey WC. Arrhenius relationships from the molecule and cell to the clinic. *Int J Hyperthermia*. 1994;10(4):457-483. doi:10.3109/02656739409009351

253. Kupfermann I, Carew TJ. Behavior patterns of Aplysia californica in its natural environment. *Behav Biol*. 1974;12(3):317-337. doi:10.1016/S0091-6773(74)91503-X

254. Kozub JA, Shen JH, Joos KM, Prasad R, Hutson MS. Efficacy and predictability of soft tissue ablation using a prototype Raman-shifted alexandrite laser. *J Biomed Opt*. 2015;20(10):105004. doi:10.1117/1.JBO.20.10.105004

255. Cayce JM, Wells JD, Malphrus JD, et al. Infrared neural stimulation of human spinal nerve roots in vivo. *Neurophotonics*. 2015;2(1):015007. doi:10.1117/1.NPh.2.1.015007

256. You M, Mou Z. Model study of combined electrical and near-infrared neural stimulation on the bullfrog sciatic nerve. *Lasers Med Sci*. 2017;32(5):1163-1172. doi:10.1007/s10103-017-2222-x

257. Boros ÖC, Horváth ÁC, Beleznai S, et al. Optical and thermal modeling of an optrode microdevice for infrared neural stimulation. *Appl Opt*. 2018;57(24):6952-6957. doi:10.1364/AO.57.006952

258. Takata AN, Zaneveld L, Richter W. *Laser-Induced Thermal Damage of Skin*. IIT RESEARCH INST CHICAGO IL; 1977. Accessed March 28, 2022. https://apps.dtic.mil/sti/citations/ADA054612

259. Cury J, Perre LV, Smets H, et al. Infrared neurostimulation in ex-vivo rat sciatic nerve using 1470 nm wavelength. *J Neural Eng*. 2021;18(5):056018. doi:10.1088/1741-2552/abf28f

260. Kou L, Labrie D, Chylek P. Refractive indices of water and ice in the 0.65- to 2.5-μm spectral range. *Appl Opt*. 1993;32(19):3531-3540. doi:10.1364/AO.32.003531

261. Markos C, Vlachos K, Kakarantzas G. Guiding and thermal properties of a hybrid polymer-infused photonic crystal fiber. *Opt Mater Express*. 2012;2(7):929-941. doi:10.1364/OME.2.000929

262. Dewhirst MW, Viglianti BL, Lora-Michiels M, Hanson M, Hoopes PJ. Basic principles of thermal dosimetry and thermal thresholds for tissue damage from hyperthermia. *Int J Hyperthermia*. 2003;19(3):267-294. doi:10.1080/0265673031000119006

263. Yarmolenko PS, Moon EJ, Landon C, et al. Thresholds for thermal damage to normal tissues: An update. *Int J Hyperthermia*. 2011;27(4):320-343. doi:10.3109/02656736.2010.534527

264. Owen SF, Liu MH, Kreitzer AC. Thermal constraints on in vivo optogenetic manipulations. *Nat Neurosci*. 2019;22(7):1061-1065. doi:10.1038/s41593-019-0422-3

265. Fekete Z, Csernai M, Kocsis K, Horváth ÁC, Pongrácz A, Barthó P. Simultaneous in vivo recording of local brain temperature and electrophysiological signals with a novel neural probe. *J Neural Eng*. 2017;14(3):034001. doi:10.1088/1741-2552/aa60b1

266. Zhao YH, Zhang YF, Bai SL. High thermal conductivity of flexible polymer composites due to synergistic effect of multilayer graphene flakes and graphene foam. *Compos Part Appl Sci Manuf*. 2016;85:148-155. doi:10.1016/j.compositesa.2016.03.021

267. Fang H, Zhang X, Zhao Y, Bai SL. Dense graphene foam and hexagonal boron nitride filled PDMS composites with high thermal conductivity and breakdown strength. *Compos Sci Technol*. 2017;152:243-253. doi:10.1016/j.compscitech.2017.09.032

268. Wei J, Liao M, Ma A, et al. Enhanced thermal conductivity of polydimethylsiloxane composites with carbon fiber. *Compos Commun*. 2020;17:141-146. doi:10.1016/j.coco.2019.12.004

269. Goncalves SB, Palha JM, Fernandes HC, et al. LED Optrode with Integrated Temperature Sensing for Optogenetics. *Micromachines*. 2018;9(9):473. doi:10.3390/mi9090473

270. Csernyus B, Szabó Á, Fiáth R, et al. A multimodal, implantable sensor array and measurement system to investigate the suppression of focal epileptic seizure using hypothermia. *J Neural Eng*. 2021;18(4):0460c3. doi:10.1088/1741-2552/ac15e6

271. Sohal HS, Clowry GJ, Jackson A, O'Neill A, Baker SN. Mechanical Flexibility Reduces the Foreign Body Response to Long-Term Implanted Microelectrodes in Rabbit Cortex. *PLOS ONE*. 2016;11(10):e0165606. doi:10.1371/journal.pone.0165606

272. Nguyen JK, Park DJ, Skousen JL, et al. Mechanically-compliant intracortical implants reduce the neuroinflammatory response. *J Neural Eng*. 2014;11(5):056014. doi:10.1088/1741-2560/11/5/056014

273. Coleman DL, King RN, Andrade JD. The foreign body reaction: A chronic inflammatory response. *J Biomed Mater Res*. 1974;8(5):199-211. doi:10.1002/jbm.820080503

274. Carnicer-Lombarte A, Chen ST, Malliaras GG, Barone DG. Foreign Body Reaction to Implanted Biomaterials and Its Impact in Nerve Neuroprosthetics. *Front Bioeng Biotechnol*. 2021;9. Accessed March 10, 2022. https://www.frontiersin.org/article/10.3389/fbioe.2021.622524

275. Suda EY, Gomes AA, Butugan MK, Sacco ICN. Muscle fiber conduction velocity in different gait phases of early and late-stage diabetic neuropathy. *J Electromyogr Kinesiol*. 2016;30:263-271. doi:10.1016/j.jelekin.2016.08.006

276. Mackel R, Brink E. Conduction of neural impulses in diabetic neuropathy. *Clin Neurophysiol*. 2003;114(2):248-255. doi:10.1016/S1388-2457(02)00320-6